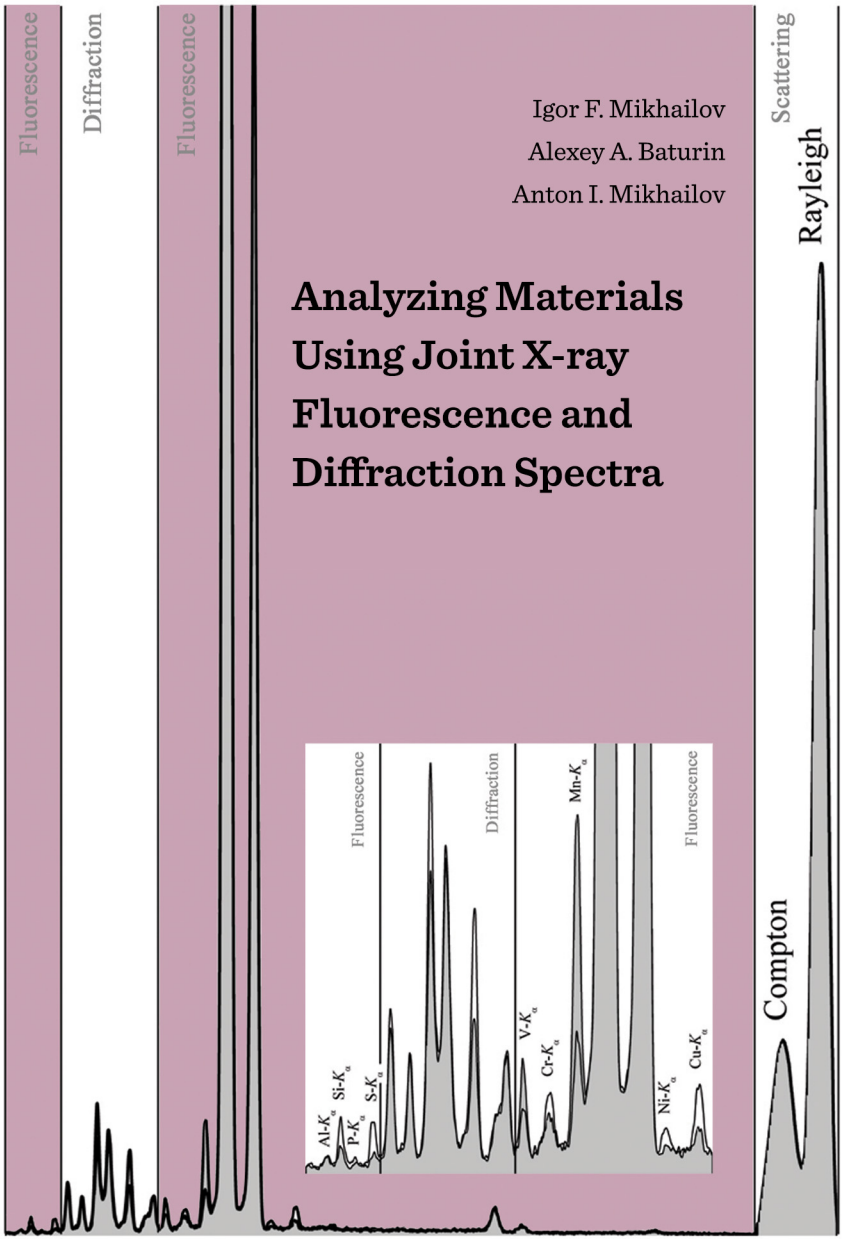

Igor F. Mikhailov
Alexey A. Baturin
Anton I. Mikhailov

Analyzing Materials Using Joint X-ray Fluorescence and Diffraction Spectra

Analyzing Materials Using Joint X-ray Fluorescence and Diffraction Spectra

Analyzing Materials Using Joint X-ray Fluorescence and Diffraction Spectra

By

Igor F. Mikhailov, Alexey A. Baturin and Anton I. Mikhailov

Cambridge Scholars Publishing

Analyzing Materials Using Joint X-ray Fluorescence and Diffraction Spectra

By Igor F. Mikhailov, Alexey A. Baturin and Anton I. Mikhailov

This book first published 2020

Cambridge Scholars Publishing

Lady Stephenson Library, Newcastle upon Tyne, NE6 2PA, UK

British Library Cataloguing in Publication Data
A catalogue record for this book is available from the British Library

ISBN (10): 1-5275-4246-7
ISBN (13): 978-1-5275-4246-4

CONTENTS

LIST OF LEGENDS

λ	Wavelength in Å (1 Å=10^{-10} m)
μ	Mass attenuation coefficient
σ	Mass scattering coefficient
φ	Angle of incidence
ψ	Exit angle
θ	Bragg diffraction angle
2β	Scattering angle
d	Interplanar spacing
ρ	Density
ω	Fluorescence yield
C	Concentration of a chemical element in the material
C_{min}	Limit of detection
E	Radiation energy
I	Radiation intensity
t	Thickness
Z	Atomic number of a chemical element
WDXRF	Wavelength Dispersion X-ray Fluorescence
EDXRF	Energy Dispersion X-ray Fluorescence

FOREWORD

Determination of the material composition using the XRF method is carried out by the intensity of fluorescent radiation, while the primary radiation, which is scattered by the sample, and the diffraction reflections are considered to be background signals and are rarely used for analytical purposes. To increase the sensitivity of the analysis, empirical methods are commonly used—filters, secondary emitters, monochromators, etc.—in the X-ray optical scheme. However, with the empirical approach, it is impossible to determine whether the adopted measurement scheme provides the highest sensitivity for the given chemical elements, or if there is another, more effective solution.

Apparently, in order to achieve the highest sensitivity of the analysis, it is necessary to optimally form the entire X-ray spectrum, including X-ray fluorescence, scattering (coherent and incoherent), and diffraction using a crystal lattice. In this book, we propose a general approach to solve the problem of optimizing X-ray optical schemes for the formation of spectra using the criterion of detection limit.

In recent years, a significant number of papers have appeared in which scattered radiation measurements have been used to correct XRF results. Even semi-quantitative measurements of coherent and incoherent (Compton) scatter peaks expand XRF capabilities in determining light elements. However, a precision measurement of the scattering peaks is

difficult to achieve in traditional XRF schemes. The optimization of X-ray optical schemes provides high accuracy when measuring scattered radiation. This opens up prospects for determining elements (up to hydrogen) with a small atomic number.

With the optimization of the X-ray optical schemes, conditions are created for reliably measuring the diffraction reflections of the material under study in the combined spectrum. The identification of these reflections allows one to carry out a quantitative phase analysis and to determine elements with a small atomic number by the amount of the phase that contains them (for example, carbon in cementite).

The specific conditions to measure the combined spectra, as well as the experimental X-ray optical schemes and their individual elements have been developed. Numerous examples on solving specific analytical problems are given: trace impurities at the level of 0.1–1.0 ppm; elements with a low atomic number from 6 (C) to 1 (H); phases based on light elements; and depth distribution of impurities in the bulk, etc.

The solution to the complex problem of forming a combined X-ray spectrum, including fluorescent, scattered, and diffracted radiation, gives an opportunity to expand the applications of X-ray methods when studying material composition, both in terms of the range of chemical elements and the sensitivity.

Over the past hundred years, many articles, monographs, and textbooks on X-ray analysis methods have been published. The authors hope that the reader is familiar with the fundamental works in this field and so they have,

therefore, limited themselves to mentioning the basic principles and literary references.

Acknowledgments

The main developments presented in the monograph are made at the Department of Physics of Metals and Semiconductors at the NTU "Kharkov Polytechnic Institute". The authors thank Professors V.V. Kondratenko, E.N. Zubarev, V.E. Puha, V.V. Belozerov, A.A. Mamalouy, and S.V. Malykhin for many years of cooperation and the provision of unique experimental results.

They are also thankful to employees of the X-ray Lab S.S. Borisova Ph.D. and L.P. Fomina Ph.D. for their continued support through their work, discussions, and helpful manuscript edits. The authors are especially grateful to the “Ukrrentgen” research and production firm (Kharkiv), headed by I.N. Babenko, and "Elvatekh" (Kiev), headed by A.S. Filippov, for their hardware support.

CHAPTER 1

BASIC PRINCIPLES OF X-RAY ANALYSIS

One of the basic methods for analyzing the composition of materials is X-ray fluorescence analysis (XRF). This method determines the positions and intensities of the lines in the spectrum of X-ray fluorescence that arise from the absorption of photons emitted by a primary source [1-4]. The interaction of the photons with a substance is not only limited by their absorption and emission of the fluorescence radiation. Also, an essential role is played by the phenomena of scattering atoms [2, 5] and diffraction reflection from the crystalline lattice of the material [6]. These phenomena are well studied and used for the structure certification of materials; however, in the framework of XRF, these were traditionally considered to be a background source. In the present work, we have shown that these phenomena can be used in combination with XRF to determine the chemical composition.

1.1 X-ray interaction with substance

X-ray radiation passing through a substance is attenuated according to the known Buger-Lambert-Baer law [2, 3]:

$$I = I_0 \exp(-\mu_l t) \tag{1.1}$$

where I_0 is the intensity of the primary radiation; I is the intensity of the radiation after passing through the layer with thickness, t; and μ_l is the linear attenuation coefficient characterizing the attenuation of X-rays per unit path length.

Usually, the mass attenuation coefficient is used for these calculations: $\mu = \mu_l / \rho$, where ρ is the substance density. The attenuation is caused by two processes: absorption, τ, and scattering, σ [2, 4]. So that,

$$\mu = \tau + \sigma . \tag{1.2}$$

When absorbed, a photon ionizes the atom's internal electron shells. The system tends to return to the most favorable energy state. This is accomplished by electron transfer from a more distant nucleus shell; for example, *L*, to an unoccupied inner level *K* (Fig. 1.1). Wherein the electron emits an energy portion equal to the difference between the energies of the shells. The wavelength of the emitted fluorescence radiation is characteristic for a certain element.

The probability of an electron transfer to the *K*-level that emits fluorescence radiation, ω_k, is called the fluorescence yield. This probability is reduced by the so-called Auger effect, which appears if a secondary radiation quantum is generated by an excited; for example, a *K*-shell interacting with electrons from more distant shells. As a result, the *K*-series radiation is absent outside of the atom; however, *L*- or *M*-series radiation and a free

Auger-electron are emitted. The probability of the Auger-electron emitting, a_k, is related with the fluorescence yield, ω_k, as

$$\omega_k + a_k = 1 \,. \tag{1.3}$$

To evaluate the fluorescence yield, the following approximate formula is used [4]:

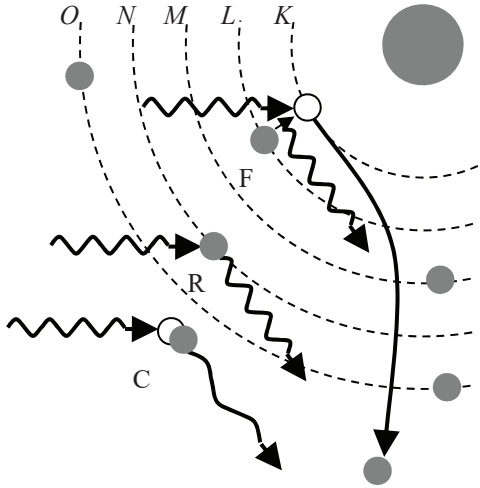

Figure 1.1: Processes accompanying the passage of X-rays through substance: F, the absorption of a photon and emitting fluorescence radiation; R, coherent (Rayleigh) scattering; C incoherent (Compton) scattering.

$$\omega_q = Z^4 / \left(a_q + Z^4\right) \tag{1.4}$$

where Z is the atomic number; q is the number of the level (the coefficients for K-, L-, and M- series: $a_K = 1{,}06 \cdot 10^6$; $a_L = 1 \cdot 10^8$; $a_M = 1{,}4 \cdot 10^9$).

The dependence of the absorption coefficient τ on the wavelength λ is a piecewise continuous function. The wavelengths corresponding to the excitation energies of *K*-, L_{I}-, L_{II}-, L_{III}-, M_{I}, and other atomic levels have absorption jumps, S_q. The relative portion of the photons absorbed by a *q*-level is $(S_q - 1)/ S_q$. Between the absorption jumps, the function τ (λ) is approximated by the relation [4]:

$$\tau(\lambda) = G\lambda^{\alpha} Z^{\beta}, \tag{1.5}$$

where $\alpha \approx 2.7$; $\beta \approx 2.5 \div 3$; *G* is a tabular coefficient [9]. For practical calculations, one can use the appropriate tables.

The physical basis of the quantitative X-ray spectral analysis is Moseley's law. which establishes a single-valued relationship between the wavelengths λ of analytical lines and the atomic numbers Z of the corresponding chemical elements. In particular, for $K_{\alpha 1}$-lines, this is written as [4]

$$\lambda = (Z-1)^{-2} \times 1.21 \times 10^{3}, \text{ [Å]} \tag{1.6}$$

The scattering coefficient consists of two components: $\sigma = \sigma_R + \sigma_C$; σ_R is coherent (Rayleigh), and σ_C is incoherent (Compton).

Coherent scattering is caused by the elastic interaction of a photon with bound electrons of atomic shells, when the direction of the photon motion is changed but its energy remains the same. Under incoherent (Compton) scattering, a part of the energy is transferred to a loosely coupled electron, which results in increasing the wavelength of the scattered radiation (Fig. 1.1). The ratio of the coherent-to-incoherent scattering intensities is drasti-

cally changed as the atomic number of the material decreases. This effect causes a unique opportunity for the quantitative analysis of light elements, up to hydrogen, using X-ray methods. This opportunity was predicted by Compton [7] and will be discussed in Chapter 4.

The intensity of the scattered X-rays is about factor 100 lower than the absorbed beam intensity; this is caused by the ratio (σ/μ) of scattering (σ) and attenuation (μ) mass coefficients.

1.2 Characteristics of X-ray spectra

An X-ray spectrum is the dependence of signal intensity on the energy (wavelength) of an X-ray quantum (Fig. 1.2). In the X-ray spectra, both processes considered in the previous section are observed: absorption and scattering. The absorption is accompanied by the fluorescence characteristic emission of the sample material; therefore, the fluorescence atoms' analytical lines appear in the spectrum. In Figure 1.2, these are the lines with wavelengths more than 1 Å (Ni-K_β, Cu-K_α, etc.). The scattering manifests itself through two peaks: the coherent scattering of the characteristic radiation of the X-ray tube anode material (Ag-K_α in the figure), and the incoherent scattering (not shown in the figure). In addition, a broadband background exists, which is caused by the scattering of the bremsstrahlung radiation (continuous spectrum). Thus, the spectrum consists of analytical and background signals, which are different widths. The width of the analytical peak is determined by the physical width of the spectral line (about 1 eV) and the energy resolution of the X-ray spectrometer, which varies from 1 eV to 500 eV depending on the type of the spectrometer and the energy of quanta. *Spectral resolution* is the minimum revealed difference

between the energies of two neighboring lines; this is determined by their half-width and, consequently, by the characteristics of the spectrometer.

The quantitative analysis of the chemical composition is accomplished through the intensity of the analytical lines. The background signal has a smooth function with a characteristic decrement of ~ 1 keV. This broad-band background is superimposed on the fluorescence spectrum and complicates the ability to reveal the weak lines: i.e., it reduces the sensitivity of the analysis.

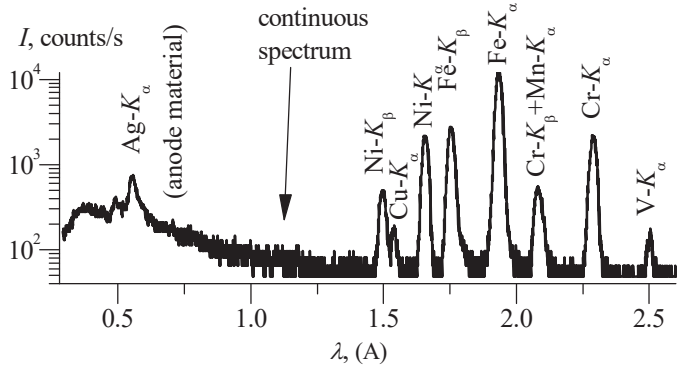

Figure 1.2: X-ray fluorescence spectrum of a steel standard sample

X-ray spectra are divided into the series labeled with the following letters: *K*, *L*, *M*, *N*, and *O*. Each series consists of lines labeled in order of the increasing radiation energy (α, β, γ, etc.) with digital indices: $K_{\alpha 1}$, $K_{\alpha 2}$, $K_{\beta 1}$, $K_{\beta 2}$, $L_{\alpha 1}$, $L_{\alpha 2}$, etc. The relative intensity of the line in the series is determined by the probability of the corresponding electron transfers between the levels. It is also characterized by the statistical weight *p*.

In comparison with optical ones, X-ray spectra are simple and consist of a small number of lines. This is caused by the fact that X-ray spectra are due to transfers to inner electron shells that have not been deformed by chemical bonds. The simplicity and stability of X-ray spectra under the formation of chemical bonds provides a unique opportunity to solve the inverse problem of determining the sample chemical composition using the full-profile analysis of its X-ray spectrum. The solution to the problem is impossible for optical spectra because of their significant variations for different phases; this fact does not allow for choosing a stable basis for the expansion of the functional.

One of the main spectral characteristics is *contrast*: the ratio of the analytical line peak intensity to the background under this line. Evidently, for the given integral intensity of the analytical line, the smaller its half-width, the higher its contrast. In this sense, the highest contrast is characteristic for lines with their half-width close to the *physical* width of lines: i.e. when the *apparatus* factor of line blurring is absent. Using this assumption, the theoretical detection limit for impurities for XRF was obtained in [8]. However, in real instruments, the contribution of this apparatus factor into the line blurring is high and will be discussed below.

Thus, the smaller the spectral line half-width, the higher the contrast and spectral resolution, or, in other words, the higher the spectrum quality. However, the high quality of the spectrum is not enough to provide a high sensitivity in the analysis. A characteristic of analysis sensitivity is the *detection limit*: the smallest concentration of the element revealed in the sample. According to the statistical interpretation, the detection limit, $C_{\min}$, is the content of the element in the sample, in which the average value of

the difference between the analytical signal I and the background signal I_b is a factor k larger than the standard deviation σ_b of the background signal [4, 9]. The value of k is determined by the chosen statistical certainty. At k = 3, which is more often used in practice, the statistical certainty of correct detection is 50%, and the false one is 14 %.

The *detection limit,* C_{min}, is determined by the formula:

$$C_{min} = 3\frac{\sqrt{I_b}}{\partial I/\partial C} = \frac{3}{\sqrt{K \cdot \partial I/\partial C}}. \quad (1.7)$$

The variation of signal (pulse count) per 1 % of impurity content $\partial I/\partial C$ is called *concentration sensitivity* and $K = \frac{\partial I/\partial C}{I_b}$ is the signal contrast for an impurity with a concentration of 1 % mass. In order to lower the C_{min}, along with contrast increasing, it is necessary to raise the concentration sensitivity (at the given X-ray tube power), which is determined by the *luminosity* of the spectrometer.

The *luminosity* of the spectrometer (ε) is the ratio of the emergent and incident radiation energies [10]. This ratio depends on the applied X-ray optic scheme and characteristics of its components (monochromators, secondary targets, detectors, etc.). Essentially, the *luminosity* ε is the device efficiency.

1.3 Measuring the intensity of spectral lines

The quantitative analysis of the chemical element content is carried out by the calibration function method [3]. According to this method, measuring the intensity of analytical lines is fulfilled for standards with certified concentrations of corresponding elements at the first stage. From the results of the measurements, a plot of the concentration versus the fluorescence integral intensity is built for each chemical element. Using this calibration function, the background value I_b is determined by extrapolation to the zero concentration, and the concentration sensitivity $\partial I/\partial C$ by the slope of the plot. The detection limit is calculated by Eq. (1.7) for a measuring time equal to that of I_b and $\partial I/\partial C$, and the standard deviation is determined by the scattering of experimental values relative to the regularization curve. At the second stage, fluorescence line intensities are measured for the test sample and then the calibration plot determines the concentration of the corresponding impurity. In the case of a significant difference between the base materials of the standard and the test samples, a correction using the base effect in the intensity of analytical line is carried out and the corresponding correction is entered into the concentration value.

The analytical line integral intensity of an impurity is measured in the specific energy range created by the spectrometer energy resolution. It is clear that the narrower the chosen range, the smaller the number of counts for the same measurement time. This would result in a predominant $\partial I/\partial C$ decrease in comparison with $\sqrt{I_b}$ in Eq. (1.7) and, consequently, to an increase in C_{min}. However, an unreasonable expansion of the energy interval would lead to a decrease in contrast due to capturing the background.

Thus, it is intuitively clear that, in order to obtain the minimum C_{min}, we should optimize the measurement interval for the impurity analytical line integral intensity.

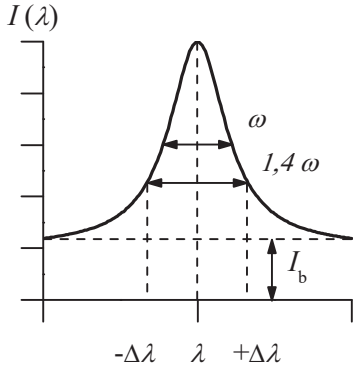

Figure 1.3: Optimal wavelength interval to measure intensity

We will now consider the measurement optimal interval problem in more detail. The shape of an analytical line is given by the quadratic Cauchy function [11] (Fig. 1.3):

$$I(\lambda) = I\left(1+\frac{\lambda^2}{\omega/2}\right)^{-1} \tag{1.8}$$

where I is the peak intensity and ω is the line width at the half-maximum height.

Measurements of the integral intensity are carried out in the range of $\pm\Delta\lambda$ at I_b = const:

$$I(\text{int}) = \int_{-\Delta\lambda}^{\Delta\lambda} I\left(1+\frac{\lambda^2}{\omega/2}\right)^{-1} d\lambda = I\ \omega\ \text{arctg}\left(\frac{\Delta\lambda}{\omega/2}\right),$$
$$I_b(\text{int}) = I_b\, 2\Delta\lambda \tag{1.9}$$

Substituting (1.9) into (1.7) we obtain

$$C_{\min} = 3\frac{\sqrt{I_b\ 2\ \Delta\lambda}}{I\ \omega\ \text{arctg}\left(\frac{\Delta\lambda}{\omega/2}\right)}. \tag{1.10}$$

By optimizing $\Delta\lambda$ from the condition of $\partial C_{\min}/\partial(\Delta\lambda) = 0$, we obtain the equation:

$$\text{arctg}\left(\frac{\Delta\lambda}{\omega/2}\right) - \frac{\Delta\lambda\omega}{\left(\omega^2/4+\Delta\lambda^2\right)} = 0. \tag{1.11}$$

The numerical decision of Eq. (1.11) gives the optimal interval for the integral intensity measurements, $2\ \Delta\lambda = 1.4\ \omega$, in which the minimum value of $C_{\min}$ can be obtained. All subsequent experimental measurements of analytical line intensities in EDXRF were fulfilled in this energy range.

1.4 Wave-dispersion and energy-dispersion X-ray fluorescence analysis

Various X-ray schemes were applied to reduce the background signal and increasing the sensitivity of analysis [12, 13]. As previously stated, the main source of the background is the X-ray tube bremsstrahlung emission, which is scattered at the sample and spectrometer components, and also gets into the detector. Therefore, to prevent this signal from entering the

detector, the bremsstrahlung intensity should be drastically reduced directly after the X-ray tube or using filter collimation systems that are installed between the sample and the detector should protect it. Thus, we can select two basic nodes from an X-ray optic scheme: the primary spectrum formation unit and the spectrum registration unit. In general, the XRF scheme includes the following main nodes (Fig. 1.4): an X-ray tube, a primary spectrum formation unit, and a spectrum registration unit.

According to the distribution of functions between the primary spectrum formation unit and the registration unit, spectrometers are distinguished as either having wave-dispersion (WDXRF) or energy-dispersion (EDXRF).

We will distinguish between the broadband and selective excitation of the sample's fluorescence. The broadband excitation is caused by the bremsstrahlung radiation of the X-ray tube and always results in scattering backgrounds in X-ray spectra. The selective excitation is produced by a system of monochromatic lines obtained in the formation unit. With the selective excitation, the level of the broadband background is extremely low and created by the multiple scattering of the bremsstrahlung radiation. However, the selective excitation is always associated with a large loss of intensity and can only be applied in the devices with high luminosity.

The main functional difference between WDXRF and EDXRF spectrometers are as follows:

- WDXRF uses broadband fluorescence excitation from the sample and selective detection.
- EDXRF uses broadband or selective fluorescence excitation from the sample and broadband detection.

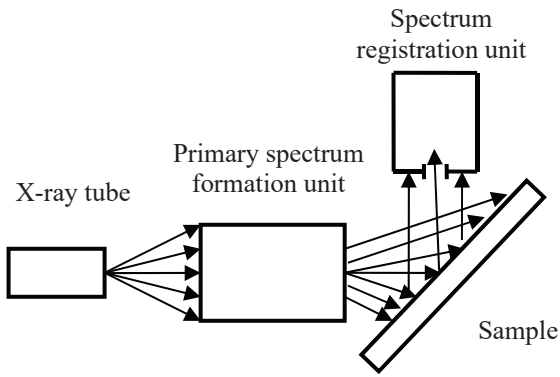

Figure 1.4: X-ray optic scheme for XRF

The broadband fluorescence excitation of the sample means that the primary spectrum formation unit is practically absent. In some cases, focusing capillary lenses are applied [5]. The X-ray tube radiation falls on the sample without any monochromatization. Unambiguously, this provides a high intensity of secondary emissions from the sample's chemical elements. However, getting into the registration unit, the sample radiation passes a long path through the collimation system and reflects from the crystal-analyzer, thus losing up to 99 % of its intensity. In order to prevent the absorption of the signal by air, the body of the WDXRF spectrometer is evacuated. Their comparably large dimensions and energy consumption characterize these types of spectrometers.

EDXRF spectrometers have high luminosity and can use both broadband and selective excitation of fluorescence. Under broadband excitation, the fluxes are so high that they exceed the permissible load of the detector and degrade the quality of spectra. Therefore, the X-ray tube power should be

limited and the measurements of the spectrum should be fulfilled in parts. However, the high level of the scattering background with broadband excitation is the principal limitation of the analysis' sensitivity. With the selective excitation, the sensitivity can be significantly increased using the calculation of the parameters for the formation unit (see Section 3).

EDXRF spectrometers use a broadband detection regime, where the detector simultaneously registers photons of all energies [13]. The detector is located a few millimeters away from the sample, thus providing a larger aperture for capturing the fluorescence radiation; this makes it possible avoid vacuuming for most analytical problems. Compact X-ray schemes with broadband detection formed the basis for creation of portable X-ray spectrometers with high luminosity.

The main factor influencing the fluorescence spectrum contrast (particularly with the broadband detection) is the fluorescence excitation method, which is realized by the spectrum formation unit. Five main methods of fluorescence excitation are known [2, 5, 13–17]. The higher contrast is required to solve a specific analytical problem; this means that more energy must be removed from the X-ray tube spectrum. Thus, the contrast is achieved at the expense of X-ray scheme luminosity losses. In order of decreasing luminosity and increasing contrast of the spectrum, the following methods of fluorescence excitation are used in known X-ray schemes:

1. An X-ray tube primary spectrum with filtration [13];
2. A quasi-monochromatic spectrum of the secondary target fluorescence emission [13, 14];

3. An X-ray primary spectrum monochromatized using a reflection from the face of a single crystal [5, 15];
4. Polarized primary radiation [16];
5. A “grazing” beam at the Brewster angle of the total external reflection [17].

The X-ray fluorescence excitation method is set by the *primary spectrum formation unit* (PSFU). Optimizing the PSFU parameters: namely, the supply voltage, filter and target parameters, and the scheme’s geometry—provide the best spectral contrast and the minimum detection limit.

1.5 A general approach for calculating X-ray spectra

Optimization of the parameters mentioned in 1.4 is realized theoretically from the condition that the total differential of the detection limit $C_{\min}$ is zero:

$$dC_{\min}(U, \tau, \mu, \sigma, t, \varphi, \psi) = 0, \tag{1.12}$$

Here U is the supply voltage. The filter and target parameters are mass coefficients of absorption (τ), attenuation (μ), and scattering (σ); t is the filter thickness. φ is an incident angle, and ψ is an exit angle from the beam and these mark the geometry parameters of the scheme.

When solving this problem, three X-ray fluxes were considered. $\Phi_{01}(\lambda)$ is the primary radiation flux (spectrum); $\Phi_{02}(\lambda)$ is the radiation flux which is formed by the fluorescence excitation unit; and $\Phi_{03}(\lambda)$ is the flux getting into the detector. The X-ray tube flux $\Phi_{01}(\lambda)$ includes the anode characteristic emission and the bremsstrahlung radiation [4]:

$$\Phi_{01}(\lambda) = \Phi_{c}(\lambda) + \sum_{i} \delta(\lambda - \lambda_i)\,\Phi_{ch}(\lambda)$$

Here $\delta(\lambda-\lambda_i)$ is a delta-function.

The $\Phi_{02}(\lambda)$ flux is determined by the spectrum forming unit, and will be discussed in detail below. The $\Phi_{03}(\lambda)$ flux sets the detection limit $C_{\min}(\lambda)$ for the i-th element emitting the fluorescence radiation with a wavelength λ_i. Using [1, 10], it can be expressed as

$$\Phi_{03}(\lambda) = \frac{S_S \sin\varphi}{4\pi r^2} \times \frac{\Phi_{02}(\lambda)\,\sigma_3(\lambda)}{\mu_3(\lambda)\left(\dfrac{1}{\sin\varphi} + \dfrac{1}{\sin\psi}\right)} + \frac{S_S \sin\varphi}{4\pi r^2} \times$$

$$\times \sum_{i=1}^{n} \frac{1}{1 + \dfrac{(\lambda_i - \lambda)^2}{(\Delta\lambda_i/2)^2}} \frac{1}{\Delta\lambda_i} C_i\, p_i\, \omega_{qi} \left(1 - \frac{1}{S_{qi}}\right) \int_{\lambda_{ed}}^{\lambda_{qi}} \frac{\Phi_{02}(\lambda)\,\tau_i(\lambda)}{\dfrac{\mu_3(\lambda)}{\sin\varphi} + \dfrac{\mu_3(\lambda_i)}{\sin\psi}}\,\mathrm{d}\lambda \tag{1.13}$$

where S_S is the sample irradiated area "seen" by the detector; r is the distance between the sample and the detector; λ_{ed} is the wavelength of the continuum spectrum edge; $\Delta\lambda_i$ is a half-width of the spectral line (spectrometer resolution); $\sigma_3(\lambda)$ and $\mu_3(\lambda)$ are, respectively, mass coefficients of scattering and attenuation of the $\Phi_{02}(\lambda)$ flux by the sample material; $\tau_i(\lambda)$ is the mass coefficient of the $\Phi_{02}(\lambda)$ flux absorption by atoms from the analyzed i-th chemical element; $\mu_3(\lambda_i)$ is the mass coefficient of the attenuation of the i-th chemical element fluorescence radiation by the sample material; C_i is the concentration of the analyzed i-th chemical element; p_i is the line relative intensity in the spectral series; and ω_{qi} is the fluorescence yield for the i-th chemical element.

The first summand in (1.13) describes the function of scattering the $\Phi_{02}(\lambda)$ flux and determines the main component of the background. The second summand describes the analytical lines of the sample chemical elements. The line profile is given by the Cauchy function. The optimization, which uses the criterion of $C_{\min}$, assumes the substitution of I_b (background) and the $\partial I_i / \partial C_i$ in (1.7). The contrast of the fluorescence spectrum or the "peak-to-background" ratio for the i-th element can be calculated as

$$K(\lambda) = C_i p_i \omega_{qi} \left(1 - \frac{1}{S_{qi}}\right) \frac{\sum_{i=1}^{n} \frac{1}{1 + \frac{(\lambda_i - \lambda)^2}{(\Delta\lambda_i/2)^2}} \frac{1}{\Delta\lambda_i} \int_{\lambda_{ed}}^{\lambda_{qi}} \frac{\Phi_{02}(\lambda)\tau_i(\lambda)}{\frac{\mu_3(\lambda)}{\sin\varphi} + \frac{\mu_3(\lambda_i)}{\sin\psi}} \mathrm{d}\lambda}{\frac{\Phi_{02}(\lambda)\sigma_3(\lambda)}{\mu_3(\lambda)\left(\frac{1}{\sin\varphi} + \frac{1}{\sin\psi}\right)}}. \tag{1.14}$$

The detection limit is determined according to (1.7)

$$C_{\min}(\lambda) = \frac{3\sqrt{\sin\varphi}}{C_i\ p_i\ \omega_{qi}\left(1 - \frac{1}{S_{qi}}\right)\sqrt{\frac{S}{4\pi r^2}}} \times .$$

$$\times \frac{\sqrt{\frac{\Phi_{02}(\lambda)\sigma_3(\lambda)}{\mu_3(\lambda)\left(\frac{1}{\sin\varphi} + \frac{1}{\sin\psi}\right)}}}{\sum_{i=1}^{n} \frac{1}{1 + \frac{(\lambda_i - \lambda)^2}{(\Delta\lambda_i/2)^2}} \frac{1}{\Delta\lambda_i} \int_{\lambda_{ed}}^{\lambda_{qi}} \frac{\Phi_{02}(\lambda)\tau_i(\lambda)}{\frac{\mu_3(\lambda)}{\sin\varphi} + \frac{\mu_3(\lambda_i)}{\sin\psi}} \mathrm{d}\lambda} \tag{1.15}$$

The Eq. (1.14) and (1.15) are general and can be applied to any function of the primary spectrum: for example, for the X-ray tube or synchrotron radiation. On the basis of Eq. (1.15), the optimization problem for $C_{\min}$ can be considered in its general form, according to Eq. (1.12). In our monograph, all calculations of X-ray schemes for X-ray tube primary radiation were based on this approach.

The number of photons emitted per 1 s within the solid angle, which is 1 steradian for the given characteristic line, determines the characteristic radiation intensity I_{ch} of the anode material. The bremsstrahlung radiation or the continuous spectrum is determined by the spectral density $\partial I_c/\partial\lambda$: the number of photons (in the unit energy interval) emitted per second within a solid angle of 1 steradian. The values, I_{ch} and $\partial I_c/\partial\lambda$, set the form of the characteristic and the continuous spectra of the X-ray tube. They are determined using the following formulas from [10]:

$$I_{\text{ch}} = 5\times10^{14}\, i_a\, \frac{\gamma\, \omega_q\, p\, R}{Z_a}\left(\frac{\lambda_{1q}}{\lambda_{\text{ed}}}-1\right)^{1.67} \quad \left[\frac{\text{photon}}{\text{s sr}}\right], \tag{1.16}$$

$$I_{\text{c}} = -109\times10^{8} Z_a\, i_a\, \frac{1}{\lambda^2}\left(\frac{\lambda}{\lambda_{\text{кр}}}-1\right) \quad \left[\frac{\text{photon}}{\text{s sr A}}\right], \tag{1.17}$$

where $R = \left(1-\dfrac{7\,Z_a-80}{14\,Z_a-80}\right)$, Z_a is the atomic number of the anode material; i_a is the anode current; $\gamma = 3.8\cdot10^{-2}$ for the *K*-series and 0.11 for the *L*-series; ω_q is the fluorescence yield; p is the portion of intensity in the spectral series; λ_{1q} is the absorption jump wavelength of the X-ray tube anode

material; and λ_{ed} = 12.39/U (kV) is the wavelength of the continuous spectrum edge.

Thus, the *primary spectrum formation unit* may be considered to be an operator acting on the primary X-ray source spectrum. With fluorescence selective excitation, the radiation flux $\Phi_{02}(\lambda)$ is the general form of the beam formation function. This function can be obtained from the expressions for the X-ray tube primary radiation intensity (Eq. [1.16] and [1.17]) and by the action of the following operators:

Filtration $$\exp\left(-\mu_f(\lambda) t_f \rho_f\right); \qquad (1.18)$$

Scattering $$\frac{\sigma_2(\lambda)}{\mu_2(\lambda)\left(\frac{1}{\sin\varphi}+\frac{1}{\sin\psi}\right)}; \qquad (1.19)$$

Fluorescence $$\int_{\lambda_{ed}}^{\lambda_{2q}} \frac{\tau_2(\lambda)}{\frac{\mu_2(\lambda)}{\sin\varphi}+\frac{\mu_2(\lambda_2)}{\sin\psi}}\, d\lambda; \qquad (1.20)$$

and

Monochromatization $$k\,\frac{\left(1+\cos^2 2\theta\right)}{\sin 2\theta}\,\frac{\lambda^3}{\mu(\lambda)}. \qquad (1.21)$$

Here, the filter parameters are as follows: $\mu_f(\lambda)$ is the mass attenuation coefficient; t_f is the thickness; and ρ_f is the density. The parameters for the secondary target—$\sigma_2(\lambda)$, $\mu_2(\lambda)$, $\tau_2(\lambda)$—are, respectively, the mass coefficients of scattering, attenuation, and absorption of the primary radiation by

the target material. $\mu_2(\lambda_2)$ is the mass coefficient for the attenuation of the target fluorescence using its own material; λ_{2q} is the absorption jump wavelength for the target material; and k is the reflectivity of the monochromator.

We have not consider the schemes of the fluorescence selective excitation using polarized radiation or a grazing beam at Brewster's angle for the total external reflection because, in these schemes, the arrival of the scattered continuous spectrum onto a sample is excluded. In the first case, the long-wave spectrum is filtered, and the short-wave one (the "bell" of bremsstrahlung radiation) is removed by increasing the tube voltage (more than 100 kV); this means that this is transferred beyond the effective scattering range of the primary beam using polarizer atoms [16]. In the second case, due to the small incident angle (less than 1 deg.), the primary radiation penetrates the sample depth by no more than 100 Å; this means that the substrate influence will be excluded, and there will only be a specular scattering component, which will be cut off by collimators and practically absent in the fluorescence spectrum. Thus, with these X-ray schemes, the sensitivity depends on the primary source intensity and the precision of the scheme geometry.

1.6 Schemes for primary spectrum formation

It is clear from Eq. (1.7) that in order to decrease the C_{min}, it is necessary to reduce the background under the measured analytical line and to increase its intensity. This means that the first summand in Eq. (1.13) should be significantly lower than the second one for $\lambda = \lambda_i$ (λ_i is the i-th element fluorescence wavelength). However, when determining the contents of

several impurities with a different λ_i, this requirement must be fulfilled for each of them. Due to the fact that the fluorescence excitation efficiency drops sharply with the distance from the absorption edge of the analyzed chemical element, the incident spectrum must contain a set of characteristic lines positioned near the absorption edges of the analyzed elements, and the broadband background should be minimal. This spectrum would be ideal since it would provide the highest sensitivity in terms of the XRF.

Filtration of the X-ray tube primary spectrum

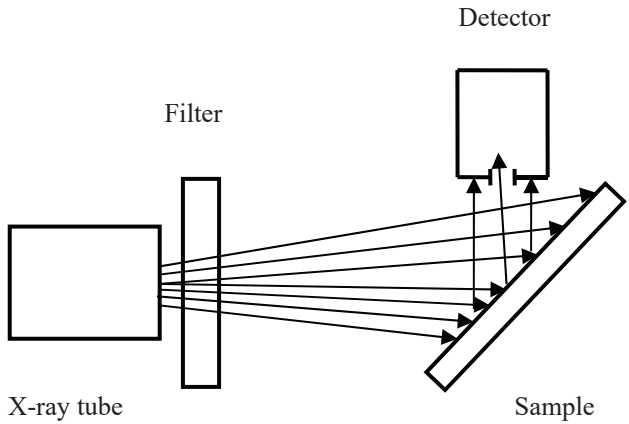

Figure 1.5: *a.* X-ray optic scheme with primary beam filtration

The point of filtration is to maximize the suppression of the primary spectrum in the range of the measured analytical line [13]. Figure 1.5 shows the X-ray optic scheme using the filtration of the primary beam. A filter is located close to the X-ray tube, so that the entire beam passes through it.

After filtration, the radiation falls on the sample, and the detection unit detects the fluorescence of its elements. The filter material is chosen by the fact that its absorption jump must not be in the range where the analytical signal is expected [13].

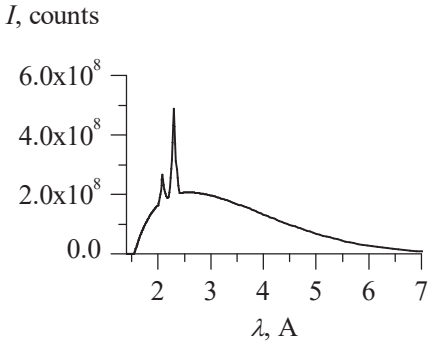

Figure 1.5: *b*. The primary spectrum from an X-ray tube

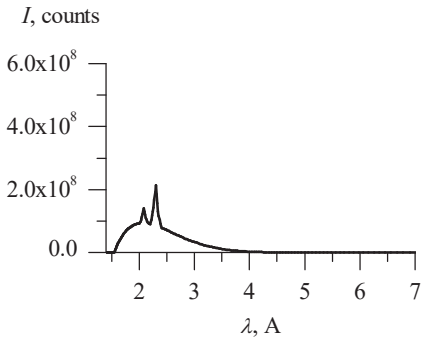

Figure 1.5: *c*. The primary spectrum of an X-ray tube after filtration

Usually, anode Z_a is used for the X-ray tube filter or a material that has an atomic number 2–3 lower than this. In the first case, only the anode characteristic line is present in the primary spectrum. In the second case, the

filter material effectively absorbs the anode line, and the filter characteristic line is observed in the transformed spectrum. In Figure 1.5, *b*, an X-ray tube primary spectrum is shown. In the transformed spectrum (Figure 1.5, *c*), the rapid decrease of the exponent in Eq. (1.18) results in the effective suppression of long-wave bremsstrahlung radiation.

It would be logical to assume that a filter thickness exists that corresponds to a zero background. However, when analyzing small concentrations of an impurity, the spectrum quality will be affected by a background signal, which caused by other factors than continuous spectrum scattering (Section 1.8). This background does not depend on the filter parameters. Consequently, the thickness of the filter can only be increased to a certain limit. Therefore, a problem arises in terms of optimizing the parameters of the filter for the primary radiation; this will be considered in Section 3.1.

Removing an X-ray tube's scattered bremsstrahlung radiation from the long-wave range of the spectrum by filtering favors the identification of light elements due to the reduced background, but it also makes it difficult to obtain a high fluorescence signal intensity due to the low excitation efficiency in the range of medium and short wavelengths (Fig. 1.5, *c*). Therefore, this fluorescence excitation scheme is not capable of theoretically achieving maximum sensitivity of the analysis.

Formation of a primary beam using a secondary target [13, 14]

A scheme with a secondary target differs from the abovementioned filtration scheme in that actions aimed at reducing the background do not require a decrease in the exciting radiation intensity. To excite the atoms

from the sample, a quasi-monochromatic radiation of the secondary target is used, which is excited, in turn, by the entire primary spectrum of the X-ray tube (Fig. 1.6, *a*).

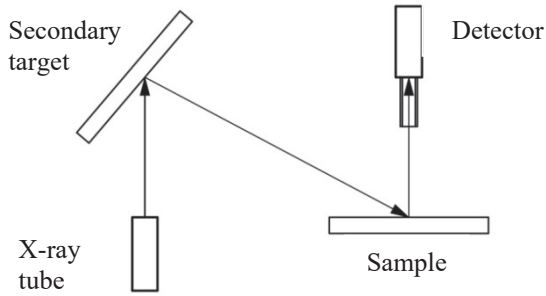

Figure 1.6, *a*: X-ray scheme with a secondary target

The main advantage of this scheme is the high luminosity due to effective use of the X-ray tube radiation pattern. However, here the spectrum monochromatization is not complete; this is because the primary radiation source bremsstrahlung spectrum scattered by the sample is present along with the secondary target fluorescence lines. Each stage of the scattering reduces the background intensity by at least two orders of magnitude. To achieve maximum sensitivity, the target material is chosen so that fluorescence lines of the secondary target have wavelengths a little higher than the absorption edge of the main element of the sample, but with some lower than absorption edges of "trace" elements in the sample (Fig. 1.6, *b*, *c*).

The scheme with the secondary target is unlike the filtration scheme in that it is a finer instrument, which allows you to contrast the lines of certain elements. It also fully corresponds to the theoretical model considered in the beginning of the current section.

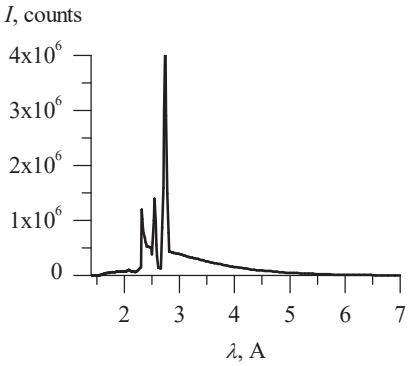

Figure 1.6, *b*: Fluorescence spectrum of a secondary target

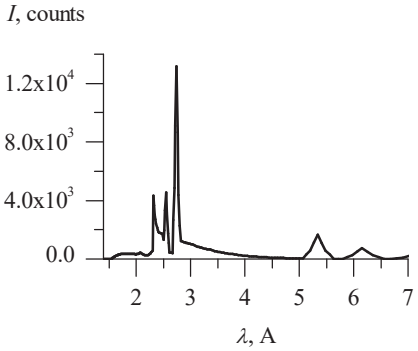

Figure 1.6, *c*: Fluorescence spectrum of a sample in the X-ray scheme from Figure 1.6, *a*

Moreover, one can apply several secondary targets thus increasing the number of lines exciting the fluorescence from impurities that are distanced from each other at the absorption edges. The right combination of primary and secondary targets made from appropriate materials allows us

to achieve a spectrum quality (for certain groups of elements) comparable with the spectra obtained using total external reflection effect (with a detection limit of 10^{-6} % mass [17]).

Excitation of fluorescence in the sample using a tube spectrum monochromatized by the crystal's reflection

The monochromatization of X-rays using the reflection from a single crystal will be considered in detail in the next section, which is devoted to wave dispersion. This is because the reflection from the crystal-analyzer is fundamental for crystal-diffraction spectrometers. Here, we will only focus on X-ray optical schemes with monochromators that are distinguished by a high contrast in the analytical spectrum (~ 10^6…10^7) that, in principle, can provide a sensitivity of 10^{-8} % mass [15]. The main difficulty of this method is obtaining high signal intensity.

In spite of excellent background characteristics, a significant disadvantage of this monochromatization scheme is its narrow range of chemical elements, which are excited effectively by a single line. Therefore, it is difficult to form a primary spectrum that is close to the theoretical because this is connected with a re-adjustment of the crystal-monochromator through the reflection angle. Such a re-adjustment requires precision mechanical devices, and cannot be used in practice.

1.7 Wave dispersion

With wave dispersion, it is possible to achieve the maximum possible values of the spectral resolution determined by the fluorescence line spectral width. To ensure high energy resolution, only $\Delta\theta \approx 1 \cdot 10^{-3}$ is used from the

directional pattern of the fluorescent radiation flux with a half-width of 50…100 deg.: i.e. not more than one thousandth of the energy flux. Such low utilization efficiency of primary radiation forces us to apply sources with the highest possible power; this leads to large dimensions and higher costs with regard to instruments.

To increase the luminosity of the scheme, the broad band excitation of fluorescence of sample elements and the selective detection of outgoing X-rays are used. In this connection, the spectrum formation unit (Fig. 1.4) is absent (this is particularly the case for WDXRF spectrometers); this means that the primary radiation will directly get onto the sample. Less frequently, filtration of the primary radiation occurs and, for special analytical problems, monochromatization uses the reflection from the face of the crystal-monochromator or the fluorescence of the secondary target. There are unique schemes that use fluorescence selective excitation via monochromatic radiation and wave dispersion with bent monochromators; these provide a comparably high luminosity along with spectrum high contrast. These schemes provide a chance to obtain record values for detection limits of between 10^{-4} to 10^{-6} % masses; however, this is only possible for a narrow range of chemical elements with absorption edges close to the excitation energy of the monochromatic radiation [15].

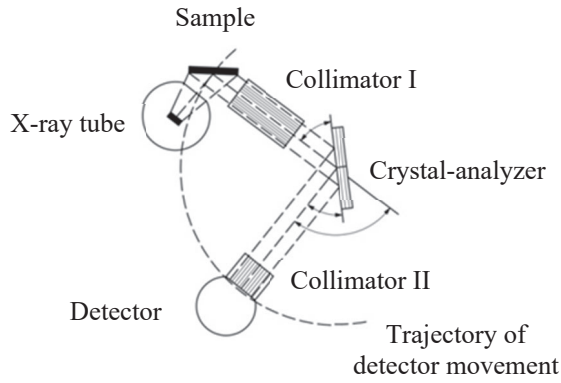

Figure 1.7: A Bragg-Soller spectrometer

The fluorescence radiation from sample atoms gets into the *spectrum registration unit* (Fig. 1.4), passes through the collimator and, when reflected from the single-crystal's crystallographic planes is decomposed in a spectrum, which is registered by a detector (flow-proportional or scintillation). Unlike the primary beam formation, the crystal monochromatizes the fluorescence radiation of the sample, and not the primary radiation of the X-ray tube. Additionally, is not located before the sample but next to it. The crystal-monochromator realizing the wave dispersion is called the *crystal-analyzer* and the efficiency of the whole system depends on its reflection coefficient and perfect structure.

The most widely used detection units are equipped with flat crystal-analyzer and Soller collimators [3] (Fig. 1.7). In this case, it is easy to realize the rotation of the crystal and the movement of the detector in order to change the diffraction angle. In the classical Bragg-Soller scheme [3], the Soller multiplate collimator (Fig. 1.8) is installed behind the large (≈ 10…40 mm) radiator, which provides an angle divergence of $\Delta\theta_{col} = 2b/L$ (where b

is the distance between collimator plates; L is the plate length) for the beam incident on the flat crystal-analyzer. The decomposition of X-rays into the spectrum by the crystal-analyzer occurs according to the Bragg equation: each wavelength λ (n =1) and a set of its harmonics (n =2, 3, etc.) correspond to specific reflection angles θ for crystallographic planes d_{hkl}:

$$\lambda = 2d_{hkl} \sin\theta / n, \quad n = 1, 2, 3\ldots \tag{1.22}$$

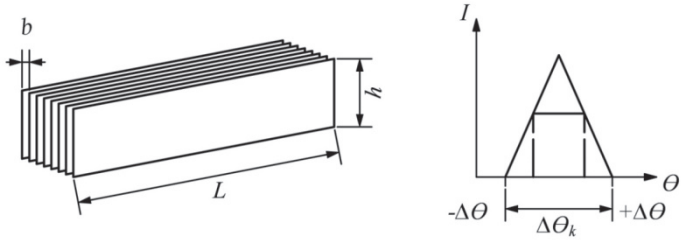

Figure 1.8: Soller collimator scheme (*a*) and the plot of its bandwidth (*b*)

The intensity ratio of the harmonics is determined by the structure factors of the corresponding crystallographic planes d_{hkl}/n [6]. Therefore, when setting the monochromator at an θ angle, the main line λ is allocated from the primary continuous spectrum, and so are its harmonics, λ/2, λ/3, etc. The ratio of intensities of these harmonics can be determined as

$$\frac{\partial\Phi_{03}(\lambda)}{\partial\lambda} \cdot F_{hkl} \Big/ \frac{\partial\Phi_{03}(\lambda/n)}{\partial\lambda} \cdot F_{nh\,nk\,nl}$$

Thus, in some cases, the harmonics' contribution may attain several percent of the monochromatized spectrum's integral intensity. For example, the monochromatization from the LiF (200) crystal gives Cu-Kα, λ = 1.54 Å, sinθ/λ = 0.25, and a structure factor of $F^2_{200} \approx 556$, while the LiF (400)

gives $F^2_{400} \approx 137$. The close values of $\partial\Phi_{03}/\partial\lambda$ give the value 0.246 for the intensity ratio of the second harmonic. The presence of multiple reflections adversely affects the quality of the spectrum due to their superimposition on the sample main fluorescence lines, which are reflected by the first order d_{hkl}. Therefore, the spectrum is usually cleaned by the amplitude discrimination of signals in the detector. However, in some tasks, making an adjustment to measure the intensities of the second and third orders of the reflection may be useful, due to the increased Bragg angle and, respectively, the spectrometer resolution. For example, this adjustment is sometimes used to measure Compton scattered hard radiation in order to move away from the crystal-analyzer's reflection's small angle range.

1.7.1 The energy resolution and efficiency of the WDXRF spectrometer

We will now consider the question of the relationship between the spectral resolution of the WDXRF spectrometer, $\Delta\lambda/\lambda$, and its efficiency. The selection of monochromatic radiation from an arbitrary spectrum requires adjusting the crystal-analyzer to a specific reflection angle, and amending the angular collimation of the beam according to the below equations [3]:

$$\Delta\lambda/\lambda = \cot\theta \cdot \Delta\theta \tag{1.23}$$

$$\Delta\theta = \sqrt{\Delta\theta_{col}^2 + \omega^2} \tag{1.24}$$

where $\Delta\theta_{col} = 2b/L$ is the angular divergence of the collimator and ω is the angular half-width of the crystal rocking curve.

It follows from Eq. (1.24) that the beam angular divergence $\Delta\theta$ is determined by the crystal structure perfection and the angular divergence of the collimator. So, for LiF (002), $\omega \approx 2' = 5.8 \cdot 10^{-4}$ rad, with the optimal choice of $\Delta\theta_{col} \approx \omega \approx 6 \cdot 10^{-4}$ rad at the wavelength $\lambda = 1.54$ Å and $\theta = 22.6$ rad, we obtain $\Delta\theta = 8.5 \cdot 10^{-4}$ rad and the characteristic spectral resolution of the crystal-diffraction instrument: $\Delta\lambda/\lambda = 2.04 \cdot 10^{-3}$. This value is probably close to the maximum achievable in standard crystal-diffraction schemes. In comparison with EDXRF spectrometers, WDXRFs have an order of value better spectral resolution for $\lambda = 1.54$ Å. The gain grows with the increasing wavelength, due to decreasing $\cot\theta$.

An evaluation of efficiency of the primary radiation can be carried out using the formula:

$$\varepsilon = \frac{\Delta\theta_{col}\,\Delta\theta_{AB}}{\Omega^2},$$

where $\Delta\theta_{AB}$ is the divergence of the beam in the anti-Bragg plane, and Ω is the angular half-width of the primary beam.

The divergence in the anti-Bragg plane, $\Delta\theta_{AB}$, can be set by a factor 3÷5 higher than $\Delta\theta_{col}$ without significant loss of the spectral resolution [4]. Then, with a value characteristic of $\Omega \approx 1.22$ rad for the X-ray tube, we obtain a very small value for the primary radiation efficiency—$\varepsilon = 0.0045 \cdot 5 \cdot 0.0045 / (1.22)^2 = 6.9 \cdot 10^{-5}$—even for schemes with focusing monochromators, $\varepsilon < 1 \cdot 10^{-3}$ [10].

The efficiency of monochromatization is evaluated in a similar way. In standard schemes for X-ray spectrometers, the Bragg angle θ is less than 45 deg.: i.e., $\cot\theta \geq 1$. Therefore, in order to obtain an acceptable spectral resolution, $\Delta\lambda/\lambda < 1\%$, it is necessary to provide a collimation system angular divergence of $\Delta\theta < 0.001$ rad. The influence of the angular divergence in the anti-Bragg plane on the spectral resolution of the wave-dispersion instrument is several times less than the divergence in the Bragg plane, $\Delta\theta_{col} = 2b/L$, although its contribution into $\Delta\lambda/\lambda$ is also proportional to $\cot\theta$ [3]. This allows for setting the divergence in the anti-Bragg plane $\Delta\theta_{AB}$ by a factor 3÷5 higher than $\Delta\theta_{col}$ without noticeable loss of spectral resolution in order to increase the luminosity [3]. At the same time, the efficiency of separating the monochromatic component from the X-ray spectrum remains extremely low. Indeed, with the angular half-width $\Omega \approx 1.22$ rad of the diagram of the radiation emitted from the sample surface, the wave-dispersion spectrometer can select a portion of $\varepsilon = 2.6 \cdot 10^{-6}$ to provide spectral resolution at the level of $2 \cdot 10^{-3}$. If we consider that the reflection peak coefficient of known crystal-analyzers does not exceed $R = 0.3$, the efficiency of this monochromatization, $\eta = \varepsilon R$, is not more than one millionth of the sample X-ray spectrum. Thus, wave-dispersion spectrometers have high resolution, but require quite powerful sources of primary radiation and precision goniometers that result in their large sizes, complexity, and high costs.

1.8 Dispersion by quantum energies: characteristics of solid state detectors for X-rays

Energy-dispersion XRF methods began to be developed with occurring solid-state semiconductor diode detectors and related pulse-processing

circuits [13]. The solid-state detectors, unlike flow-proportional or scintillation ones (with which crystal-diffraction spectrometers are equipped) simultaneously register the entire spectrum of the sample fluorescence, which is called a broadband detection. The separation of X-ray quanta by energies takes place in the detector. Each energy value corresponds to the certain amplitude of the pulse created by the detector and registered by the electronic circuit. In EDXRF spectrometers, the parallel accumulation of the spectrum is realized: i.e. radiations with different wavelengths are simultaneously registered by the detector and form the spectrum [13]. This important advantage sometimes allows us to reduce the spectrum accumulation time by orders of value. Additionally, the absence of complex collimation systems provides a possibility to place the detector close to the sample. The small distance "sample-detector" maximizes the directional diagram of the sample radiation in the detector window and minimizes the losses due to the air absorption of the fluorescence spectrum of the long-wavelength range. This makes it possible to work without vacuuming and to use low-power sources of the primary radiation, which significantly simplifies the cooling and protective systems. Evidently, the energy-dispersion systems should be used with the portable X-ray equipment [13].

However, intense lines of basic components and their artifact peaks with the spectrum parallel accumulation (Sect. 1.8.2), which can be mistakenly identified as an analytical signal; this can have a negative effect on the sensitivity. The intense lines give the main load to the detector and make it difficult to measure the intensities of the weak lines of "trace" impurities. Modern solid-state silicon based detectors successfully work in an energy range of 1 to 30 keV with loading not more than $1…2 \cdot 10^4$ photons/s with a pulse duration > 2 μs. At larger fluxes, we have to reduce the pulse dura-

tion in order to avoid a sharp increase of the dead time. Increasing the spectral line half-width and an unacceptable loss of the energy resolution follow the reduction of the pulse duration. Let us assume that the detection of the trace impurity analytical line requires at least 100 pulses. At an impurity concentration of 1 ppm (10^{-6}), the accumulation of pulses for the entire spectrum is $100/10^{-6} = 10^8$ counts. With a counting speed of 10^4 counts /s the minimum exposure is about 10^4 s.

The limitation of the detector integral load leads to the need for long exposures not only to identify weak lines of trace impurities but also to determine the precision measurements of Compton and Rayleigh scattering intensities, as well as the sample's main components' fluorescence lines.

1.8.1 Energy resolution and efficiency of solid- state detectors

A solid-state detector is a cylindrical crystal of silicon or germanium with metalized ends (electrodes). The electrical potential (about 500 V) of the electrodes draws the most out of the charge carriers from the intrinsic conductivity band, thereby creating a depletion region sensitive to ionization radiation. In the absence of irradiation, the material's semiconductor properties permit the passage of a very low current. An X-ray photon penetrating into the semiconductor creates a series of electron-hole pairs that move towards the electrodes under the action of the electrical field. As a result, a charge is created. This electrical pulse provides an informative base from which to detect both the event and to measure the energy of the absorbed photon. The charge collected at the detector electrodes is proportional to the number of electron-hole pairs: i.e. to the energy emitted by the photon under absorption in the sensitive layer. The average energy need for the formation of an electron-hole pair in the semiconductor is low (3.8 eV for

Si and 2.9 eV for Ge) in comparison with measured energies (0.1…30 keV), which allows us to use a spectrometer with a high resolution. If the photon energy is completely absorbed in the sensitive layer, the registration efficiency is close to 100%. High-energy photons have a high probability of going outside the detector, which means the registration efficiency decreases. When there is constant photon energy, the number of formed electron-hole pairs undergoes statistical fluctuations because of the presence of defects, impurities, and other factors. This leads to a variation in the pulse amplitude for characteristic X-ray photons, which is expressed as the *energy resolution* of the detector.

Two kinds of materials are used to manufacture the crystals for the detector: silicon and germanium. In order to compensate for the effect of minor impurities on the conductivity, the silicon crystals are doped by lithium atoms; thus a material with a high intrinsic resistance is formed, which is denoted as Si(Li): drift silicon-lithium detectors. Under the action of an electrical field, Li ions move to the *p*- areas of the *p*-*n* junction, where they compensate the acceptors and create a wide sensitive zone of intrinsic conductivity, where width is set by the Li ion diffusion depth and is able to attain 5 mm. An advantage of these detectors is their good resolution for both high and low energies, as well as their high efficiency of absorption within the whole range of XRF energies (to 20…40 keV). Early models of Si(Li) detectors (produced before the 1990s) required liquid nitrogen to function, otherwise they could degrade due to lithium diffusion. Modern technologies allow for manufacturing thermo-cycling Si(Li) detectors: i.e. they can be left without cooling for a rather long time.

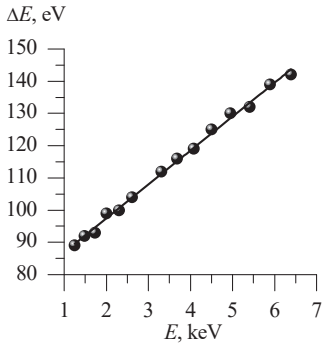

Figure 1.9: The energy resolution of a SDD X-123 (Amptek) detector. The data was obtained in the present work.

Another material is high purity germanium (HpGe). It has the advantage of absorption efficiency when measuring high-energy radiation (to MeV). Over the past 20 years, new modifications of silicon detectors occurred, such as Si PIN [18] and Si-compensating Si-drift detectors (SDD) [19], which provide higher speeds for counting and better spectral resolution in comparison with Si(Li). Our results from studying the energy resolution of a modern SDD X-123 produced by Amptek (USA) are shown in Figure 1.9 [20]. The fluorescence line half-width for single-component samples determined the energy resolution. We obtained the dependence of the energy resolution in photon energies using the following empirical formula:

$$\Delta E[\text{eV}] = 10.529\, E\,[\text{keV}] + 76.376\,[\text{eV}]. \tag{1.25}$$

As the energy decreases, the energy resolution approaches the theoretical background limit of ≈ 80 eV. In the considered energy range, the experimental ΔE is only 10–15% higher than the theoretically possible spectral resolution.

The spectral resolution of the EDXRF spectrometer in the range of 1 to 7 keV is better (8.5 to 2.2%) but remains at least an order of magnitude worse than in the WDXRF. However, EDXRF spectrometers are characterized by their high efficiency. Indeed, due to the close location of the detector to the sample surface, it is possible to capture a significant part of the fluorescent radiation from the sample. So, with an area of $S \approx 7$ mm^2 for the X-123 detector window and a "sample-detector" distance r =5 mm, the capture efficiency of the radiation with the angular pattern half-width $\Omega \approx 1.22$ rad is $\varepsilon = \frac{S}{r^2\Omega^2} = 0.19$, which is five orders of magnitude higher than in the WDXRF. Such high efficiency makes it possible to use low-power primary radiation sources for the EDXRF and to create low-cost portable instruments.

1.8.2 Spectrum artifacts

Now we will consider some specific features of spectra obtained in the EDXRF. These features are should be taken into account when treating and obtaining quantitative results [13].

Peaks of loss

When X-rays with energy higher than the Si-K absorption edge enter into the detector, the fluorescent radiation of the detector material is observed. Its main portion is absorbed in the detector volume and contributes to the total charge collected from the initial incident X-ray photon. However, there is a finite probability that the Si-K_α radiation will leave the detector

volume and not contribute to the charge collected from the initial detected photon. The resulting detected energy is reduced by 1.740 keV, which corresponds to the lost Si-K_α radiation energy. The greatest probability of extinction exists near the end of the detector crystal. The probability of the Si-K_β generation is extremely low, and so this effect is negligible. The result of Si-K_α radiation leakage is an additional spectral peak, which is 1.74 keV lower in energy than the initial one. Usually its intensity is 0.5–1% of the main peak. It is more important to take this phenomenon into account in low energy ranges of 1 to 3 keV, where the peaks of loss can be misinterpreted as lines from *L*- and *M*-series of elements, which are not present in the sample.

Cumulative peaks

Cumulative peaks appear when two photons enter the detector in such a short time interval that the device is not able to recognize them as two events. This effect is manifested in the fact that the sum of the energy emitted from two analytical signals is registered as a single event. Additionally, the lines' intensity ratio does not correspond to that of the *K*-series characteristic lines. Consequently, the cumulative peaks are misinterpreted as elements and may interfere with important lines in a particular analysis. This is of high importance for analyses in the field of ecology; for example, a high Fe concentration gives intense Fe-*K* lines, which result in cumulative Fe-*K* peaks in the range of *K*-lines for Se and Br, as well as in the range of *L*-lines for toxic heavy elements, such as Hg, Tl, and Pb.

Diffraction peaks

When analyzing crystalline samples, the possibility of Bragg conditions exist, which are caused by the divergent geometry of the incident and detected beams. The higher the degree of X-ray monochromatization, then the less likely it is that diffraction reflections will occur. It is often enough to incline or rotate the sample to minimize diffraction peaks. Besides, we can use an additional collimation in order to cut off the angles satisfying Bragg conditions, or apply fluorescence excitation schemes, which change or reduce the incident energies causing the diffraction. An increase in the voltage and the application of a filter for primary radiation completely changes the energy distribution of the excitation spectrum and removes the artifact.

Peaks of contamination in the system

To eliminate lines of false elements in analytical spectra, all the spectrometer's units and components should be carefully shielded. Each manufacturer applies specific shielding materials; therefore, there are a variety of potentially contaminating peaks in the spectrum. For example, beryllium entrance windows usually contain some trace elements that can be observed in background spectra. The application of thick beryllium windows aggravates this potential problem. The most probable source of false spectral peaks is the quality of the samples, which is mainly controlled by the user.

1.8.3 Thickness of the detector active region

As the detected radiation energy increases for hard X-rays with a wavelength pf $\lambda < 1$ Å, the efficiency of absorption in the material of the detector active region is markedly reduced because the thickness of the active region is, as a rule, significantly less than the detector silicon plate thickness and is determined by the depth of the doping zone and the work conditions. To find the correct quantitative measurements in a wide wavelength range, you need to know the value of the active region and introduce corresponding corrections into measured intensities [21].

The thickness of the active region can be determined experimentally by measuring the known fluxes of the monochromatic radiations. This work is very laborious because it requires a readjustment of the spectrometer X-ray scheme. The problem is simplified, if the fluorescence radiation fluxes of the analytical lines from single-component samples are used as tknown fluxes when they are excited by the monochromatic radiation of a secondary target.

The intensity of fluorescence of a single-component target excited with a monochromatic radiation, I_0, corresponds to [1, 10], is written as

$$I_i = \frac{S}{4\pi r^2} I_0 \left(1 - \frac{1}{S_{q_i}}\right) \omega_i p_i \sin\varphi \frac{1}{\left(1 + K\dfrac{\mu_{ii}}{\mu_{0i}}\right)} = \frac{S}{4\pi r^2} I_0 R_i, \tag{1.25}$$

where $\dfrac{S}{4\pi r^2}$ is the solid angle of the sample illumination; S_{qi}, ω_I, and p_i are, respectively, the absorption jump value, the fluorescence yield, and a

portion of intensity of the *i*-th line in the spectral series; μ_{0i} and μ_{ii} are mass attenuation coefficients for the secondary target monochromatic radiation and for its fluorescence radiation, respectively; and $K = \sin\varphi/\sin\psi$.

The efficiency of the detector is determined as

$$F_i = \left(1 - \exp\left(-\mu_i \rho t\right)\right)$$

where μ_i is the attenuation coefficient of the *i*-th analytical line in the material of the detector active region (Si); $\rho = 2.3$ g/cm^3 is the detector material density (silicon); and *t* is the thickness of the active region.

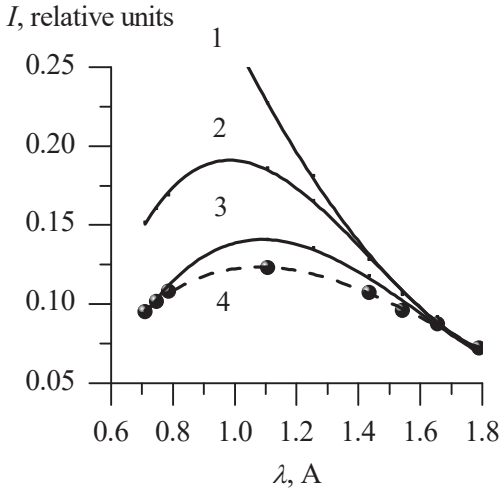

Figure 1.10: K_α analytical line intensity versus wavelength dependences obtained for a one-component sample using detectors with different thicknesses *t* of the Si-pin active region. Calculated curves: 1, $t \to \infty$; 2, – t = 300 μm; 3, t = 170 μm; and 4, experimental curve.

According to Eq. (1.25), with the detector's 100% efficiency, the intensity of chemical element analytical lines should decrease monotonically with wavelength increasing (Fig. 1.10, curve 1).

To reveal the real dependence $I(\lambda)$, the fluorescence radiation of single-component samples with atomic numbers from $Z = 27$(Co) to $Z = 42$(Mo) was excited by the radiation of the high purity silver secondary target. As a result, the curve shows non-monotonicity with a maximum close to $\lambda \approx 1.15$ Å. This is due to the passage of hard radiation across the active region of the detector without absorption and the creation of current pulses. If the active region of the detector was to extend over its entire thickness of 300 μm, the registered intensity of the Mo-K_α ($\lambda = 0.71$ Å), Nb-K_α ($\lambda = 0.74$ Å), and Zr-K_α ($\lambda = 0.78$ Å) analytical lines would be twice as large as the intensities of the Cu-K_α ($\lambda = 1.54$ Å) and Ni-K_α ($\lambda = 1.65$ Å) lines (Fig. 1.10, curve 2). The maximum of the curve would be $\lambda = 1$ Å. Reducing the thickness of the active region, in accordance with formula (1.26), results in a decrease of this ratio and a shift of the curve maximum toward larger wavelengths (Fig. 1.10, curve 3). The matching of the experimental (4) and calculated (3) curves makes it possible to determine the thickness of the active region $t = 170$ μm with an accuracy of ±10 μm.

Thus, the active region of the Si-pin detector is half its thickness, which requires the introduction of appropriate corrections to the optimization calculations.

Conclusion to Chapter 1

The spectrometers of wave and energy dispersion modes differ in the conditions of the spectrum accumulation: in the first case, the spectrum is obtained sequentially by scanning and the crystal analyzer is tuned at each step to measure the intensity of the spectral line of a certain wavelength; in the second, the entire spectrum is detected simultaneously. In principle, the energy resolution of the wave spectrometer's spectrum is limited by the spectral line width, which is very small: $\Delta\lambda/\lambda < 5 \cdot 10^{-4}$. For *K*-, *L*-, or *M*- series lines in most chemical elements it is possible to select crystals-analyzers with a reflection angle about 60–70°, which provides a 2 to 3 fold decrease in the aperture component, $\Delta\lambda/\lambda$, according to Eq. (1.23) and (1.24). The practically achievable value $\Delta\theta \approx 2$ mrad provides a spectral resolution of $\Delta\lambda/\lambda \sim 1 \cdot 10^{-3}$ in commercial WDXRF spectrometers, which is an order of magnitude better than in EDXRF instruments. The possible reduction of $\Delta\theta$ is caused by the power of the primary radiation source, the crystal-analyzer reflectivity, and its rocking curve width. Since the manufacturer of X-ray tubes determines the power of the primary radiation source, the choice of a crystal-analyzer with respect to the reflectivity and structure perfection remains at the disposal of the experimenter in order to increase the sensitivity of the analysis. Chapter 2 will consider various ways to solve this problem.

The basic difference of an EDXRF spectrometer in comparison with a WDXRF one is the principle of the spectrum formation, where the detector simultaneously records radiations of different wavelengths. A serious disadvantage of solid-state detectors is their low energy resolution. Although, in a modern SDD the $\Delta E/E$ value approaches the theoretical limit of 2.0 %

(for E = 5.89 keV), this is several times worse than found in wave spectrometers. Additionally, under the simultaneous accumulation of the spectrum, the scattered broadband spectrum of the tube, lines from the sample's main components, and their artifact peaks negatively affect the sensitivity of the analysis. The modern Si-based solid-state detectors work well in an energy range of 1 to 30 keV with a load not more than 1 to $2 \cdot 10^4$ photons/s and a pulse duration of > 2 μs. The limitation of the detector integrated load leads to the need for long exposures not only for detecting weak lines of "trace" impurities, but also for precision measurements of Compton and Rayleigh scattering and fluorescence in the sample's main components.

In connection with the above, the broadband excitation with the primary spectrum of the X-ray tube in the energy-dispersion analysis may be only applied when solving comparably simple tasks, such as measuring the intensities of elements whose lines are not less than 0.01 to 0.1 % of the entire spectrum's intensity. Solving complex problems when detecting weak signals of trace impurities requires the elimination of the detector stray load; this then stimulates the application of selective excitation, which has been specially calculated as the optimal solution for the specific technical problem.

The larger aperture is an advantage of the EDXRF; therefore, high luminosity will be due to the dense arrangement of the X-ray optic scheme components. So, the EDXRF spectrometer captures about 20 % of the fluorescence radiation emitting from the sample surface, whereas the wave-dispersion one is only able to capture about $3 \cdot 10^{-4}$ %: i.e., tens of thousands times less. It is the high luminosity of EDXRF instruments that

makes it possible to apply selective excitation schemes coupled with a large loss of intensity.

New complex selective excitation schemes that minimize the stray load of the detector and provide a high contrast in the fluorescence spectrum for a wide range of *Z* will be considered in Chapter 3.

CHAPTER 2

WAVE-DISPERSION X-RAY FLUORESCENCE ANALYSIS

The basic components of WDXRF instruments are crystals-analyzers and collimation systems. This chapter focuses on new developments in these components and their influence on increasing the sensitivity of WDXRF analysis.

2.1 The main characteristics of traditional crystal-analyzers

It is impossible to cover the entire range of analytical element lines; therefore, several crystals with different interplanar distances d are used in X-ray spectrometers. In practice, a very limited assortment of crystals is used as crystal-analyzers that meet the requirements of stability, high reflection coefficients, and structural perfection. The characteristics of traditional crystal analyzers are given in Table 2.1 [4].

In the short-wave range of the spectrum, LiF [200] crystals are used and, if you need a higher resolution, LiF [220] crystals, which have a slightly smaller integral reflection coefficient but a higher dispersion, can be applied. In particular, the Soller scheme with LiF [220] provides the possibility of reducing the superimposition of K_β-lines for elements with Z = 24÷30 on K_α-lines in (Z+1) elements, as has been observed through analogous channels with Li[200] crystals.

Table 2.1: Characteristics of main crystal-analyzers applied when performing the "reflection" mode of measurements

№	Crystal [plane]	2*d* Å	Wave range Å	Element range *Z*	Mosaicity rad·10^4	Integral reflectivity rad·10^5
1	LiF [200]	4.027	0.5-3.8	19–50(K) 51–94(L)	20	40
2	LiF [220]	2.848	0.3-2.7	22–56(K) 57–94(L)	20	20
3	EDDT [020]	8.803	7-8.5	13–14(K)	6	18
4	PE [002]	8.750	3-8.5	13–21(K)	2	8
5	Ge [111]	6.532	4.5-6.5	15–17(K)	3	20
6	ADP [101]	10.642	9-10	12(K)		
7	KAP [100]	26.632	11-25	8–11(K)	1.5	2.0
8	RAP [100]	26.121	9-25	8–12(K)	3	6
9	Stearates	60–100	30-100	5–8(K)	100	30
10	Graphite [002] (pyrolytic)	6.719	4.5-6.5	15–17(K)	120	440
11	Quartz [1011]	6.686	0.6-6.5	15–47(K)	3	15
12	TlAP [100]	25.75	9-20	8–14(K)	No data	
13	InSb [111]	7.48	6-7.2	14(K)	No data	
14	Artificial pseudocrystals	20–120	5-100	5–16(K)	No data	

Until now, crystals from K, Na, Rb, Tl, and NH_4 phthalates with an interplanar distance of d ≈ 13 Å in the wavelength range λ of 4 to 25 Å were used, which, for λ of 4.5 to 13 Å, gave line intensities that were a factor 8–13 higher than with mica. At the same time, crystal TlAP reflects Mg-Kα and Na-Kα radiations twice as efficiently as KAP and RbAP crystals, and

F-Kα and O-Kα reflect a factor 3–5 more efficiently than the KAP crystal. A crystal of lead stearate $[CH_2(CH)18COO]_2Pb$, which is a synthetic multilayer film, was used for the spectral decomposition of the X-ray radiation with wavelengths of 9 to 96 Å. However, the listed long-period crystals showed instability in their peak reflectivity [4].

The technology for multi-layer X-ray mirrors (MXM) has developed rapidly since 1980 [22]. To date, multilayer structures have almost supplanted long-period crystals due to their higher peak reflection coefficients and high stability. MXM are widely used for monochromatization of not only synchrotron radiation, but also for the radiation of X-ray tubes in diffractometers in order to perform structure analysis. However, MXM were only applied relatively recently in XRF because of the complexity of their setting in standard X-ray optic schemes. In Section 2.6, we will consider the application of short-period X-ray mirrors in WDXRF in detail, as well as the corresponding modernization of X-ray optic schemes in order to obtain spectra in the wavelength range of 5 to 67 Å.

2.2 Criterion for selecting materials for monochromators with a high reflectivity

it is useful to have a general criterion for a purposeful selection of materials for monochromator crystals with a high reflection coefficient. This is the value of the integral reflection coefficient, which depends on the monochromator material, the type of its crystal lattice, and the volume of the unit cell [23]. In this section, we will establish the general criteria needed when selecting materials for monochromators.

According to the kinematic theory, the integral intensity of a Bragg reflection is determined by the expression [6]:

$$\rho_{hkl} = 7{,}9 \cdot 10^{-26} \frac{\lambda^3}{2\mu\,\rho\,V^2} \cdot \frac{1+\cos^2 2\theta}{2\sin 2\theta} |F|^2 , \qquad (2.1)$$

where λ is the wavelength; θ is the Bragg angle; V is the volume of a unit cell (cm^3); μ is the mass absorption coefficient (cm^2/g); ρ is the density (g/cm^3); and $F(hkl)$ –is the structure factor.

The absence of absorption jumps in the operating wavelength range of the monochromator material means that it is convenient to present μ in the following form (according to Eq. [1.5]):

$$\mu = \sum_i G_i \; p_i \; \lambda^{\alpha} \; Z_i^{\beta} , \qquad (2.2)$$

where p_i is an empirical coefficient.

In the range of chemical elements with numbers Z from 3 to 10, the values $p = 5.4 \cdot 10^{-3}$, $\alpha \approx 3$, and $\beta = 3$ [24] are constant. The X-ray density of the monochromator substance is calculated using the following relation [25]:

$$\rho = \frac{1.6604 \cdot M \cdot n}{V} = \frac{1.6604 \cdot n}{V} \cdot \sum_{j=1}^{m} k_j A_j$$

$$M = \sum_{j=1}^{m} k_j A_j \qquad (2.3)$$

where M is the molecular weight of the compound (atomic weight A_j for a single-component material); n is the number of molecules in the unit cell; and V is the volume of the unit cell. The summation is carried out by all m

elements of the molecule chemical formula. k_j are coefficients in the chemical formula (for example, CaF_2: $k_1 = 1$, $k_2 = 2$; $m = 2$).

Let us consider the maximum possible value of the structural factor for a chemical compound with a cubic lattice:

$$F^2 = n^2 \left(\sum_{j=1}^{m} k_j f_j \right)^2 , \tag{2.4}$$

where f_i is the atomic factor for the j-th element of the chemical formula.

We transformed the expression (2.1) making allowance for (2.2), (2.3), and (2.4) and, when omitting the numerical factors and the polarization factor, we obtain:

$$\rho_{hkl} \sim \frac{n \cdot \left(\sum_{j=1}^{m} k_j f_j \right)^2}{V \cdot \sum_i C_i Z_i^3 \cdot \sum_{j=1}^{m} k_j A_j} , \tag{2.5}$$

where $C_i = \dfrac{k_i A_i}{\sum_j k_j A_j}$ is the mass fraction of the i-th element.

Let us examine the dependence of the expression (2.5) on the atomic number taking into account $A_i \approx 2Z_i$. According to [6], $f = Z \cdot \Phi(Z)$, $\Phi(Z)$ weakly depends on Z. So, in the practically important range of interplanar distances of monochromators, $\sin\theta / \lambda \leq 0.25$ (Å^{-1}), the dependence $\Phi(Z)$ is weak-

er than that of Z and, therefore, we must neglect it. Then, taking into account $f_j \sim Z_j$, we obtain the following reflection coefficient:

$$\rho_{hkl} \sim \frac{n}{2} \cdot \frac{\left(\sum_{j=1}^{m} k_j Z_j \right)^2}{V \sum_{j=1}^{m} k_j Z_j^4} . \qquad (2.6)$$

This formula (2.6) is the criterion for selecting a monochromator material, because it only contains the parameters of the material. Two important conclusions follow from (2.6): firstly, the reflection coefficient increases inversely with the square of the atomic number for single-component materials and, secondly, optimal ratios of atomic numbers of elements in the chemical compound may exist for multi-component materials.

The optimal ratios are determined from the condition of equality to zero of partial derivatives: $\partial\rho_{hkl} / \partial Z_i = 0$. When differentiating (2.6) with respect to Z_i, we obtain

$$\sum_j k_j Z_j \left(Z_j^3 - 2Z_i^3 \right) = 0 . \qquad (2.7)$$

This system of equations has a specific solution for multi-component compounds. For example, for AB type binary compounds ($k_1 = 1$, $k_2 = 1$) we obtain the solution, $Z_2 / Z_1 = 1.396$; similarly, for A_2B binary compounds ($k_1 = 2$, $k_2 = 1$), we have $Z_2 / Z_1 = 1.495$, etc.

Based on these solutions and taking into account the fact that elements with low Z should be selected, we compiled a list of promising mono-

chromators (Table 2.2) among single-component materials and binary compounds with cubic lattice.

Table 2.2: The most promising materials for creating monochromators for two ranges of X-ray wavelengths [23]

λ range, Å	Material	Criterion	2*d*, Å	Structure type
0.4÷4	LiH	$5.7\ 10^3$	4.09	K5
	Li	$2.57\ 10^3$	3.51	K1
	Be_2C	$1.35\ 10^3$	4.34	K6
	Li_2O	$0.93\ 10^3$	4.63	K6
	C	$1.22\ 10^3$	6.70	H
	LiF	$0,67\ 10^3$	4.02	K5
	SiO_2 (β-crystobalite)	$0.21\ 10^3$	7.136	K8
4÷12	Be_3N_2	$0.90\ 10^3$	8.146	K16
	B_2O_3	$0.17\ 10^3$	10.06	K
	C_{60}	$0.11\ 10^3$	16.36	K4

Taking into account the differences in the lattice periods, it is appropriate to group the materials according to the principle of their applicability in the two most important X-ray spectrum ranges (Table 2.2): λ = (0.4÷4) Å, where the element lines from K (Z= 19) to U (Z= 92) are located, and λ = (4÷12) Å, where element lines from Na (Z=11) to Cl (Z= 17) (the third line of the Periodic Table) are present.

Therefore, for the range $\lambda = (0.4 \div 4)$ Å, potentially the best selection is lithium hydride, whose integral reflection coefficient is several times larger than for graphite and LiF monochromators. Currently, only monochromators made from C (pyrolytic graphite), LiF, and SiO_2 exist, of which graphite is the best. Therefore, creating highly perfect LiH single crystals would be a significant step in the development of XRF analysis for the wavelength range $\lambda = (0.4 \div 4)$ Å.

Unfortunately, due to the low structure perfection of pyro-graphite (the rocking curve width is less than 0.4 deg.), the application of this monochromator in the WDXRF standard scheme is impossible because of the poor quality of the spectrum obtained. In connection with this point, in Section 2.3 we will consider the modernized Bragg-Soller scheme, which allows the use of crystals with low structure perfection in order to obtain high-quality spectra.

Only one of the indicated prospective crystal-analyzers was created for the wavelength range $\lambda = 4 \div 10$ Å; this was based on fullerite C_{60} epitaxial layers. The structure characteristics of the C_{60} monochromator in comparison with traditional KAP are presented in Section 2.5.

2.3 The application of high-efficiency crystal-analyzers with low structure perfection, and an X-ray optic scheme with two Soller collimators

In order to measure the intensity of the brightest analytical lines from different elements, the X-ray fluorescence spectrometer should work in a very wide range of wavelengths from at least 0.35 to 70 Å. The lower spectrum edge is technically limited by the X-ray tube working voltage

which, as is usual in commercial instruments, does not exceed 40÷50 kV. When scanning crystal-diffraction spectrometers, the short-wave edge requires low θ angles because high-efficiency crystal-analyzers with small interplanar distances are absent. For current analyzers (Table 2.1), the crystal LiF (220), $2d$ = 2.848 Å for measurements of $\lambda \cong 0.3$ Å should operate at a Bragg angle of $\theta = 6°$.

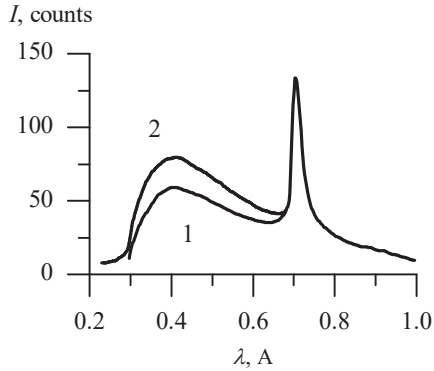

Figure 2.1: Background level for two schemes of the spectrometer: 1, modernized scheme with two collimators; 2, traditional Bragg-Soller scheme

In the last decade, significant progress has been made in the production of crystal analyzers from pyrolytic graphite, $2d$ = 6.70 Å [26]. The integral reflectivity of these analyzers is, at least, an order of magnitude higher than for other crystals (Table 2.1), and the rocking curve half-width is reduced to 0.4°. Additionally, short-period ($2d$ = 30÷60 Å) mirrors recently developed for the range λ = 6÷20 Å have reflection coefficients that significantly exceed that of all known natural crystals. All these crystal-analyzers require measurements at low angles, but this is impossible in the

Bragg-Soller scheme because of the significant increase in the background (Fig. 2.1).

Let us consider the modernization of the classical Bragg-Soller scheme, which has the potential to obtain high-quality spectra using crystals with poor structure perfection at low diffraction angles [27]. The $\Delta\lambda/\lambda$ value is determined by the spectrum registration's technical conditions; this is used for the $\Delta\theta$ calculation. For example, to separate the lines Cr-K_β, $\lambda = 2.088$ Å and Mn-K_α, $\lambda = 2.102$ Å using the LiF(200) crystal-analyzer with $2d = 4.027$ Å and the rocking curve width $\omega = 0.1°$, we need (in accordance with Eq. [1.24]) a collimator with a divergence no greater than $\Delta\theta_1 = 0.21°$. So, the separation of these lines is impossible with a graphite (002) crystal-analyzer of $2d = 4.027$ Å and $\omega = 0.4°$ in the Bragg-Soller scheme because the necessary divergence $\Delta\theta = 0.126°$ is less than the graphite rocking curve width.

In [28], the possibility to significantly reduce the rocking curve half-width of a mosaic crystal is substantiated. This decrease is possible due to the fact that the reciprocal lattice site size along the normal to the diffraction vector of the crystals with poor structure perfection is much smaller than the site radial blurring, which is determined by the mosaic block misorientation.

To avoid the broadening of diffraction reflections due to these misorientations, the spectrum should be recorded in the θ–2θ-scanning mode with narrow slits. As follows from the Ewald structure, a reciprocal lattice site is dissected along the diffraction vector in this mode, and the site blurring

in the radial direction does not influence the half-width of the diffraction reflection. In this case, the physical broadening of the spectral line, $\beta_{\theta-2\theta}$, is only determined by the size L of blocks along the normal surface and the inhomogeneity, $\Delta d/d$, of interplanar distances:

$$\beta_{\theta-2\theta} = \sqrt{\left(\frac{\lambda^2}{L^2 \cdot \cos^2\theta} + 16\left(\frac{\Delta d}{d}\right)^2 tg^2\theta \right)}. \tag{2.8}$$

In a single-crystal $L \geq 10^4$ Å and $\Delta d/d < 10^{-4}$; therefore, when recording $\theta \leq 30°$, the line broadening $\beta_{\Delta\theta-2\theta} \leq 0.015°$ is found to be at least an order of magnitude lower than the practically attainable beam divergence, while the value β_ω, which is caused by the misorientations, can reach 0.4° for pyrographite. Let us consider the passage geometry of the diffracted beams in the scheme with two Soller collimators using the example of one pair of cells (Fig. 2.2) [27].

Using Bragg-Brentano focusing, we draw an auxiliary circle from the center at the point O with the radius $R = OF$ (the point F corresponds to the position of a slit in the classical construction). The horizontal arrangement of the crystal corresponds to the Bragg condition for the central ray in the point O, then $R = 0.5\ L_1 + l_0$, where l_0 is the distance between the collimator and the point O on the crystal. As the crystal rotates counterclockwise, the reflection begins in the point A, for which, first of all, the Bragg conditions are realized: $\theta_A = \theta_{Br}$. In this case, the angle φ_1 between the crystal surface and the horizontal plane is $\varphi_1 = -b_1 / (L_1 + l_A)$, where l_A is the distance between the collimator and point A on the crystal, b_1 is the distance between plates of the first collimator, and L_1 is the length of plates of the first col-

limator. The angular divergence is equal to $2\theta_{Br} - 2b_1 / (L_1+l_A)$. Therefore, for θ-2θ scanning, the coordinate of the center of the detector collimator, *P*', is given by the arc *F*'*P*', which corresponds to the detector rotation angle: $2\theta = 2\theta_{Br} - 2b_1 / (L_1+l_A)$. The reflected signal from point *A* falls into point *P*, which is out of the zone of transmission, *M*'*N*' = b_2, of the second collimator: i.e. the signal is not detected by the detector. When turning the crystal in the range *MN* = b_1, all the rays passing through the first collimator (arbitrary points F_1, F_2, etc.) are focused on the auxiliary circle (points P_1, P_2, etc.).

When the crystal rotates, the *M*'*N*' zone moves at double speed along the auxiliary circle. When point *M*' coincides with *N*, the diffracted rays begin to fall into the transmission zone and they come out of this zone (the reflection disappears) when point *N*' coincides with *M*. Thus, the signal is observed in the angle range from

$$2\theta_{\min} = \left(2\theta_{Br} - \frac{(b_1 + b_2)}{2R}\right) \text{ to } 2\theta_{\max} = \left(2\theta_{Br} + \frac{(b_1 + b_2)}{2R}\right),$$

where b_1, b_2 are the distances between the plates of the first and second collimators, respectively, and *R* is the radius of the auxiliary circle.

The width at half-maximum height expressed in Δθ is

$$\Delta\theta = \frac{(b_1 + b_2)}{4R}, \tag{2.9}$$

This is significantly lower than the value obtained by Eq. (1.24).

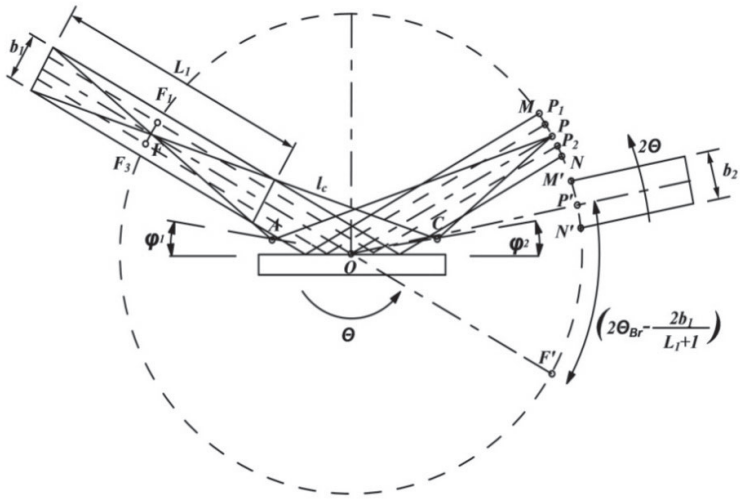

Figure 2.2: Geometrical representation of diffraction conditions in the scheme with two Soller collimators and one pair of cells.

From these constructions, (Fig. 2.2) we can see that in the peak of the reflection curve, where Bragg conditions are realized for the *FO* ray, the scheme with two collimators provides exactly the same transmission of all the rays reflected from the crystal, as well as the scheme with one primary collimator. Therefore, peak intensities of lines in both schemes should be the same. A slight decrease is due to the transmission coefficient of the second collimator.

2.4 The high-oriented pyrolytic graphite reflection coefficient in different radiations

High-oriented pyrolytic graphite (HOPG) shows a very high reflectivity in the range of short and medium wavelengths; however, it is characterized

by a high mosaicity [26]. In X-ray spectral analysis, pyro-graphite X-ray analyzers and monochromators with a crystallite misorientation of 0.4 to 0.6° have limited applications. For HOPG, this value can be reduced to 0.2° [26]. At this time, the reflectivity of graphite is about 10 times higher than for LiF; for example, the integral intensity of S-K_α line of graphite is a factor 30 higher than for EDDT crystals.

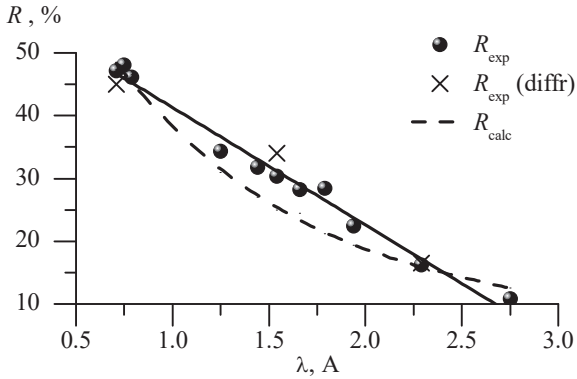

Figure 2.3: The relative integral reflectivity of pyro-graphite (002) reflections (R,%), depending on the wavelength of the probing fluorescent radiation: R_{calc},%, results of the theoretical calculation; R_{exp},%, experimental measurements of fluorescence radiation intensities for single-component targets; and R_{exp},% (diffr.), results of measurements in the monochromatic radiation of the X-ray tube in the diffractometer.

Since the use of pyro-graphite as a monochromator for XRF is promising, we studied its reflectivity in the following wavelength range: λ = 0.47÷2.75 Å. The integral intensity was measured using the spectrometer scanning mode with the K_α fluorescence line of single-component samples as the probing radiation. Both the K_β radiation and the scattered continuous

spectrum were cut off by the thresholds of the discriminator of the flow-proportional counter with an energy resolution of 16.5 % at the Cu-K_α line. Such tuning makes it possible to reduce the contribution of the K_β line into the measured intensity of the probing fluorescence radiation by at least three or four times. Independent measurements were carried out with the X-ray diffractometer in monochromatic radiations Ag-K_α ($\lambda = 0.56$ Å), Cu-K_α ($\lambda = 1.54$ Å) and Cr-K_α ($\lambda = 2.29$ Å). The dependence of the integrated reflection coefficient on the wavelength was calculated from the following formula:

$$R_{\text{calc}} \sim 7{,}92 \cdot \frac{\left(1+\cos^2 2\theta\right)}{\sin 2\theta} \cdot \frac{\lambda^3 \left(\text{Å}^{\circ}\right)}{\mu\left(\text{sm}^2/g\right)} \cdot 10^{-2},$$

It was also represented in relative units for qualitative comparison with the experimental data (Fig. 2.3). As the probing radiation wavelength increases, the integral reflection coefficient decreases from 45 to 10 %, which is important to take into account when tuning spectrometers with graphite crystal-analyzers because, with their help, it is possible to determine the detection limits and the sensitivity of the analysis of impurities in the range $Z = 22 \div 92$.

2.5 Monochromators based on fullerite C_{60} epitaxial films

In Section 2.2, it was theoretically shown that fullerene C_{60} is one of the promising monochromators for the wavelength range, $\lambda = 4 \div 12$ Å. In order to verify this fact, an original technology for the deposition of fullerite high-perfect epitaxial layers in a quasi-closed volume was developed [28]. Fullerite layers up to 30 μm thick were grown on the mica substrates;

these showed a rocking curve width of ω = 0.2°: i.e., they were more perfect than the pyro-graphite monochromators.

Electron-microscopic observations showed that in the beginning stages of the growth, the fullerite layers on the mica substrates had a hexagonal close-packed lattice up to a thickness of about 0.2 μm (Fig. 2.4).

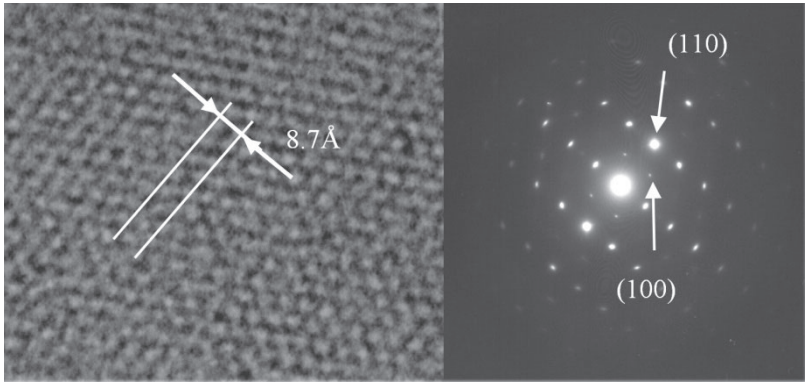

Figure 2.4: An electron-microscopic image and the diffraction pattern for a fullerite single-crystalline film, which was grown on synthetic mica (fluoroflogopite).

In the images of the direct resolution of the crystal lattice, fullerene molecules ordered in an hcp lattice are clearly visible. The distance between rows of molecules is 8.7 Å. No extraneous phases were detected. X-ray diffraction studies showed that as the layer thickness increases, an fcc lattice of fullerene molecules is formed, and the high oriented texture with an axis [111] perpendicular to the substrate surface appears. With a fullerite film thickness of more than 5 ÷ 10 μm, a texture with a misorientation

angle ω < 0.35° is formed, which allows the possibility of applying these films as monochromators for X-ray radiation [28, 30].

C_{60} fullerene is a new carbon material with a complex crystalline lattice [29, 31]. Therefore, fullerene epitaxial layers, called fullerites, require a structure attestation as well as calculations and experimental measurements of their spectral characteristics.

2.5.1 Calculations for the structural factor in the rotation model

The reflection integral intensity in the kinematic theory is determined by the square of the structural factor. For crystals with complex molecules, such as fullerene, the structural factor is determined by the form-factor F_m and can be calculated in the framework of the rotation model [6]. According to this model, each molecule can be assigned the following effective scattering function:

$$f_{\text{mol}} = \left(f_o + \sum_S f_s \cdot \frac{\sin \varphi_S}{\varphi_S} \right), \tag{2.10}$$

where $\varphi_S = 2\pi D \sin(\theta)/\lambda$; f_0 and f_S are, respectively, atomic factors of the central atom of the molecule and the atom located on the sphere of diameter D.

In the fullerene molecule, the central atom is absent ($f_0 = 0$), and the centers of 60 carbon atoms are statistically distributed over the surface of the sphere:

$$F_m = 60 f_C \frac{\sin(\pi S D)}{\pi S D} \tag{2.11}$$

where f_C is the atomic factor of carbon; $S = 2\sin(\theta)/\lambda$; and D is the diameter of the fullerene molecular sphere.

For Bragg reflections (hkl), $S = 1/d_{hkl}$ ($1/d_{hkl}$ is the modulus of the reciprocal lattice vector) and therefore, $\sin(\pi S D) = \sin(\pi D/d_{hkl})$.

Table 2.3: Reflection coefficients for monochromators in Fe-K$_\alpha$ radiation, which were calculated using kinematic theory, R_{kin}, and an experimental method, R_{exp},. The double-crystal spectrometer (n, -n) scheme.

Monochromator/ reflectivity	Graphite (002)	LiF (002)	Fullerite (111)	RbAP
$R_{kin} \cdot 10^4$, rad	43.6	7.20	3.45	0.6
$R_{exp} \cdot 10^4$, rad	25.9	5.3	2.4	0.5

By measuring d_{hkl} from the position of the Bragg reflections, one can determine the diameter of the fullerene molecule D and its variations under the influence of various factors using the dependence of the form-factor on the order of reflection. Fullerite C_{60} has the fcc lattice with a period H = 14.16 Å. The lattice contains molecules consisting of sixty carbon atoms in its sites. Epitaxial films of the new material (fullerite C_{60}) with (111) planes parallel to the substrate surface have an interplanar distance of $d_{(111)}$ = 8.175 Å and are fully fit for use as monochromators in the wavelength range of 4÷13 Å. However, there is no data on their reflection coefficients in the literature. Taking into account d_{111} = 8.175 Å and f_C = 5.625, we have $F^2(111) = 16 \cdot f_C{}^2 = 36284$ for fullerite.

Despite a significant decrease in the structural factor due to the molecular form-factor, fullerite occupies a worthy place among the best monochromators. In Table 2.3, the comparative characteristics of fullerite and known monochromators are shown. For Fe-K_α radiation, fullerite is considerably inferior in terms of its reflectivity with regard to pyrolytic graphite and lithium fluoride, which are used in the range of 0.4÷4 Å. However, for monochromators in the range of 4÷12 Å, the fullerite significantly exceeds the best of the currently used RbAP. It is important to note that by placing one heavy atom at the center of the molecule—for example, bismuth—would result (according to Eq. [2.10] at $f_0 = 79$) in 7.1-fold increase in the intensity of the (111) reflection. This conclusion stimulates the technological development of endo-fullerenes to create new monochromators.

2.5.2 Ratio of reflection orders and determination of C_{60} molecule size

Epitaxial layers of fullerite C_{60} with an orientation parallel to the mica substrate surface were grown using a modified method of quasi-closed volume [23, 30]. X-ray studies ware carried out with a diffractometer DRON-3M in Cu-K_α radiation monochromatized in the diffracted beam via graphite (002) reflection. Integral intensities of fullerite (*hhh*) reflections were measured in $\theta - 2\theta$ scanning mode but not in ω-mode, because the half-width of the rocking curve for the films is much less than the half-width of the monochromator directional pattern (about 0.6°).

Integral reflection coefficient was calculated by the formula:

$$\rho_{hkl} = \frac{S_{hkl}}{I_0}, \tag{2.12}$$

where S_{hkl} is area under the diffraction curve, counts·rad/s, and I_0 is the intensity of the primary beam (counts/s) when it falls completely in the counter.

The molecular form-factor F_m is determined from the structure factor for an fcc lattice:

$$\left|F_{hhh}\right|^2 = 16F_m^2 =$$

$$= \frac{2\ \mu\ \rho}{N^2}\frac{1}{\lambda^3}\frac{10^{26}}{7{,}9}\left(\frac{2\sin 2\theta}{1+\cos^2 2\theta}\right)\frac{\rho_{hhh}}{1-\exp\left(-\ \mu\ \rho\ \cos ec\,\theta\ t\right)}, \qquad (2.13)$$

where N is the number of unit cells per a volume unit; μ is the mass absorption factor; t is the film thickness; and ρ is the film density determined by the absorption of the K-K_α X-ray fluorescence line of potassium contained in the mica substrate.

Since the fullerite films on mica are strongly textured, and the texture axis <111> is perpendicular to the substrate surface, only the diffraction peaks of the (*hhh*) type are detected in the spectrum with θ–2θ scanning. The peak reflection coefficient for (111) planes can go up to 12 %. A characteristic width of the rocking curve for (*hhh*) reflections from the fullerite film is from 0.2 to 0.5°, while it is from 0.07 to 0.15° for the mica substrate. The fullerite lattice parameter determined by the positions of (666) and (777) maxima (Fig. 2.5), which varies in limits from 14.160 to 14.164 Å.

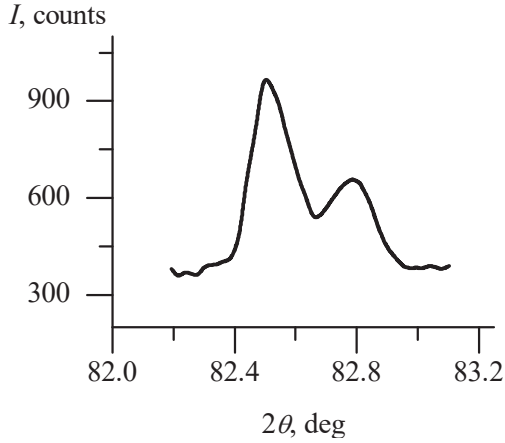

Figure 2.5: A 7th order (*hhh*) diffraction peak from the fullerite film. The pulse accumulation time per a point is 20 s.

The experimentally measured integral intensity of (*hhh*) reflections from the fullerite films is much less than that calculated for the structure of a bulk fullerene within the framework of kinematic theory. So, the theoretical value ρ_{hkl} for the (111) reflection is $530 \cdot 10^{-6}$ rad for the bulk state, whereas the maximum measured value for the film of 50 μm thickness is $146 \cdot 10^{-6}$ rad (Table 2.4).

When introducing a correction for the film thickness, this value should be $258 \cdot 10^{-6}$ rad for the bulk state: i.e., almost a half of the theoretical value. This decrease should be manifested to the greatest extent for first-order reflections due to extinction. For all other orders, both ρ_{hkl} and, consequently, F_{hkl} values obtained from the experimental data should also be lower than these calculated using kinematic theory because structure defects affect the intensity. This condition allows the possibility of introducing a constraint on the molecule diameter, *D*. The literature indicates *D*

values from 7.04 Å [31] to 7.12 Å [31, 32]. The above condition is valid only for $D \geq 7.09$ Å (Fig. 2.6, curves *2* and *3*), while at smaller D values the experimental curve crosses the theoretical curve near 6th and 7th orders of reflection (Fig. 2.6, curves *1* and *3*).

Table 2.4: Integral reflection coefficient ρ_{hhh} for (hhh) reflections from a fullerite film

(*hhh*)	Freshly-deposited film $\rho_{hhh} \cdot 10^6$, rad,	1st annealing $\rho_{hhh} \cdot 10^6$, rad	2nd annealing $\rho_{hhh} \cdot 10^6$, rad	3rd annealing $\rho_{hhh} \cdot 10^6$, rad
(111)	146.41	38.53	76.80	87.64
(222)	43.35	7.67	4.07	23.84
(333)	10.16	2.97	4.65	8.29
(444)	0.953	0.275	0.47	0.746
(555)	0.173	0.0557	0.083	0.128
(666)	0.041	0.0148	0.021	0.0308
(777)	$3.02 \cdot 10^{-3}$	$1.49 \cdot 10^{-3}$	$0.92 \cdot 10^{-3}$	$1.54 \cdot 10^{-3}$

In order to determine the D value more precisely, it is necessary to choose the ratio of $(F_{hhh})^2$ values for two reflection orders with arguments close to one of the zero points of the $[\sin(\pi S D)] / (\pi S D)$ function. According to Eq. (2.11), at $D = 7.10 \div 7.14$ Å, the zero value is reached near the 8th order (*hhh*) which cannot be observed in the experiment. Therefore, it is the ratio of $(F_{hhh})^2$ values for 6th and 8th orders of reflection that provides the highest sensitivity. The ratios $(F_{666})^2 / (F_{777})^2$ determined from the experimental

ρ_{hkl} values are in the range of 6.89 to 9.96 for the fullerene films under study; this corresponds to the molecule diameter of 7.140 to 7.104 Å.

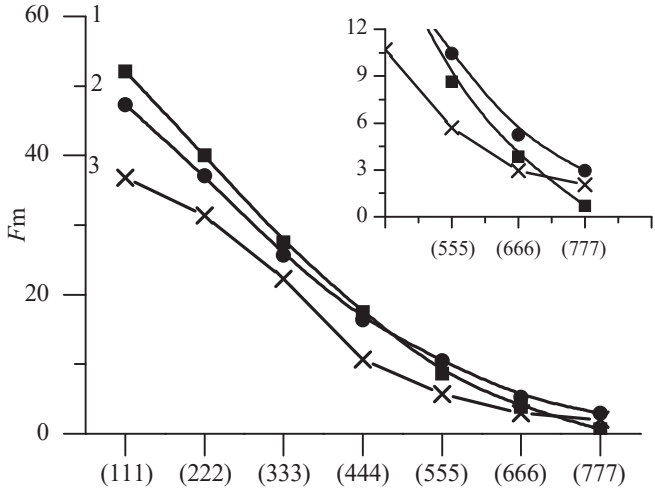

Figure 2.6: Values of molecular form-factor F_m for a fullerene C_{60} molecule versus reflection order (*hhh*) calculated by Eq. (2.13) for D = 7.04 Å (curve 1) and 7.14 Å (curve 2), and experimental values of diffraction integrated intensities for a fullerene film of 50 μm (curve 3).

Figure 2.7 shows the dependence of the peak reflectivity R_{111} on the ratio of integrated intensities for 6th and 7th reflection orders. An increase of R_{111} from 2.65 % to 12 % is accompanied by increasing the $\rho_{(666)} / \rho_{(777)}$ ratio from 9.74 to 13.61. This variation corresponds to decreasing the molecular diameter by 0.035 Å as calculated from the ratio of $(F_{666})^2 / (F_{777})^2$.

The pulse vacuum annealing of the fullerene film with the smallest diameter D = 7.104 Å leads to decreasing the ratio of $(F_{666})^2 / (F_{777})^2$ from 9.96 to

7.16 (the first annealing), which can be interpreted as an increase in the molecular diameter up to 7.136 Å.

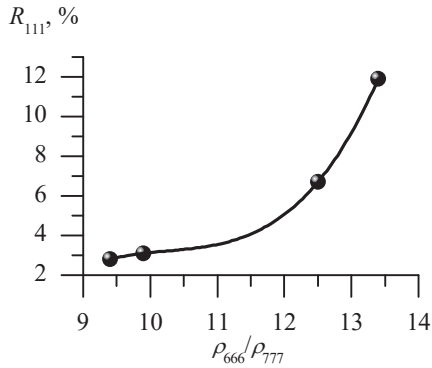

Figure 2.7: Peak reflection coefficient R_{111} depending on the ratio of integrated intensities for 6th and 7th reflection orders

The successive use of the long low-temperature and high-temperature annealing (2nd and 3rd annealing) leads to an increase in the ratio of $(F_{666})^2$ / $(F_{777})^2$ from 14.6 to 16.8, which corresponds to a reduction in the molecular diameter from 7.09 up to 7.085 Å. Without discussing the reasons for such D reduction, we point out the possibility of detecting small changes (0.001 Å) in the fullerene molecular diameter under the influence of external factors by determining the argument $\pi S D = \pi n D / d_{111}$ and independently measuring the interplanar distances.

In conclusion, the molecular rotation model adequately describes the experimental dependence of the form factor on the order of reflection up to the 7th order. A procedure has been developed for the exact determination of the fullerene molecular diameter from the ratio of the integrated intensities of reflections of the 6th and 7th orders. Within the framework of the

rotation model, it was found that the diameter of the fullerene molecule changes upon vacuum annealing of the film.

2.5.3 Dependence of the fullerite reflection coefficient on the wavelength in the range λ from 1.54 Å to 8.34 Å

Epitaxial C_{60} fullerite films with (111) orientation show a half-width for the rocking curves $\omega = 0.35 \div 0.22°$ (Fig. 2.8) when at least 10 cm^2 of the surface area is illuminated [23]. Such a half-width, apparently, is a record for monochromators based on carbon [26] and raises the hope of obtaining high-quality X-ray spectra for elements from the Periodic Table's third period.

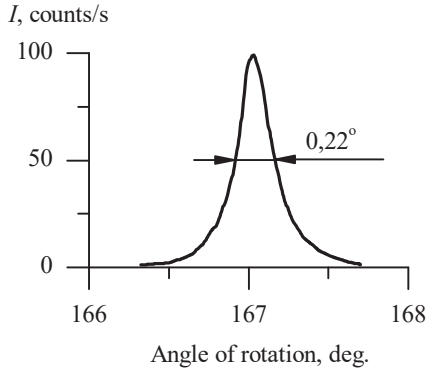

Figure 2.8: Experimental rocking curve for a fullerite C_{60} epitaxial film

Nevertheless, in the experiment, we failed to reach the theoretical peak reflection coefficient R_{peak} in the range of wavelengths $\lambda = 4.5 \div 7.5$ Å and to exceed the traditional PbAP (Fig. 2.9). The possible reason for the understatement of R_{peak} of the fullerite epitaxial layers is their structural features.

Let us consider this issue in more detail. Fullerene's high tendency to saturation from the oxygen and nitrogen in air is well known. Estimations show that understating the peak reflection coefficient may be due to a change in the structural factor change from the atoms' saturation of the fullerite crystal lattice.

The fcc lattice, which was formed by fullerite molecules, contains tetrahedral voids with a radius of r_{tet} = 1.125 Å and octahedral voids of r_{oct} = 2.06 Å. Since the radii of nitrogen and oxygen atoms are approximately the same (0.89 and 0.88 Å, respectively) an isolated atom most likely enters in a tetrahedral void, while a gas molecule may enter into an octahedral one. If gas atoms occupy all the tetrahedral voids in the fcc lattice, we will obtain a lattice with a K6 structural type (type CaF_2), where the structure factor F (111) is the same as for the fcc lattice. Oxygen molecules in the octahedral voids result in structural type K5, where the (111) reflection intensity is 2.2 times lower than the fcc lattice.

Thus, the experimentally observed double understatement of the peak intensity may be due to the presence of molecular oxygen in the octahedral voids. Only 4.3% of oxygen mass in the epitaxial layer is sufficient to create this effect. The oxygen in the fullerite lattice was measured by XRF using the O-Kα line fluorescence intensity. The fluorescence spectrum was registered using a scanning spectrometer with a Mo-B_4C short-period X-ray mirror. Figure 2.10 shows a fragment of the typical fluorescence spectrum for the fullerite epitaxial layer in the wavelength range λ = 18÷28 Å.

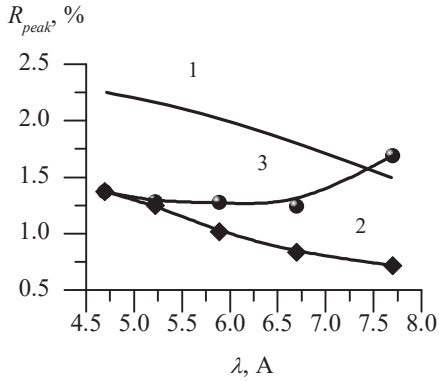

Figure 2.9: Dependence of the peak reflection coefficient on the wavelength: 1, theoretical (monochromator C_{60}); 2, experimental (C_{60}); and 3, experimental (RbAP).

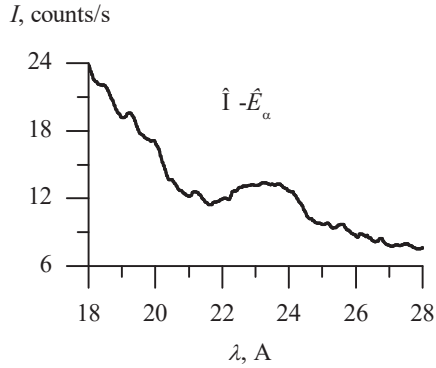

Figure 2.10: An O-Kα oxygen line observed in the X-ray fluorescence spectrum of a fullerite film. The determined mass concentration of oxygen in the film is 3.28 %.

The intensity of the detected oxygen peak O-$K\alpha$ corresponds to the total oxygen content of about 3.28 % mass in the fullerite.

This result indirectly confirms the hypothesis about the effect of molecular oxygen in the fullerite lattice on a two-fold drop of the peak reflectivity. In order to avoid the entry of oxygen atoms into the fullerite epitaxial layer after deposition, a gas-proof coating transparent to X-rays could be deposited. If successful, the best crystal analyzer for the range $\lambda = 4.5 \div 7.5$ Å will be obtained.

2.5.4 Characteristics of spectra obtained via fullerite crystal analyzers

As an example, we will now consider aluminum alloy spectra obtained with fullerite and RbAP crystal-analyzers in a wavelength range of 4 to 8.5 Å (Fig. 2.11). These spectra were recorded with similar geometry using vacuum WDXRF spectrometers. Let us compare the quality of the spectra obtained with RbAP and fullerite C_{60} crystal analyzers.

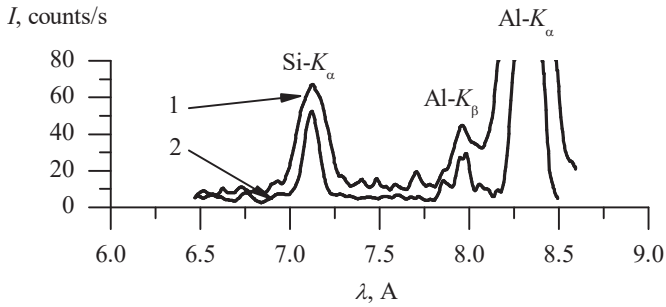

Figure 2.11: Comparison of aluminum alloy spectra obtained with an RbAP crystal (1) and a fullerite film (2).

The peak intensity values of the Si-K_{α}, Al-K,α and Al-$K\beta$ analytical lines are very close in the both spectra, but their half-widths in the fullerite spectrum are smaller by a factor 1.6. This means that the fullerite crystal-

analyzer provides a spectral resolution that is 1.6 times better than the RbAP at the same line intensity. In spectrum *2* and fullerite (Fig. 2.11, curve *2*) a weak Al-K_β line is clearly visible, while in spectrum *1* it is poorly detected due to the overlap of the strong Al-K_α line's "tail". The contrast of the Si-K_α and Al-K_α analytical lines in spectrum *2* is greater than in spectrum *1*. Thus, for the elements from the third period, fullerite provides a higher quality of the spectra than RbAP, which was previously considered to be the best from the perspective of current crystal analyzers in this wavelength range.

2.6 Multilayer X-ray mirrors

2.6.1 Structural characteristics

Multilayer X-ray mirrors (MXM) are multilayer film compositions of periodically alternating layers made from usually two materials. A reflection from MXM is formed as a result of interference by the rays reflected from the interlayer interfaces. The angular position of the reflection maximum is determined by the Bragg equation with an allowance made for refraction:

$$2H \sin\Theta_n \sqrt{1-\frac{2\delta}{\sin^2\Theta_n}} = n\lambda \qquad (2.14)$$

where H is the period, Θ is the grazing angle, n is the order of the reflection, λ is the wavelength of radiation, and δ is the real part of the refraction index.

MXM are highly reflective optical elements for X-rays with wavelengths λ in a range from 10 to 500 Å. In view of the complex wavelength dependence of the materials' optical constants, this rather narrow range for the electromagnetic spectrum is divided into several ranges where the maximum possible reflection coefficient R can be achieved., Different compositions of materials are used in each of these ranges. E. Spiller formulated the rule of choice for the materials [33]. According to this rule, the material with the lowest absorption in the considered part of the spectrum (a low absorption layer) is selected first. The second is the material that provides the maximum reflection at the interface with the first material (a high absorption layer). Also important is the manufacturability of materials: i.e., it is necessary to make sure that the selected materials can be grown in the form of thin, continuous, and smooth layers. The thickness of an individual layer is varied in the range of 10 to 250 Å, which is determined by the working wavelength and the geometry of the experimental arrangement.

The ratio of the layer thicknesses, which ensures the maximum reflection of the MXM, is given by

$$\gamma = t_a / H \approx 0.4, \tag{2.15}$$

where t_a is the thickness of the high absorption layer and H is the period. The number of periods in the MXM is determined by the absorption of the multi-layered composition. Since all the materials in the considered range have a high absorption, the total thickness of the multilayer coating is $t_\Sigma \approx$ 200 ÷ 400 Å. The number of periods is from 5 to 10 for the long-

wavelength range of the spectrum and from 2 to 300 for the short-wavelength range.

The ability to purposefully optimize the material and design of the MXM is an important advantage over molecular crystals that have a fixed period and, in terms of optics, a non-optimal composition. Another important advantage of MXM is the ability to produce them on curved substrates, as well as within a specified variation over the substrate's area. The preliminary quality control of the manufactured mirror is based on the results of the small-angle X-ray diffraction according to the Θ – 2Θ scheme. This method is based on a fundamental physical effect: the total external reflection (TER) of X-ray radiation at the interface between two media. Therefore, a critical condition is the absence of surface roughness. The beams reflected from the upper and lower boundaries of the film interfere with this, resulting in a series of oscillations whose angular positions can be used to estimate the film's thickness:

$$t = \frac{\lambda}{2}\left[\sqrt{\theta_{m+1}^2 - \theta_k^2} - \sqrt{\theta_m^2 - \theta_k^2}\right], \tag{2.16}$$

$$\theta_k = \left(\frac{\theta_m^2}{m^2} - \frac{\theta_{m+1}^2}{(m+1)^2}\right) \Big/ \left(\frac{1}{m^2} - \frac{1}{(m+1)^2}\right), \tag{2.17}$$

where $\theta_{m,\ (m+1)}$ are angular positions of neighboring maxima of m and (m+1) orders; and θ_k is the critical angle of TER.

The intensity of these oscillations for the "film-substrate" system is described by the Fresnel formula, in which the reflection amplitudes from the

upper and lower boundaries of the film are considered. The densities of the film and substrate materials determine the magnitudes of these amplitudes. Therefore, by performing a full-profile analysis of the X-ray reflectivity angular dependence, it is possible to independently determine the film's thickness and density.

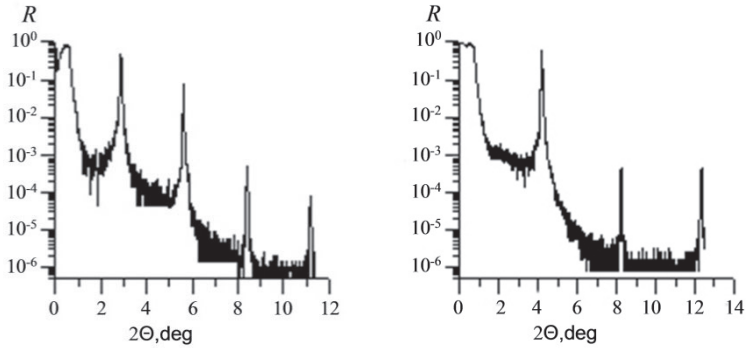

a *b*

Figure 2.12: X-ray diffraction from MXM W/B_4C in Cu-K_α radiation: (*a*) H = 31.7 Å and (*b*) H = 21.6 Å.

The diffraction oscillations have been observed experimentally starting with a film thickness of 12 Å [34]. In fact, good accuracy is ensured with a film thickness exceeding 50 Å, when more than three orders of oscillations are confidently observed. As the thickness of the film decreases, the oscillations are blurred and the measurement accuracy drops. The diffraction pattern of MXM W/B_4C with period $H \approx 21.6$ Å is shown in Figure 2.12, *a*. The mirror period is calculated from the angular positions of the diffraction maxima; the thickness and density of the layers and the level of the interlayer roughness are estimated from the results of the diffraction curve simulation. By varying the ratio of the thicknesses for the low- and high-

absorption layers, one can change the intensity ratios of the reflection orders in the diffraction curve. In particular, this dependence makes it possible, if necessary, to suppress the second order of diffraction. For this, the thicknesses of the high- and low-absorption layers must be the same. Figure 2.12, *b* shows the small-angle diffraction spectrum from MXM W/B_4C with a period $H \approx 21.6$ Å where alternating W and B_4C layers have a thickness of $t \approx 10$ Å.

In the X-ray spectral analysis, the wavelength range of 5 to 100 Å is the most interesting. This is where the *K*-series of light chemical elements are located (Table 2.5). A large set of pairs of materials is used to manufacture the mirrors operating in this part of the spectrum. The selection of materials for analyzing the lightest elements (from beryllium to nitrogen) is carried out according to Spiller's rule. For chemical elements with shorter wavelengths for their characteristic radiation (from oxygen to silicon), the main requirement for choosing MXM materials is their manufacturability, and then their optical contrast. A combination of light and heavy refractory materials (tungsten and boron carbide; tungsten and silicon) meets both these requirements. Using a single mirror to measure several elements allows us to simplify the design of the device and increase the speed of information collection.

However, W/Si and W/B_4C MXMs are not suitable for the analysis of phosphorus because tungsten and silicon have absorption jumps at wavelengths $\lambda_W = 6.85$ Å and $\lambda_{Si} = 6.74$ Å, respectively. Thus, it is advisable to turn to Mo / B_4C mirrors (Table 2.5).

Table 2.5: MXM for the analysis of light elements in a wavelength range of 6 to 120 Å

Element	Z	*K*-series wavelength λ, Å	MXM	Period, *H,* Å
Be	4	114.0	Mo/Be, Ti/Be	60÷100
B	5	67.6	Mo/B_4C, Sb/B_4C	35÷60
C	6	44.7	Co/C, Ni/C, Cr/C	23÷50
N	7	31.6	Cr/Sc	16÷40
O	8	23.6	W/Si, W/B_4C	20÷50
F	9	18.3	W/Si, W/B_4C	20÷40
Na	11	11.9	W/Si, W/B_4C	20÷40
Mg	12	9.9	W/Si, W/B_4C	20÷30
Al	13	8.3	W/Si, W/B_4C	20÷30
Si	14	7.1	W/Si, W/B_4C	20÷30
P	15	6.2	Mo/B_4C	20÷30

Figure 2.13 shows the electron microscopic images of the cross-sections of Co/C and W/B_4C multilayer mirrors. The first mirror has a period of H = 70 Å and is intended for carbon analysis. As stated, this mirror represents strictly alternating layers of amorphous carbon and amorphous cobalt with sufficiently smooth interfaces. The deposition of layers causes cobalt amorphization [35]. Since such an interaction is practically absent between carbon and silicon, the first carbon layer deposited on the single-crystalline silicon substrate has a greater thickness than the layers of carbon between the cobalt. To varying degrees, the interlayer interaction in the manufacturing process is characteristic of various combinations of

materials. This feature should be taken into account when manufacturing MXM.

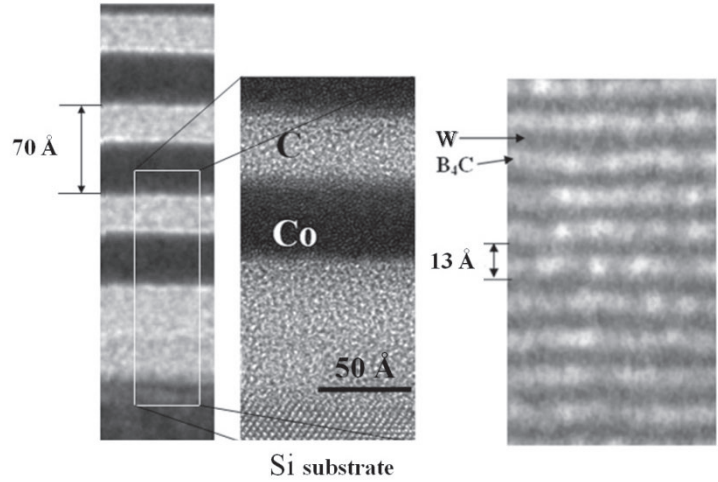

Figure 2.13: Cross-section electron microscopic images of Co/C (left) and W/B_4C (right) MXM.

W/B_4C MXM also exhibits an interlayer interaction in the manufacturing process, although it is less intense than in the Co/C system. As a result, this short period mirrors the absorbing layer, which is not pure tungsten, but is instead a mixture of tungsten with carbon [35]. This fact should be taken into account when evaluating the maximum achievable reflection coefficient R. The W/B_4C with period H = 13 Å is close to the minimum realizable value for X-ray mirrors, since the reflection coefficient decreases with the decreasing period of the MXM (Fig. 2.14).

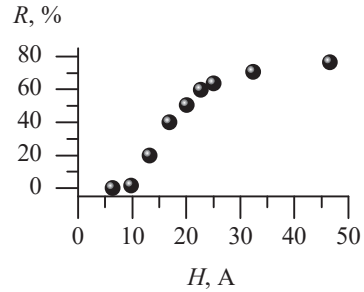

Figure 2.14: Experimental reflection coefficients R versus period H from a W/B_4C mirror measured using Cu-K_α radiation.

Qualitatively, this dependence is typical for all mirrors and is due to the increasing influence of the interlayer root-mean-square roughness on the reflection coefficient as well as the non-uniformity of the super thin layers.

2.6.2 Short-period mirrors and the dependence of reflection coefficient on the operating wavelength range period

Short-period mirrors are intended for a spectral range of 5 to 24 Å (Table 2.5), where the K-series lines from the third line elements are located [34]. To ensure the reflection angles $\theta > 5°$ are acceptable for X-ray spectral measurements, it is necessary to reduce the mirror period to $H = 10 \div 30$ Å. With such small periods, the roughness of the interlayer boundaries significantly affects the reflection coefficient. In this section, we will present the measurements of the reflection coefficient in the operating wavelength range and the characteristic spectra obtained with short-period mirrors. Small-angle X-ray diffraction patterns of MXM with periods H of 13.2 to 33.7 Å show three to five peaks corresponding to Bragg reflections from the periodic structure (Fig. 2.15).

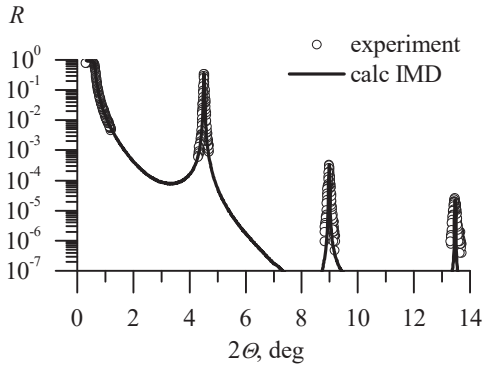

Figure 2.15: Small-angle X-ray diffraction spectrum from a Mo-B_4C MXM with a period of H = 19.72 Å.

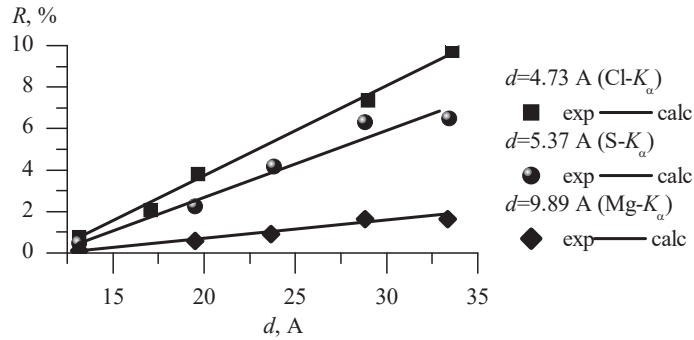

Figure 2.16: Dependences of the reflection coefficient on the period of Mo-B_4C MXMs for radiations with different wavelengths.

The half-width of these peaks is practically independent on the order of reflection, which indicates the constancy of the MXM period over the irradiated volume. When measuring using soft radiation, a sharp fall in the reflection coefficient is observed when decreasing the mirror period (Fig. 2.16). The greater the fall, then the longer the wavelength will be from the

used radiation. So, for Cl-K_α (λ = 4.73 Å), shortening the period from 33.7 to 13.2 Å results in a reflection coefficient decrease by a factor of 7, and for Na-K_α by a factor of 15. Simulation of the small-angle diffraction spectra with IMD software showed that the main structural reason for reducing the reflection coefficient is the roughness of the interlayer boundaries. Fitting the theoretical and experimental diffraction patterns allowed us to establish that the root-mean-square roughness ξ of the interlayer boundaries in all multilayer mirrors is approximately the same (3 to 2.9 Å).

Parameters of MXM (layer thickness; density and roughness of the interlayer boundaries) obtained by fitting the theoretical and experimental small-angle diffraction patterns in Cu-K_α radiation were used to calculate the diffraction spectra in soft X-rays. A good coincidence of the experimental and calculated plots (Fig. 2.16) confirms the correctness of the chosen model, and the dependence of the reflectivity R on the mirror period for λ from 4.7 to 11.9 Å corresponds to $R \sim \exp\left(-\pi\xi^2/d^2\right)$. The short-period Mo-$B_4C$ mirrors with H >17 Å demonstrated a significant gain in the intensity of the spectral lines in comparison with RbAP (Fig. 2.17). The spectra are of an acceptable quality with a clear separation of the silicon, aluminum, and magnesium lines. For practical applications in scanning devices, the optimal H range is from 24 to 29 Å but, in this case, we have to reduce the beam angular divergence of the X-ray optical scheme to improve the spectral resolution. Figure 2.17 demonstrates that using a mirror with H = 29.2 Å and a proper collimation, it is possible to obtain spectra of higher quality: the line intensity is higher and the spectral resolution is better than for H = 17.1 Å.

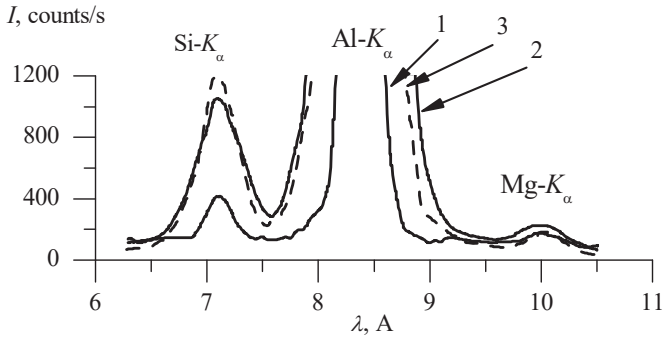

Figure 2.17: Fragments of the aluminum alloy X-ray spectra obtained with different crystal-analyzers: 1, RbAP; 2, Mo-B_4C MXM, H = 17.1 Å; and 3, Mo-B_4C MXM, H = 29.2 Å.

Thus, MXMs allow us to obtain spectra with higher qualities than with RbAP crystals in the λ range of 4.5 to 12 Å; therefore, they are promising for use in WDXRFs. Compared with fullerite, they provide a fourfold gain in intensity, but they suffer double the loss in spectral resolution.

2.6.3 Long-period X-ray mirrors for measuring light elements using fluorescence lines

The fluorescence lines of these elements are in the wavelength range of 18 to 67 Å, where mirrors based on silicon, scandium, and carbon layers in combination with the metal layers are optimal. In order to comply with the Bragg reflection conditions, the period H of the mirrors should be in the range of 40 to 70 Å, so that the effect of the layer roughness on the reflection coefficient is less critical than for the short-period form [35]. However, the problem of measuring the intensity of long-wave radiation lines consists in a strong absorption by the window material of a flow-proportional detector. Even the best Proline 10 windows with a thickness

of 0.65 μm provide about 10% transmission efficiency for the N-K_α line, and 60% for the C-K_α line. In addition, the extremely low fluorescence yield and the strong absorption of these emissions from the sample matrix sharply reduce the signal intensity and hinder the quantitative analysis. Examples of the measurement of light elements are given in Chapter 5. In this section, we will consider the characteristics of the spectra obtained with Co-C mirrors using the example of determining carbon content in steel.

The determination of carbon content using the XRF method is very difficult because of the low fluorescence yield $\omega_q = 0.0026$, and also due to the strong absorption of its fluorescence radiation by the sample material. Nevertheless, there are analytical problems requiring the non-destructive control of carbon content, which can only be provided by XRF. Such problems include studying the properties of thin films, adsorbed layers, and even bulk materials; for example, analyzing carbon content together with other chemical elements that are constituents of steel or cast iron. Finding a solution to these problems is possible with effective X-ray mirrors. In the wavelength range of interest, 44 Å < λ < 67 Å, carbon has the lowest absorption in comparison with the other materials. So, mirrors based on it should, therefore, be the most effective. The requirements are not so critical for a heavy mirror component. In terms of reflectivity, a series of transition metals (Co, Fe, Ni, Cr, etc.) are optimum matches for carbon. For the given case, the theoretical reflectivity of the Co-C mirrors is maximal, which causes an increased interest in this system. The possibility of determining carbon in iron-carbon alloys can be evaluated by analyzing the fluorescence spectra of cast iron and steel specimens. Figure 2.18 shows fragments of cast iron and steel spectra obtained using a Co-C multilayer

mirror with a period H = 44 Å. The spectra show a well-defined C-K_α carbon peak.

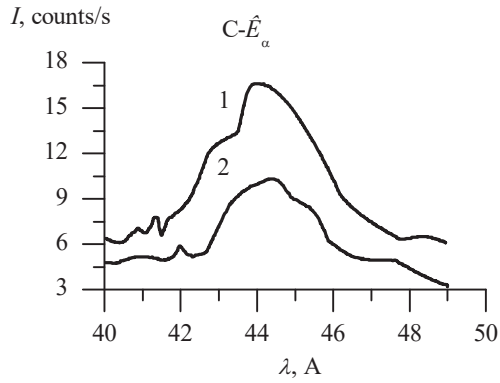

Figure 2.18: The difference in the intensity of the C-K_α line in the spectra of cast iron (4.02 % mass of carbon, curve *1*) and carbon steel (1.6 % mass of carbon, curve *2*)

The experimental half-width of the carbon line, $\Delta\lambda$ = 2.79 Å, corresponds to the calculated value $\Delta\lambda$ = 2.57 Å. The application of a modernized X-ray optical scheme with two Soller collimators has allowed us to achieve a good contrast for the carbon line in cast iron. Figure 2.19 presents the calibration plot obtained after optimizing the X-ray optical scheme for the C-K_α line.

The results of the measurements are comparable with the data obtained via the new powerful Rigaku spectrometer, "Simultix 12", using the ratio of the background signal to the signal gain per 1% change in concentration. This value is 2.5 according to Rigaku data. Consequently, the detection limit is approximately the same at C_{min} = 0.2 % mass.

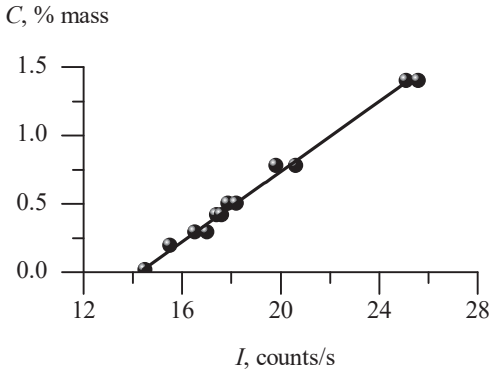

Figure 2.19: Calibration function (for carbon in steels) obtained using a Co-C mirror (period H = 44 Å) with a Moxtek ProLine 10 window in an X-ray optical scheme optimized for C-Kα line contrast.

The results from measuring carbon concentrations in steels using the intensity of the fluorescent C-K_α line did not meet the requirements of the State Standard detection limit. To improve the obtained characteristics, we optimized the Co-C mirrors using the reflection angle and applied a 0.65-micron window (Proline 10, Moxtek, USA) in the counter window.

This made it possible to increase the sensitivity to 6 counts/s per 1% mass with a background signal of 14 counts/s (Fig. 2.19), which corresponds to the detection limit C_{min} = 0.108% mass. This result allowed us to use the spectrometers to determine the carbon in cast iron and steel with a minimum detection limit for carbon at the level of 0.1%.

Conclusion to Chapter 2

The main advantage of crystal-diffraction spectrometers is their high spectral resolution, which is important for revealing weak signals in complex

X-ray spectra with a significant overlap of spectral lines. This advantage mainly determines the application area of the WDXRF spectrometers. The high spectral resolution is achieved due to the luminosity of the X-ray optical scheme, so the analysis sensitivity depends on the primary radiation source power and the parameters of the crystal analyzer: the reflection coefficient and structural perfection. Single crystals with a high reflection coefficient are often characterized by low structural perfection.

To use such materials as crystal-analyzers, a new X-ray optical scheme with two Soller collimators has been designed; its spectral resolution does not depend on the rocking curve width of the crystal-analyzer. The creation of new carbon based crystal-analyzers and multilayer X-ray mirrors, as well as the development of X-ray optical schemes and ultra-thin windows, expand the possibilities for the analysis of light elements in materials via the intensity of their fluorescence lines.

CHAPTER 3

ENERGY-DISPERSION X-RAY FLUORESCENCE ANALYSIS

3.1 Optimization of the primary beam formation unit

Due to the high luminosity of the EDXRF spectrometers, it is possible to optimize the parameters of the beam-forming unit to obtain the maximum possible sensitivity of the analysis, taking into account the detector efficiency and its background characteristics.

In this section, we will separately consider the conditions for optimizing the parameters of the primary radiation filter and the secondary target, as well as their joint application in the formation unit.

3.1.1 Conditions for optimizing a primary radiation filter's parameters

The analytical capability of instruments in which the filtration of primary radiation is used to contrast the spectra is well illustrated by the experiment in the scheme [13, 36] (Fig. 3.1). A shooting-through type tube with a silver anode operating at a voltage U = 15 kV was used as the X-ray source. The detector registers the tube primary radiation passing through the aluminum filter, which hits the sample, as well as the emergent fluorescent and scattered radiation.

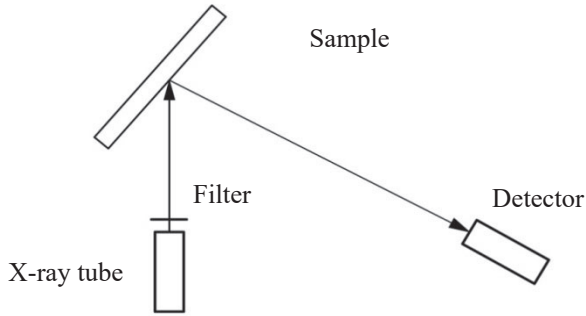

Figure 3.1: X-ray optical scheme with a filter in the primary beam

We determined the dependence of the detection limit C_{min} on the thickness of the primary radiation filter for various chemical elements [37]. We used state standard samples containing a 1% mass of silicon, phosphorus, sulfur, calcium, titanium, and cobalt in a light matrix (B_2O_3). Experiments show that yhe optimum filter thickness can be selected for heavier elements (calcium, titanium, and cobalt), while for lighter elements the minimum detection limit is achieved in the absence of a filter. That is, for the analysis of some chemical elements, one can find the filter's optimum thickness, but for others this is not possible. The comparison of the experimental results (Table. 3.1) with the calculations carried out by the algorithm (Section 1.5) is shown in Figure 3.2. For silicon, phosphorus, and sulfur, the smallest C_{min} is achieved in the absence of a filter under the specified experimental conditions. For heavier elements, the optimum filter thickness depends on the atomic number: the larger the atomic number, the greater the optimum filter thickness.

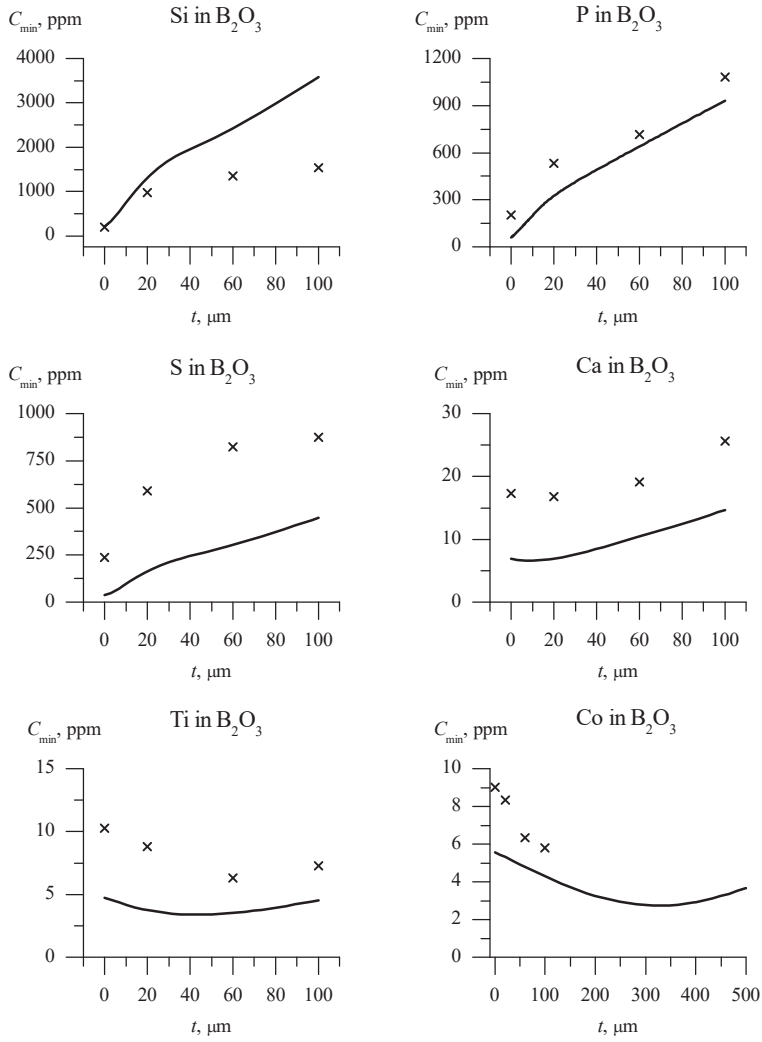

Figure 3.2: Experimental (×) and theoretical (–) dependences of the detection limit C_{min} on the filter thickness for different standards.

Table 3.1: Detection limit C_{min} (ppm) was calculated from experimental data for impurities at concentrations of 1 % mass in boric acid. The primary radiation filter material was aluminum.

Thickness Al, μm	Si	P	S	Ca	Ti	Co
0	202	202	238	17	10	9
20	970	531	589	17	9	8
60	1343	718	825	19	6	6
100	1541	1082	874	26	7	6

This means that the maximum of the continuous spectrum is quite far from the lines of the analyzed elements: the easier the element, the less the intensity of the lines excite it. Obviously, for light elements, the optimization problem is solved at lower supply voltages, when the bremsstrahlung spectrum is shifted to the long-wave region. Indeed, when the supply voltage drops to 8 kV, the optimal filter thickness for the analysis of sulfur is about 3 μm (calculated theoretically). In order to correctly determine the optimal filter thickness, it is necessary to solve this problem in a general form.

We consider the number of accumulated background counts as the sum of two components: a filtered background signal $B(\lambda)$, and a background signal A that does not depend on the filter parameters. Then, according to Eq. (1.1), the radiation passed through the filter can be written in the form:

$$I_f = B(\lambda)\exp(-\mu_f(\lambda)\,\rho\,t) + A \tag{3.1}$$

Taking into account the absorption of the primary radiation, the concentration sensitivity is written as

$$\frac{\partial I}{\partial C} = \int_{\lambda_{ed}}^{\lambda_{2q}} \frac{\Phi_{01}(\lambda)\,\mu_i(\lambda)\exp(-\mu_f(\lambda)\,x)}{\left(\dfrac{\mu_1(\lambda)}{\sin\varphi} + \dfrac{\mu_i}{\sin\psi}\right)}\,d\lambda = \int_{\lambda_{ed}}^{\lambda_{2q}} \Phi(\lambda)\exp(-\mu_f(\lambda)\,x)\,d\lambda \tag{3.2}$$

where $\Phi_{01}(\lambda)$ is the spectrum incident on the filter; $\mu_i(\lambda)$ is the coefficient of the spectrum attenuation by the analyzed element *i*; $\mu_1(\lambda)$ is the coefficient of the spectrum attenuation by the sample matrix; μ_i is the coefficient of the *i* element analytical line attenuation by the sample matrix; and $x = \rho \cdot t$.

To determine the filter thickness at which the detection limit is minimal, we substitute the obtained expressions (3.1) and (3.2) into (1.7), then differentiate with respect to *x* and equate to zero.

Change of variables:

$$U = \sqrt{B(\lambda)\exp(-\mu_f(\lambda)x) + A}, \quad U' = -\frac{1}{2}\frac{B(\lambda)\mu_f(\lambda)\exp(-\mu_f(\lambda)x)}{\sqrt{B(\lambda)\exp(-\mu_f(\lambda)x) + A}},$$

$$V = \int_{\lambda_{ed}}^{\lambda_{2q}} \Phi(\lambda)\exp(-\mu_f(\lambda)x)d\lambda, \; V' = \int_{\lambda_{ed}}^{\lambda_{2q}} (-\mu_f(\lambda))\Phi(\lambda)\exp(-\mu_f(\lambda)x)d\lambda,$$

$$\left(\frac{U}{V}\right)' = U' \times V - V' \times U = -\frac{1}{2}\frac{B(\lambda)\mu_f(\lambda)\exp(-\mu_f(\lambda)x)}{\sqrt{B(\lambda)\exp(-\mu_f(\lambda)x) + A}} \times$$

$$\times \int_{\lambda_{ed}}^{\lambda_{2q}} \Phi(\lambda)\exp(-\mu_f(\lambda)x)d\lambda -$$

$$-\int_{\lambda_{ed}}^{\lambda_{2q}}(-\mu_f(\lambda))\Phi(\lambda)\exp(-\mu_f(\lambda)x)d\lambda \sqrt{B(\lambda)\exp(-\mu_f(\lambda)x)+A}=0,$$

$$\left[B(\lambda)\mu_f(\lambda)\exp(-\mu_f(\lambda)x)\right]\int_{\lambda_{ed}}^{\lambda_{2q}}\Phi(\lambda)\exp(-\mu_f(\lambda)x)d\lambda+$$

$$+2\left[B(\lambda)\exp(-\mu_f(\lambda)x)+A\right]\int_{\lambda_{ed}}^{\lambda_{2q}}(-\mu_f(\lambda))\Phi(\lambda)\exp(-\mu_f(\lambda)x)d\lambda=0.$$

Using the mean value theorem for the integral [13] $\int\Pi\times\Theta=\langle\Pi\rangle\int\Theta$, we can write

$$B(\lambda)\mu_f(\lambda)\exp(-\mu_f(\lambda)x)+2\langle\mu_f(\lambda)\rangle\left[B(\lambda)\exp(-\mu_f(\lambda)x)+A\right]=0,$$

Now we will write the optimization criterion in the following form:

$$\mu_f(\lambda)=-2\langle\mu_f(\lambda)\rangle\left[1+\frac{A}{B(\lambda)}\exp(\mu_f(\lambda)x)\right], \tag{3.3}$$

$$\langle\mu_f(\lambda)\rangle=\frac{\int_{\lambda_{ed}}^{\lambda_{2q}}(-\mu_f(\lambda))\Phi(\lambda)\exp(-\mu_f(\lambda)x)d\lambda}{\int_{\lambda_{ed}}^{\lambda_{2q}}\Phi(\lambda)\exp(-\mu_f(\lambda)x)d\lambda}.$$

where

The formula (3.3) is obtained analytically without any assumptions. In general terms, it defines the conditions under which the filter thickness can be optimized by the $C_{\min}$ criterion.

Table 3.2: Calculations of μ_f using the criterion (3.3) for a zero filter thickness and supply voltage of 15.8 kV.

	Si, 1%	P, 1%	S, 1%	Ca, 1%	Ti, 1%	Co, 1%
$A/B(\lambda)$	1 698.5	27.80	2.01	1.07	0.19	0.02
$2(\mu_f(\lambda))$	-1334.4	-1286.6	-1209.4	-161.4	-124.6	-60.6
Right side of (3.3)	2 267 875	37 056	3 638	335	149	62
$\mu_f(\lambda)$	3 630	2 420	1 650	445	255	77
Optimiza-tion	no	no	no	yes	yes	yes

Table 3.3: Calculations of μ_f using the criterion (3.3) for zero filter thickness and a supply voltage of 8 keV.

	Si, 1%	P, 1%	S, 1%	Ca, 1%	Ti, 1%
$A/B(\lambda)$	101.23	1.76	0.14	0.10	0.02
$2(\mu_f(\lambda))$	-1485.3	-1432.7	-1348.1	-279.1	-208.7
Right side of (3.3)	151 841	3 956	1 530	306	213
$\mu_f(\lambda)$	3 630	2 420	1 650	445	255
Optimization	no	no	yes	yes	yes

Let us analyze the experimental results (Fig. 3.2) using the expression (3.3). Tables 3.2 and 3.3 show the left and right sides of the resulting equation for zero filter thickness and tube voltages 15.8 kV and 8 kV, respectively. The left side of the equation does not depend on the filter thickness. The right side increases when increasing x. Thus, at a supply voltage of 15.8 kV, the task of the filter thickness optimization is solved for calcium, titanium, and cobalt. This is also solved for sulfur, calcium, and titanium at a voltage of 8 kV; cobalt is not excited at this voltage.

The foregoing allows us to make three important statements that determine the scope of the primary spectrum's filtration. Firstly, in the absence of a detector background signal (constant signal), the filter thickness optimization using the $C_{\min}$ criterion does not have a solution in the classical XRF scheme. Secondly, the presence of the detector background signal provides the solution most pronounced medium and heavy element lines; this depends on the ratio of the detector background signal and the level of the continuous spectrum scattered by the sample. Thirdly, the minimum of the functional of the optimization problem is very weakly expressed and $C_{\min}$ decreases no more than twice the initial value.

3.1.2 The optimization of secondary target parameters for the detection limit

To excite a narrow range of chemical elements, the X-ray optical scheme works well with a secondary target. Now, we can somewhat change the classical scheme given in the previous subsection; however, the main nodes, the detector, and the tube remain the same. The geometry of the scheme is shown in Figure 3.3.

The secondary target is placed in the position of the sample (Fig. 3.1); the sample is displaced to the position of the detector, which in turn is placed above the sample, so that its axis becomes perpendicular to the surface of the sample. To protect the detector from the direct or the scattered primary radiation of the tube, a slit and a collimator are added to the scheme.

Let us theoretically compare the analytical possibilities of this scheme with the one considered in Section 3.1.1 [37]. The calculation of the detection limit of impurities in boric acid gave the following results: C_{min} (Si) = 43.2 ppm, C_{min} (P) = 14.2 ppm, C_{min} (S) = 8.5 ppm, and C_{min} (Ca) = 11 ppm. The initial conditions for the calculation are as follows: the target material was titanium; the voltage was 25 kV; and the current was 300 μA. Thus, the use of the secondary target makes it possible to reduce the detection limit of light impurities in boric acid by several times in comparison with the standard XRF scheme (Fig. 3.1). Let us analyze how the detection limit of the impurity changes when its absorption jump is distanced from the line of the secondary target. A convenient model is standard samples of aqueous solutions, because water provides a very high scattering level, and the obtained quantitative results can easily be recalculated for any light filler. In addition, it is possible to compare the results with those of Anisovich's classic experiment [15], in which, apparently, the limiting sensitivity of the crystal-diffraction spectrometer is reached. To excite the fluorescence of impurities of chemical elements from $Z = 22$ (Ti) to $Z = 30$ (Zn) at contents of 0.5 ppm and 5 ppm, we used a germanium secondary target. The lines of the germanium secondary target are close to the absorption jump of these elements, which ensures efficient fluorescence excitation. In the experimental spectrum (Fig. 3.4), analytical lines of "trace" impurities are clearly revealed even at concentrations of 0.5 ppm in aqueous solution. The contrast of the impurity lines with contents of 5 ppm lies

in the range of 1.7 to 3.6. In particular, for cobalt this value of 3.2 is close to the crystal-diffraction spectrometer's record value [15].

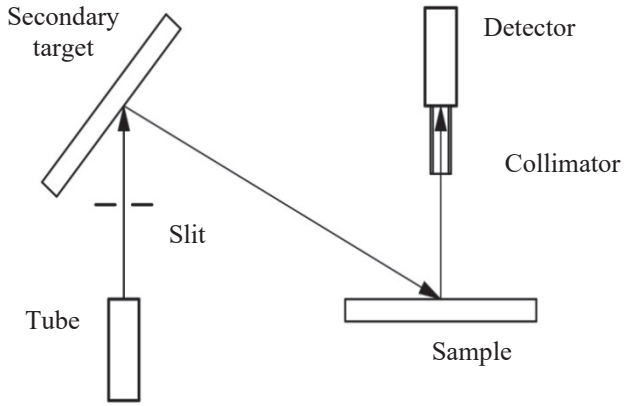

Figure 3.3: Geometry of the scheme with a secondary target

Let us consider the change in concentration sensitivity and background when the energy of the impurity absorption edge approaches the energy of the secondary target line (Table 3.4) [37]. As expected, the larger the difference in $E–E_{edi}$ between the energy of the secondary target line and the energy of the impurity absorption edge, the less the concentration sensitivity and scattering background. For the secondary target of polycrystalline molybdenum, the calculated and experimental data are completely consistent. This means that, in the experiment, the limiting characteristics of the scheme have been reached as theoretically predicted. For the secondary target of single-crystal germanium, the background experimental values decrease when increasing $E–E_{edi}$ more steeply than the theoretical ones. This is probably due to the anisotropy of scattering by a single crys-

tal, a fact that was not taken into account in the calculations. Therefore, for the single-crystal secondary target it was possible to obtain experimental results that were even better than those predicted theoretically (Table 3.4).

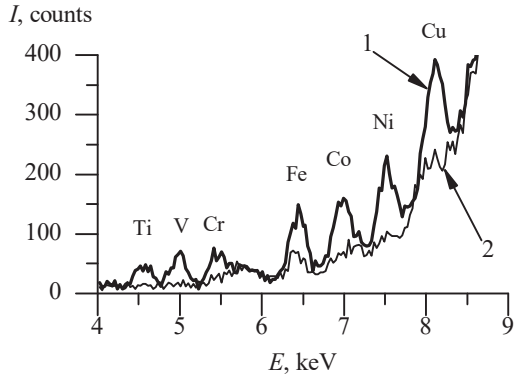

Figure 3.4: Fragment of the experimental spectrum for water solution standard samples with different "trace" impurities [37]. Impurity content: 1, 5 ppm and 2, 0.5 ppm.

The impurity detection limits in schemes with secondary targets of molybdenum and germanium were calculated from the experimental data in Table 3.4 (Fig. 3.5). In both cases, as the energy of the absorption edge is distanced from the energy of the secondary target line, the sensitivity of the analysis decreases, and the C_{min} increases. However, for a molybdenum target in the range from 7 to 13 keV, and for a germanium target from 6 to 9.7 keV, this change is barely noticeable: i.e. the excitation conditions are the same. Thus, with the selective excitation of the impurity fluorescence, it is appropriate to talk about the Z range of effectively excited elements [37]. For elements with the atomic number Z from 22 (Ti) to 30 (Zn), the value of E_{ed} lies in the range of 4.965 to 9.661 keV. The use of the germanium secondary target (E = 9.886 keV) makes it possible to

obtain a detection limit C_{min} that is five to six times smaller than with molybdenum target emitting E = 17.479 keV. Thus, the smaller the $E–E_{ed}$ difference, the higher the sensitivity of the analysis.

Table 3.4: Scattering background I_b (counts) and concentration sensitivity $\partial I / \partial C$ (counts/ppm); these are dependent on the absorption edge energy E_{ed} (keV) of impurities with a different Z. The secondary target is Mo (E = 17.479 keV) or Ge (E = 9.886 keV) and the accumulation time is 600 s.

	E_{ed}	Mo secondary target				Ge secondary target			
		Experiment		Calculation		Experiment		Calculation	
		I_b	$\frac{\partial I}{\partial C}$	I_b	$\frac{\partial I}{\partial C}$	I_b	$\frac{\partial I}{\partial C}$	I_b	$\frac{\partial I}{\partial C}$
Ti	4.965	177	2.16	185	4.9	105	22.0	316	15.3
V	5.464	265	6.10	243	7.9	120	33.0	415	25.0
Cr	5.989	306	11.00	313	12.0	220	51.5	534	38.6
Mn	6.538	351	19.81	412	17.5	320	63.0	686	56.5
Fe	7.111	682	26.06	537	25.8	520	82.0	869	83.7
Co	7.709	481	31.93	670	35.6	630	116	1041	116
Ni	8.331	629	38.92	798	51.0	830	150	1188	168
Cu	8.980	1232	38.07	905	68.0	2300	160	1260	224
Zn	9.661	930	85.54	1080	90.7	5300	250	1394	298
Se	12.66	2252	142.6	2104	219	–	–	–	–

Now consider the sensitivity required when using a germanium secondary target to determine elements where the $E– E_{ed}$ value is from 0.5 to 4 keV (Fig. 3.5, curve 2). When approaching the energy of the secondary target E

= 9.886 keV, the dependence of the C_{min} on the absorption edge E_{ed} falls sharply reaching a minimum of $C_{min} \approx 0.67$ ppm at $E - E_{ed} \approx 1.5$ keV and then it increases to $C_{min} \approx 1.1$ ppm. This growth is obviously caused by an increase in the background due to the imposition of the Compton scattering's "tail" from the secondary target line. Nevertheless, there is a fairly wide range of E_{ed} values from 6 to 9.5 keV where the value of C_{min} varies insignificantly (within 20 %). For chemical elements with E_{ed} in this range, the excitation conditions can be considered optimal. Thus, for selective exciting the fluorescence of impurities, it is appropriate to consider a range of effectively excited chemical elements that can use a specific secondary target. The width of this range, usually of 8 to 10 elements, should be taken into account when developing X-ray optical schemes.

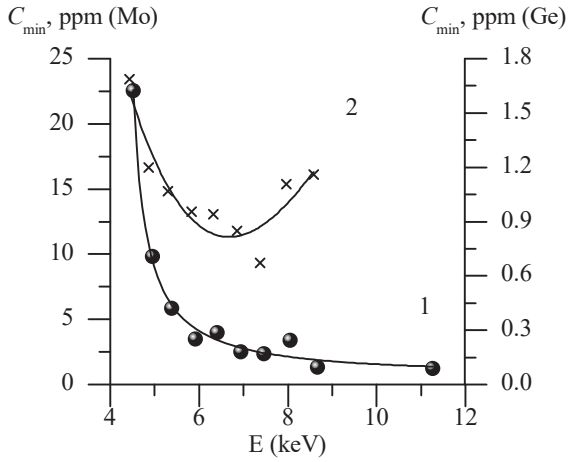

Figure 3.5: Experimental dependences of the detection limit for impurities in aqueous solutions based on the energy of their absorption edges: 1, Mo secondary target; and 2, Ge secondary target.

The coincidence of the theoretical calculations with the experimental results (Table 3.4) suggests that the scheme with a single-element secondary target provides a possibility of analyzing the content of "trace" impurities in the light matrix in the range of 8 to 10 chemical elements with their contents of 0.5 to 1 ppm; apparently, this is the limit of this scheme's analytical possibilities. Increasing the power of the primary radiation source from 7 W to 70 W will reduce the detection limit to 0.2 ppm.

In terms of the practical use of X-ray fluorescence analysis, it is often necessary to ensure the maximum sensitivity of the analysis in several Z ranges. This can be achieved with a complex target consisting of several secondary targets. However, the use of such a target will inevitably lead to a drop in the intensity of the lines.

3.1.3 Increasing the sensitivity of the scheme with a secondary target using primary radiation filtration

When using the scheme with a secondary target, it would be logical to use additional primary radiation filtering in the long wavelength spectral region [38]. Indeed, the characteristic line of the target excites the fluorescence of chemical elements. Its fluorescence, in turn, is excited by a harder radiation that is weakly absorbed by the primary radiation filter.

The filtration of the primary spectrum reduces the concentration sensitivity $\partial I_i / \partial C_i$ for the i-th element of the sample proportional to the intensity of the secondary target line or the intensity scattered by the sample material.

In other words, with the filtering:

$$\left(\frac{\partial I_i}{\partial C_i}\right)_f = \left(\frac{\partial I_i}{\partial C_i}\right)\exp\left(-\mu_f\ \rho\ t\right), \tag{3.4}$$

where I_i is the intensity of the i-th line after subtraction of the background; C_i is the concentration of the i-th element; ρ and t are the density and thickness of the filter, respectively; and μ_f is the empirical absorption coefficient determined from attenuation of the secondary target line scattered by the filter.

$$\mu_f = \frac{1}{\rho}\frac{1}{n}\sum_{k=1}^{n}\frac{1}{t_k}\ln\left(\frac{I}{I_{t_k}}\right), \tag{3.5}$$

where n is the number of primary filters with thickness t_k; and I and I_{tk} are the intensities of the secondary target line scattered by the sample without a filter and with a filter of thickness t_k, respectively.

For a light matrix and scattering angles $2\Theta \geq 100^o$, the Compton scattering is an order of magnitude higher than the Rayleigh scattering, so the value of μ_F can be determined by the decrease of the Compton line as the filter thickness is increased, rather than by the total scattering intensity.

In addition, the background consists of two components: the background (*a*) caused by the *scattering of the primary spectrum* by the secondary target and by the sample; and the background (*b*) associated with the *scattering of the secondary target line* by the sample (the "tail" of the Compton scattering) via the slits and details of the spectrometer, etc.

With the filtration of the primary radiation (primary filter), the background under the *i*-th line of the sample $I_B = a + b$ can be written in the following form:

$$\left(I_B\right)_f = a\exp\left(-\mu_i\, x\right) + b\exp\left(-\mu_f\, x\right), \tag{3.6}$$

where μ_i is the mass absorption coefficient of the primary filter material at the wavelength λ_i of the sample line; and $x = \rho \cdot t$ is the product of density per filter thickness.

Changing the detection limit $C_{\min f}$ when filtering relative to the initial value $C_{\min}$ in the scheme with a secondary target with allowance for (3.5) and (3.6) can be written in the following form:

$$\frac{C_{\min\, f}}{C_{\min}} = \left(1 + \alpha\exp\left[\left(\mu_i - \mu_f\right)x\right]\right)^{0.5}\exp\left[\left(\mu_f - 0.5\,\mu_i\right)x\right] \tag{3.7}$$

where $\alpha = b/a$ is the ratio of the background constituents.

Optimization of [3.7] for the x value according to the condition $\partial/\partial x = 0$ leads to the formula [38]:

$$X_{\text{opt}} = \frac{1}{\mu_i - \mu_f}\ln\left[\frac{0.5\,\mu_i - \mu_f}{0.5\,\alpha\,\mu_f}\right] \tag{3.8}$$

As it is seen from Table 3.5, the optimum thickness of the filter for different parts of the spectrum differs significantly; therefore, the choice of the filter thickness is not universal, although it is practically independent of the secondary target material.

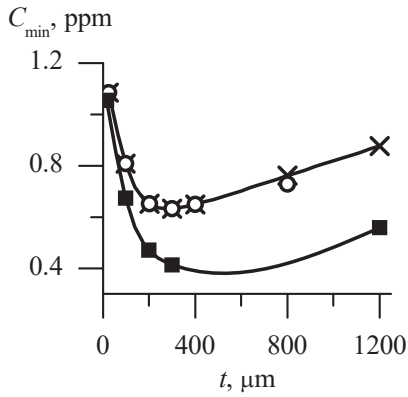

Figure 3.6: Detection limit of copper in aqueous solutions, which is dependent on the thickness of the primary radiation filter: × – Mo, b/a = 0.25; ○ – Y, b/a = 0.25; and ■ – Mo, b/a = 0.1.

Table 3.5: Optimal thickness of a silicon filter to achieve the minimal detection limits for copper and selenium in aqueous solutions (secondary targets are Mo and Y; α = *b*/*a* = 0.6).

Line \ Secondary target	Mo, *t* (μm)	Y, *t* (μm)
Se-Kα, *E*=11.2 keV	447	461
Cu-Kα, *E*=8.047 keV	268	249

The effectiveness of applying a filter to reduce the detection limit for copper in aqueous solutions is illustrated in Figure 3.6. A sharp decrease in C_{min} is observed with a small filter thickness, and it is even more noticeable with a small *b/a* ratio in the background components. Thus, the filtration efficiency increases when decreasing the contribution of the scattering of the secondary target line. If the measurement scheme provides the ratio

b/a = 0.25, then by means of the primary filtering it is easy to achieve a triple increase in the sensitivity using the C_{min} criterion and a fivefold increase in the contrast of the specific spectral line.

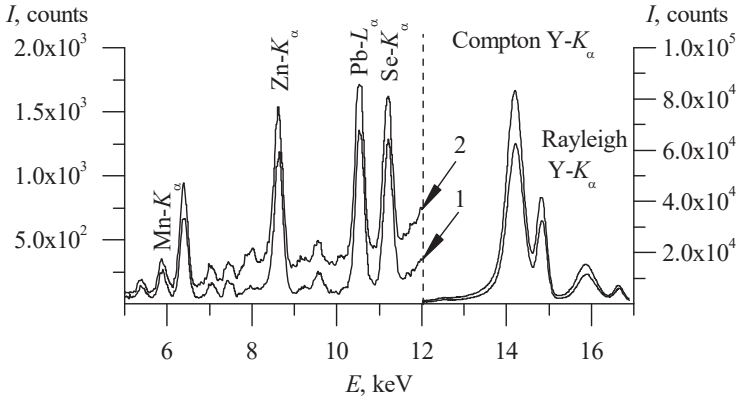

Figure 3.7: A spectrum of a standard sample of aqueous solution with 20 ppm content of selenium, zinc, and manganese: 1, with a silicon filter; and 2, without a filter. The secondary target is yttrium and the exposure is 600 s.

In the spectra of the standard samples of aqueous solutions, we observe an intense Compton scattering line, a weaker line of the Rayleigh scattering, (Fig. 3.7), and analytical lines of "trace" impurities: selenium, lead, zinc, and manganese. The measurements revealed a sharp increase in the contrast of the spectral lines when increasing the primary filter thickness and allowed us to calculate the value of μ_F from the change in intensity of the Compton scattering (Table 3.6). For the Mo secondary target, μ_f = 2.41 cm^2/g; for Y: μ_f = 3.16 cm^2/g. Based on the measurements of the background under the lines at four values of the filter thickness (0; 360; 720; 1080 μm), for each analytical line from Table. 3.6, the values of a and b

were calculated for the background components and their ratios (Table 3.7).

Table 3.6: Experimental intensities of Compton scattering, analytical lines, and the background for a standard sample of aqueous solution with 20 ppm of each impurity (Se, Zn, and Mn).

	Secondary target material Mo				Secondary target material Y			
Filter (Si) thickness, μm	0	360	720	1080	0	360	720	1080
Compton, counts· 10^3	68	54	48	38	83	62	52	38
Se-K_α, counts	1250	965	600	550	1600	1280	725	675
Background, counts	350	150	95	75	450	160	100	75
C_{min}, ppm	1.25	0.90	1.16	1.09	1.11	0.65	0.96	0.87
Zn-K_α, counts	1050	850	600	550	1520	1190	725	650
Background, counts	200	65	50	40	290	82	80	75
C_{min}, ppm	1.00	0.62	0.77	0.74	0.83	0.49	0.83	0.90
Mn-K_α, counts	250	200	175	150	350	250	200	150
Background, counts	100	55	50	50	105	60	50	40
C_{min}, ppm	4.00	3.07	3.39	4.24	2.51	2.45	2.83	3.45

According to Table 3.7, the ratio $b/a < 1$ is only characteristic to lines with an energy more than 8 keV (Zn-*K*α, Se-*K*α); therefore, the filtration can only be effective in a narrow range of energies near the secondary target line.

Table 3.7: The *b*/*a* ratio of the Compton scattering background *b* to the background *a* of the primary spectrum double scattering from different analytical lines

Line Secondary target	Se-Kα 11.2 keV *b*/*a*	Zn-Kα 8.63 keV *b*/*a*	Mn-Kα 5.89 keV *b*/*a*
Molybdenum	0.63	0.58	3.0
Yttrium	0.57	0.87	3.2

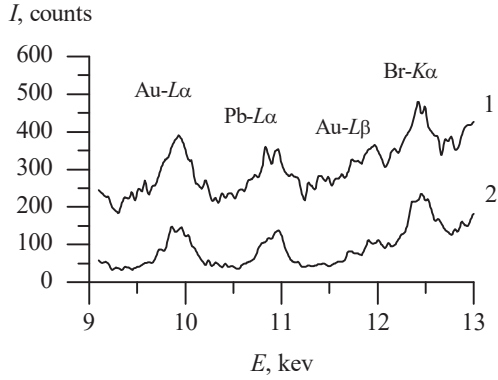

Figure 3.8: A fragment of the spectrum from a standard sample of gold in an ion-exchange resin (gold content is 10 ppm): 1, without a filter, C_{min} = 2.1 ppm; 2, with a filter optimized by thickness, C_{min} = 138 ppm. The secondary target is yttrium, the filter is silicon, and the exposure is 600 s.

Let us now discuss the increase in the sensitivity of the analysis when filtering the primary radiation (Table 3.6). Although C_{min} cannot be reduced by more than 70% with the ratio $b/a \approx 0.6$ implemented in our scheme, there is an increase in the contrast of weak signals by a factor of 3 to 4. You can achieve a triple increase in the sensitivity of the analysis by increasing the exposure. Thus, on the fragment of the spectrum of "trace" gold impurities in ion exchange resins (Fig. 3.8), we can observe how the proper filtration (curve 2) in the scheme with a secondary target ensured a threefold contrast increase compared to the same scheme without a filter (curve 1). The detection limit of Au calculated for the Au-Lα line by the curve 2 is 1.38 ppm [39].

3.1.4 Multilayer secondary targets and the optimization of layers by thickness and atomic number

The main disadvantage of the scheme with a secondary target is its limited ability to effectively excite the sample elements.

As it was defined in the last section, the high contrast of the fluorescence lines is provided for 8 chemical elements with absorption jumps near the secondary target line. The secondary target with a large atomic number excites the fluorescence of light elements inefficiently, and even a loss in the sensitivity of the analysis is possible in comparison with the standard XRF scheme. A natural solution to this problem would be the installation of two secondary targets: one for excitation of short and medium wavelengths, and the second for long-wave ranges. Such a solution can be realized with the help of a composite secondary target made of plates of different materials located in the same plane. The disadvantage of the scheme

is that each plate is illuminated only by a part of the primary source directional diagram. Consequently, the fluorescence intensity of each line of the composite target is always significantly lower than with the corresponding one-component target. Such a decrease in the target's luminosity would lead to a decrease in the concentration sensitivity and an increase in the background of scattering in the sample spectrum. An alternative solution is the two-layer secondary target, which is a thin film on a bulk substrate [40]. Such a secondary target is illuminated with the entire directional diagram of the primary source, but gives two groups of fluorescence lines: from the film and from the substrate materials. In such a secondary target, the upper layer serves to excite the lines of light elements and, at the same time, is the absorber of the continuous spectrum scattered by the lower layer. The lower layer gives hard radiation for the excitation of short and medium wavelengths.

Consider a secondary target in the form of a thin layer of the material Z_1, which has been deposited on a semi-infinite substrate of the material, Z_2. The layer Z_1 of density ρ_1 and thickness t dissipates the radiation with a wavelength λ in accordance with [1, 40]:

$$I_1(\lambda) = \frac{S}{r^2} \frac{\sigma_1(\lambda)}{\mu_1^*} \frac{\partial \Phi_{01}(\lambda)}{\partial(\lambda)} [1 - \exp\left(-\mu_1^*(\lambda)\rho_1 t\right)]$$
$$\mu_1^*(\lambda) = \mu_1(\lambda) \cdot \left(\frac{1}{\sin\varphi} + \frac{1}{\sin\psi}\right) \tag{3.9}$$

where $\sigma_1(\lambda)$ is the mass scattering coefficient; $\mu_1(\lambda)$ is the mass coefficient of attenuation by the layer; φ and ψ are angles of incident and exit of

the radiation, respectively; S is the irradiated area; and r is the distance between the tube and the secondary target.

The intensity of the scattering by a semi-infinite substrate located under the layer Z_1 is determined by the expression

$$I_2(\lambda)=\frac{S}{r^2}\frac{\sigma_2(\lambda)}{\mu_2^*}\frac{\partial\Phi_{01}(\lambda)}{\partial\lambda}\exp\left(-\mu_1^*(\lambda)\rho_1 t\right)$$
$$\mu_2^*(\lambda)=\mu_2(\lambda)\cdot\left(\frac{1}{\sin\varphi}+\frac{1}{\sin\psi}\right) \tag{3.10}$$

where $\mu_2(\lambda)$ is the mass attenuation coefficient by the substrate and the exponent corresponds to the absorption in the upper layer .

Then the total intensity of the scattering by the secondary target $I_s = I_1 + I_2$. This can be written in the form

$$I_S(\lambda)\sim\frac{\sigma_1}{\mu_1^*(\lambda)}-\exp\left(-\mu_1^*(\lambda)\rho_1 t\right)\left(\frac{\sigma_1}{\mu_1^*(\lambda)}-\frac{\sigma_2}{\mu_2^*(\lambda)}\right). \tag{3.11}$$

It follows from (3.11) that, depending on the thickness of the upper layer, the level of scattering the radiation with wavelength λ is in the range from $\frac{\sigma_1}{\mu_1^*(\lambda)}$ at $t\to\infty$ (scattering by the upper layer of infinite thickness) to $\frac{\sigma_2}{\mu_2^*(\lambda)}$ at $t\to 0$ (scattering by the substrate).

Let the absorption band edge wavelength of the substrate, λ_{ed2}, be less than λ_{ed1} of the coating material. Then for wavelengths from the range of $\lambda_{ed2} < \lambda < \lambda_{ed1}$ the condition is $\frac{\sigma_1}{\mu_1^*(\lambda)} < \frac{\sigma_2}{\mu_2^*(\lambda)}$: i.e. the scattering before the absorption jump of the coating is less than that behind the absorption jump of the substrate.

Calculations show (Fig. 3.9) that the titanium coating in the Ti/Ag secondary target allows us to reduce significantly the background of the scattered radiation: i.e., to improve the contrast in the indicated wavelength range in comparison with the solid silver secondary target. However, in this case, the intensity of the fluorescent radiation emerges from the substrate through the decrease in the coating.

For a single-component substrate under a layer (film) of thickness t, by analogy with [1, 10], the intensity of the analytical line λ_2 can be written as

$$I(\lambda_2, t) = \frac{S}{r^2} \cdot \left(1 - \frac{1}{S_{q2}}\right) \cdot \omega_2 \cdot p_2 \int_{\lambda_0}^{\lambda_{q2}} \frac{\tau_2(\lambda)}{\mu_2^*(\lambda)} \cdot \frac{\partial \Phi_{01}(\lambda)}{\partial \lambda} \cdot \exp\left(-\mu_1^* \rho_1 t\right) d\lambda,$$
$$\mu_1^*(\lambda) = \frac{\mu_1(\lambda)}{\sin\varphi} + \frac{\mu_1(\lambda_2)}{\sin\psi}, \quad \mu_2^*(\lambda) = \frac{\mu_2(\lambda)}{\sin\varphi} + \frac{\mu_2(\lambda_2)}{\sin\psi}. \tag{3.12}$$

where $\tau_2(\lambda)$ is the mass coefficient of absorption by the substrate material; the exponent describes the attenuation of the incident $\mu_1(\lambda)$ and emergent $\mu_1(\lambda_2)$ beams by the film; ω_2 is the fluorescence yield; p_2 is the portion of the analytical line intensity in the spectral series; and S_{q2} is the absorption jump value.

For a single-component film, the intensity of the analytical line $\lambda_1$is written as [1, 4, 40]

$$I(\lambda_1,t)=\frac{S}{r^2}\left(1-\frac{1}{S_{q1}}\right)\omega_1\ p_1\int_{\lambda_0}^{\lambda_{q1}}\frac{\tau_1(\lambda)}{\mu_1^*(\lambda)}\frac{\partial\Phi_{01}(\lambda)}{\partial\lambda}\left(1-\exp\left(-\mu_1^{**}\rho_1\ t\right)\right)d\lambda,$$

$$\mu_1^{**}(\lambda)=\frac{\mu_1(\lambda)}{\sin\varphi}+\frac{\mu_1(\lambda_1)}{\sin\psi}, \tag{3.13}$$

where $\mu_1(\lambda)$ and $\mu_1(\lambda_1)$ are mass coefficients of attenuation by the film material for the incident and emergent radiations, respectively; and $\tau_1(\lambda)$ is the mass coefficient of absorption by film atoms.

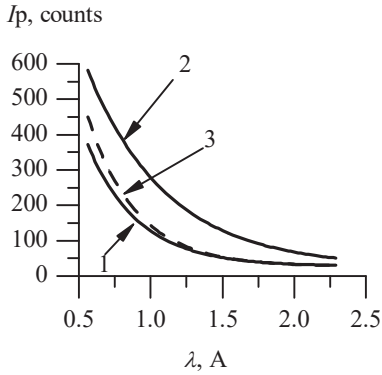

Figure 3.9: Calculated scattering intensities depending on the wavelength: 1, solid titanium secondary target; 2, solid silver secondary target; 3, two-layer secondary target Ti (50μm)/Ag (bulk).

When a secondary target irradiates the sample, the intensity of the *i*-th analytical line of the atoms with the concentration of C_i is expressed as [40]

$$I_i = C_i\left\{ I(\lambda_2;t)\Pi(\lambda_2-\lambda_{edi})\frac{\tau_{2i}}{\mu^*_{2i}} + I(\lambda_1,t)\Pi(\lambda_1-\lambda_{edi})\frac{\tau_{1i}}{\mu^*_{1i}} \right\}, \tag{3.14}$$

$$\mu^*_{1i} = \frac{\mu_s(\lambda_1)}{\sin\varphi_s} + \frac{\mu_s(\lambda_i)}{\sin\psi_s}, \qquad \mu^*_{2i}(\lambda) = \frac{\mu_s(\lambda_2)}{\sin\varphi_s} + \frac{\mu_s(\lambda_i)}{\sin\psi_s},$$

where μ_s is the mass attenuation coefficient for radiations with wavelengths λ_1, λ_2 and λ_i; $\Pi(x) = \begin{cases} 1, \text{if } x > 0; \\ 0, \text{if } x \le 0. \end{cases}$ is a step function; λ_1 and λ_2 are wavelengths of film and substrate materials, respectively; and λ_i is the wavelength of the sample's analytical line.

The intensity of the radiation scattered from the sample, I_{sc}, is obtained by multiplying (3.14) the corresponding expression of σ_s / μ_s. Then the contrast $K = I_{fl}(\lambda_i) / I_{sc}(\lambda_i)$ for different analytical wavelengths λ_i depends on the thickness t of the upper layer. Solving the extreme-value problem for the contrast $\partial K/\partial t = 0$ gives the value of the optimal coating thickness:

$$t(\lambda) = \frac{1}{\rho_1 \cdot \mu^*_1(\lambda)} \cdot \ln\left\{ \frac{\left(\frac{\sigma_1(\lambda)}{\mu_1(\lambda)} - \frac{\sigma_2(\lambda)}{\mu_2(\lambda)}\right)\cdot\left(\mu^*_1(\lambda_2) - \mu^*_1(\lambda)\right)}{\mu^*_1(\lambda_2)\cdot\frac{\sigma_1(\lambda)}{\mu_1(\lambda)}} \right\}. \tag{3.15}$$

Direct calculations for the Ti/Ag pair showed that the optimal thickness of the titanium layer in the wavelength range of 0.71 Å to 2.29 Å decreases from 20 μm to 10 μm when approaching the absorption jump of the titanium coating.

In Figure 3.10, the calculated contrast $K = I_{fl}(\lambda) / R(\lambda)$ of analytical lines from impurities in concentrations of C = 1% mass is shown: molybdenum (λ = 0.71 Å), gallium (λ = 1.25 Å), copper (λ = 1.54 Å), chromium (λ = 2.29 Å), chlorine (λ = 4.7 Å), silicon (λ = 7.11 Å), and magnesium (λ = 9.9 Å) in the iron matrix. Obviously, the contrast of the lines' "trace" impurities in the iron matrix under irradiation with the two-layer Ti/Ag secondary target is two to three times higher than for the secondary target made of solid silver. The most effective contrast is observed for light element lines, such as sulfur, phosphorus, or silicon.

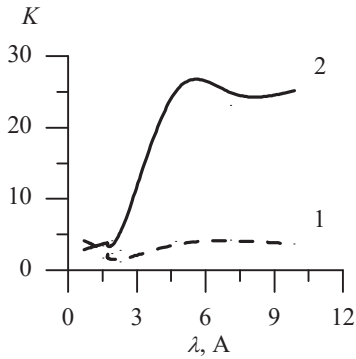

Figure 3.10: Calculated contrast (K) for analytical lines depending on their wavelengths for impurities in iron: 1, a single Ag secondary target; and 2, a double-layer Ti (20 μm)/Ag secondary target.

It is convenient to compare the Ti/Ag secondary targets via the spectral distributions of radiation scattered by a high-purity amorphous carbon. This material has no absorption jumps in the considered range and adequately reflects the spectrum of the secondary target.

The intensity of the scattering peaks of the silver *K*-series fluorescence lines in the amorphous carbon scattering spectrum determines the fluorescence intensity of element lines whose absorption edge λ_{edi} is in the range $\lambda_{Ag} < \lambda_{edi} < \lambda_{Ti}$. The intensity of the scattering peaks of titanium fluorescence lines determines the fluorescence intensity of light elements where $\lambda_{edi} > \lambda_{Ti}$.

As the upper (Ti) layer of the secondary target becomes thicker, the fraction of titanium lines in the carbon scattering spectrum increases, reaching an asymptotic value of ≈ 0.37 at t_{Ti} ≈100 μm (Fig. 3.11). This means that the fluorescence intensity of the light elements in the sample irradiated by such a secondary target will increase and reach their highest value at t_{Ti} =100 μm. At the same time, the silver K_α line, which has been weakened by the upper layer of the secondary target, decreases monotonically; this leads to a decrease in the intensity of the analytical lines in the range of $\lambda_{Ag} < \lambda < \lambda_{Ti}$. Thus, with a two-layer Ti/Ag secondary target, it is possible to achieve a significantly increased intensity ratio of light element lines to the lines from the remaining elements in the spectrum of the sample.

According to the calculations for the Ti/Ag secondary target, the contrast of the phosphorus line with its content in the steel C_p = 0.6% mass should be K = 6.9, which is very close to the experimental value

$$K = \frac{I - I_b}{I_b} = \frac{(380 - 90)}{90} = 3.2.$$

The detection limit of 0.005 to 0.01% mass for these elements is quite sufficient for measuring cast iron and steel.

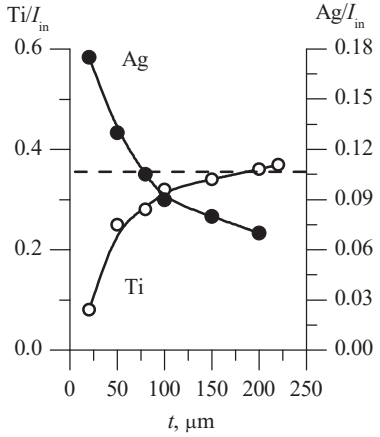

Figure 3.11: Experimentally measured fractions of the Ti-Kα and Ag-Kα lines in the amorphous carbon scattering spectrum obtained using Ti/Ag secondary targets with different thicknesses t of titanium coatings.

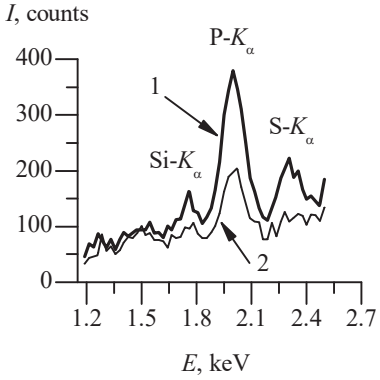

Figure 3.12: A fragment of the spectrum of a standard cast iron sample with lines of silicon, phosphorus, and sulfur. The mass fractions of these elements are 0.3, 0.6, and 0.15%, respectively; 1, a two-layer Ti/Ag secondary target; 2, a solid Ag secondary target [40].

Let us compare the experimental intensities of impurity analytical lines and the background level in different parts of the spectrum obtained using a solid Ag secondary target or two-layer Ti/Ag secondary targets with different titanium layer thicknesses. We used State Standard Samples of cast iron with sulfur and phosphorus contents in the range of 0.005% to 0.67% of mass, and silicon in the range of 0.2 to 1.14% mass. The normalization was carried out by the integrated intensity of the spectrum. Indeed, the use of the two-layer secondary target provided a gain in the intensity of the analytical lines of silicon, phosphorus, and sulfur in cast iron compared to the silver secondary target (Fig. 3.12). This made it possible to increase the sensitivity by 3–4 times in these elements.

Consider the results of measuring the background scattered by amorphous carbon at $\lambda = 0.78$ Å (i.e. near the silver substrate Compton line $\lambda = 0.59$ Å [Fig. 3.13, curve 1]) and at $\lambda = 2.26$ Å (i.e. near the titanium coating absorption edge $\lambda_{edTi} = 2.5$ Å [Fig. 3.13, curve 2]). Curve 2 drops to an asymptotic value at a coating thickness of 20 μm, and the further increase in thickness does not result in reducing the background, but the fluorescent yield of Ag-*K* radiation does decrease. Thus, the maximum contrast of lines with $\lambda < \lambda_{edTi}$ is ensured at $t \approx 20$ μm. For the wavelength $\lambda = 0.78$ Å, the background continues to slowly decay in the range of t from 20 to 200μm after a rapid fall in the initial section of the curve. This difference between the curves in Figure 3.13 confirms the conclusion that there is no single optimal value of Ti coating thickness t for the entire wavelength range.

Theoretical and experimental studies show that the two-layer Ti/Ag secondary target provides a significant reduction in the scattering background and increased contrast of fluorescence lines in comparison with the solid Ag in the wavelength range between the analytical line Ag-K_α of the substrate and the absorption edge λ_{ed} of the titanium coating. Thus, the sensitivity of the analysis increases in this range. A multilayer secondary target that combines the functions of a secondary target and a primary radiation filter provides a number of advantages when contrasting the spectrum in comparison with primary and secondary radiation filters.

As expected, a large gain in the intensity of the analytical lines of the spectrum is observed for $\lambda > \lambda_{Ti}$: i.e., for the lines of light elements.

High intensity *K*-series lines of the coating material (Ti) are located quite close to the absorption edges of the Periodic Table's third period elements, so they excite them more efficiently than the *L*-series lines of the silver substrate material. This means that the two-layer secondary target significantly expand the wavelength range of effective excitation and, consequently, of highly sensitive analysis. In accordance with [3.15], the optimum thickness t_{opt} of the coating depends on the wavelength λ of the detected line. For example, for a Ti/Ag pair in the range of $\lambda_{Ag} < \lambda < \lambda_{Ti}$ the value of t_{opt} near λ_{Ag} is 2.5 times larger than near λ_{Ti}. Therefore, the practical choice of the coating's thickness is subjective depending on the importance of contrasting a wavelength range.

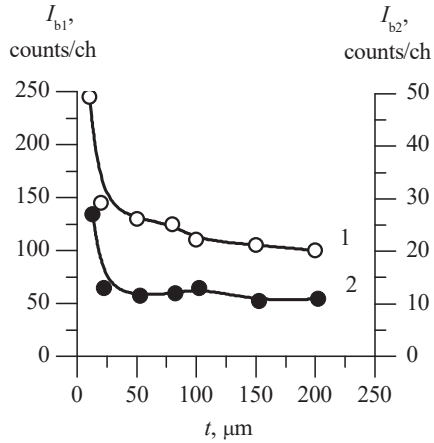

Figure 3.13: Background intensity (counts per channel) of the radiation scattered by amorphous carbon for wavelengths λ_{b1} = 0.78 A (curve 1) and λ_{b2} = 2.26 A (curve 2) depending on the thickness t of the titanium coating for the Ti/Ag two-layer secondary target.

A two-layer secondary target, in comparison with a homogeneous one, provides an increase in the analysis sensitivity over the entire wavelength range. This is caused by a three to fourfold gain in the excitation efficiency of the light elements for which $\lambda_{ed} > \lambda_1$, and a two or threefold increase in the contrast of lines located in the range of $\lambda_1 > \lambda_{ed} > \lambda_2$. This effect is greater the closer λ is to the absorption edge of the coating.

3.1.5 Experimental study of the characteristics of a two-stage fluorescent lens

X-ray optic scheme and directional diagram

Since the decrease of the background signal in the X-ray optical scheme with the secondary target occurs due to multiple scattering of the continu-

ous spectrum, it would be reasonable to equip the scheme with an additional sequential secondary target. This, of course, would lead to a loss of luminosity, but you can choose the materials for the tube anode, as well as the primary and secondary fluorescent targets, so that the intensity of the radiation that excites the fluorescence of the analyzed elements is maximized. Consider the original design (double lens) [41], which is easily mounted (worn) on the spout of an X-ray tube with a shoot-through type anode and does not require additional adjustment (after fixing the lens assemblies). The schematic drawing of the device is shown in Figure 3.14.

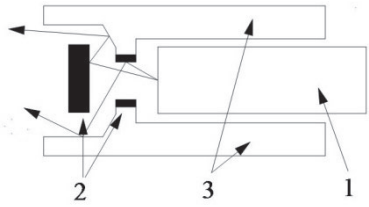

Figure 3.14: Schematic drawing of a Mo+Cu two-stage secondary target: 1, X-ray tube; 2, first stage of the secondary target; and 3, second stage of the secondary target.

The primary radiation of the BS-22 shoot-through tube (with a silver anode) hits the first stage of the secondary target (Mo material) and excites fluorescent radiation, while part of the spectrum energy is scattered, thereby creating a broadband background. The fluorescent radiation (Mo-Kα) and the background fall on the second stage of the secondary target (Cu material). Thus, the spectrum of the two-stage secondary target is a superposition of copper fluorescence lines, molybdenum fluorescence lines

scattered at the second stage of the secondary target, and the tube's scattered continuous spectrum, which creates the background.

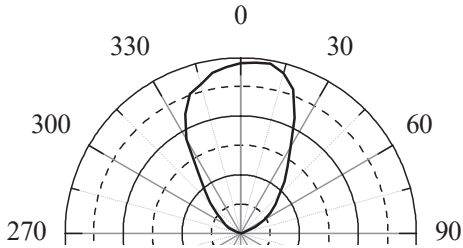

Figure 3.15: Directional diagram of a two-stage secondary target

We will start by studying the directional diagram. The intensity of the Cu-*Kα* analytical line was measured every five degrees in the angle range of -70° to 70°, with a distance of 40 mm to the detector window. The diagram shows a half-width of about 70° (Fig. 3.15), which is less than that of the primary radiation source used (BS-22 tube). The 5° offset of the diagram axis relative to the geometric axis of the device may be due to the imperfect assembly of the miniature nodes of the device and is not taken into account in the future. The device alignment, which ensures the purity and contrast of the outgoing spectrum, is carried out by micrometric feeds in the first stage of the secondary target (Fig. 3.14, pos. 2).

Estimation of detection limits

In view of the low power of the primary source, the beam generated by the device is sent directly to the detector when studying the double lens spectrum.

The spectrum was registered with an exposure time of 300 s and a voltage of 30 kV on the tube. The normalization was carried out by the Cu line peak intensity. In order to conveniently observe both the analytical line and background, the obtained spectrum is given in the logarithmic scale in Figure 3.16.

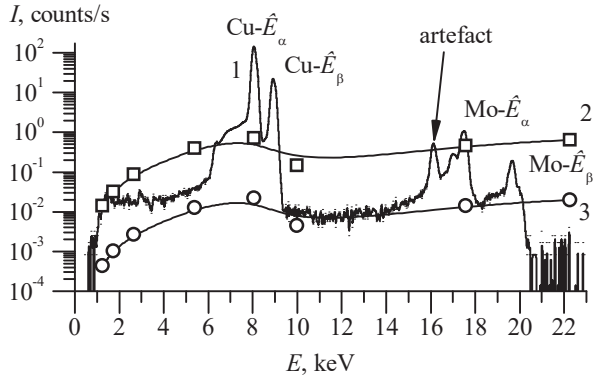

Fig. 3.16: 1, spectrum of the Mo+Cu secondary target (experiment); 2, background of the Cu secondary target (calculated); and 3, background of the Mo+Cu secondary target (calculated).

The same figure shows the theoretically calculated background signals for the two-stage (Mo + Cu) and single (Cu) secondary targets. As expected, the main lines are the copper analytical line (with intensity of 148 counts per second) and the scattered line of molybdenum. The numerical values of the background and the calculated contrast of the experimental spectrum in the range of energies smaller than the energy of the analytical copper line are given in Table. 3.8. In the spectrum we can observe the following: the molybdenum K_α and K_β fluorescence lines scattered by the second stage of the secondary target (Cu), the copper K_α and K_β lines, the

total artifact peak of copper, and the doubly scattered background of the X-ray tube's continuous spectrum. The spectrum contrast of the two-stage secondary target is 20–50 times higher than that of a conventional single-stage secondary target. The experimentally achieved background characteristics are close to those calculated for the two-stage secondary target model (Fig. 3.16, curve *3*). These results are much better than the characteristics found with the single-stage secondary target (Fig. 3.16, curve *2*). This means that the sensitivity of the sample composition analysis using a two-stage secondary target can be one and a half orders of magnitude higher.

Table 3.8: Comparison of theoretically calculated and experimental spectra (in relative units) for single (Cu) and two-stage (Mo + Cu) secondary targets.

Line	Mo+Cu	Cu	Experiment	Contrast
Cr-K_α (5.41 keV)	$12.80 \cdot 10^3$	$409.37 \cdot 10^3$	$39.92 \cdot 10^3$	3.7
Cl-K_α (2.62 keV)	$2.72 \cdot 10^3$	$87.15 \cdot 10^3$	$16.90 \cdot 10^3$	8.8
Si-K_α (1.74 keV)	$1.02 \cdot 10^3$	$32.57 \cdot 10^3$	$20.19 \cdot 10^3$	7.4
Mg-K_α (1.25 keV)	$0.44 \cdot 10^3$	$14.12 \cdot 10^3$	$15.50 \cdot 10^3$	9.6

The advantages of the two-stage secondary target when measuring "trace" impurities are visible on a fragment of the spectrum for a standard aluminum alloy with a chromium content of 13 ppm (Fig. 3.17). The standard

scheme using the filtration of the primary radiation provides a chromium line contrast of $K < 2$ (Fig. 3.17, curve 1), the scheme with a single-stage Cu secondary target gives $K \approx 7$ (not shown in the figure), and the scheme with the two-stage secondary target shows $K > 12$ (Fig. 3.17, curve 2). This means that when analyzing Cr in aluminum alloys in the scheme with the two-stage secondary target, the sensitivity is at least 6 times higher than in the standard one.

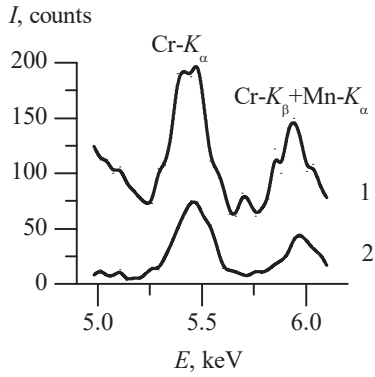

Figure 3.17: A fragment of an aluminum alloy standard sample spectrum with a chromium content of 13 ppm: 1, scheme with filtration and 2, scheme with a two-stage secondary target.

We believe that two-stage secondary targets in combination with powerful sources of primary radiation are rather promising and allow us to achieve the highest detection limits in XRF.

3.2 Quantitative X-ray phase analysis using secondary target fluorescence lines

The quantitative X-ray phase analysis provides important information about the structure of the material. This information, together with the data on the composition, is used to validate the object. To study the structure of the sample and its chemical composition, two alternative X-ray optical schemes are commonly used: XRD analysis is performed under conditions of small angular divergence of the beam ($\Delta\theta \approx 0.01– 0.05°$), and XRF analysis is carried out at the maximum divergence ($\Delta\theta \approx 4–30°$). Despite the fundamental differences in the schemes, the fluorescence spectra always contain the spectral lines of the exciting radiation scattered by the sample. Traditionally, these lines are an obstructing factor in XRF (Section 1.8.2) [1, 2]. Nevertheless, the combination of X-ray diffraction and X-ray fluorescence schemes in the same device would solve many applied problems.

It is possible to determine the content of light impurities using secondary target fluorescence lines to excite diffraction reflections for corresponding phases in multiphase systems (oxides, carbides, etc.).

The fluorescence of the chemical elements of the sample is excited by the fluorescence lines of the secondary target material, which is optimized in accordance with the principles described above. In the X-ray spectrum of the sample, there are fluorescence lines from its chemical elements, as well as lines from the secondary target, which are scattered by the sample. By analogy with the standard XRD, the secondary target can be considered as a source of primary radiation (an “X-ray tube”). However, a significant

fraction of the continuous spectrum is present in the radiation of a usual X-ray tube excited by an electron beam. This spectrum, which is scattered on the sample, creates an unwanted background that must be removed in various ways (monochromatization, filtering, amplitude discrimination of signals, etc.). In this sense, the secondary target as an X-ray source is more attractive, since the component of the continuous spectrum is much smaller than that of the X-ray tube.

However, if the fluorescent radiation of the secondary target with a wavelength λ falls on the surface of the sample at an angle θ corresponding to the Bragg condition, then we observe a diffraction reflection of the crystal lattice of the sample under investigation. This means that a portion of the diffraction pattern appears in the fluorescence spectrum of the sample. The diffraction reflections correspond to the secondary target line wavelengths using photo energies and are located in strictly defined areas of the X-ray spectrum. The appearance of a diffraction reflection from the crystallographic planes (*hkl*) is determined by the Bragg condition: $2d_{hkl} \cdot \sin(\theta \pm \Delta\theta) = \lambda$, where λ is the wavelength of the secondary target fluorescence, d_{hkl} is the interplanar distance, and $(\theta \pm \Delta\theta)$ is the range of diffraction angles realized in the experiment. If the angle θ increases monotonically, then the Bragg condition is consistently satisfied for all d_{hkl} of the sample, as in the ordinary XRD. By adjusting the Bragg angle, which corresponds to the value of d_{hkl}, a quantitative X-ray phase analysis can be performed.

3.2.1 Quantitative X-ray phase analysis of steel using ferrite and cementite Bragg reflections

A clear example of the application of such a method is the analysis of steel [42, 43], where determining the content of light elements—aluminum,

silicon, phosphorus and sulfur, as well as all alloying elements—is carried out using the intensity of fluorescence lines. At the same time, the carbon content can be determined by α-Fe and Fe_3C (cementite) diffraction reflections, if they are in spectrum regions free from the sample's fluorescence lines [43].

Steel casting not subjected to special heat treatment can be considered to be a two-phase system in accordance with the quasi-binary iron-cementite (α-Fe – Fe_3C) phase diagram [44]. The α-Fe phase does not contain carbon, so it is appropriate to correlate the carbon content in steel with the amount of the carbon-containing phase, cementite (Fe_3C), which contains 6.67% mass of stoichiometric carbon. In other words, the 1% mass fraction of carbon in steel corresponds to the 15.0% mass fraction of Fe_3C. The quantitative X-ray phase analysis of the two-phase α-Fe-Fe_3C system can be performed separately using the lines from each phase, thereby taking into account that with an increasing carbon content in steel, the amount of α-Fe decreases, and the amount of Fe_3C increases. An increase in the carbon content in steel from 0 to 1% mass corresponds to an increase in the cementite content from 0 to 15% mass and, consequently, a decrease in the content of α-Fe from 100 to 85% mass.

The calculation is carried out according to the known relation [25, 45]

$$\frac{I}{I_0} = \frac{x_1 \times \mu_1}{x_1 \times (\mu_1 - \mu_2) + \mu_2}, \tag{3.16}$$

where I_0 is the relative intensity of a diffraction reflection from the pure phase (α-Fe); I is the relative intensity of the same reflection in the binary

mixture; μ_1 and μ_2 are absorption coefficients of the constituent phases (cm^2/g); and x_1 is the concentration of the phase being determined.

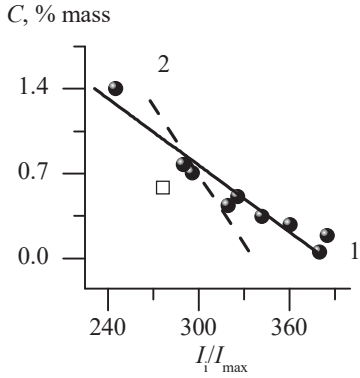

Figure 3.18: The calibration function to determine the carbon content in low-alloy steel using the (310) reflection integrated intensity of α-iron: *1*, experimental curve for SSS from the 127 set; and *2*, calculated curve without taking into account the texture change.

According to (3.16), the intensity of the α-Fe reflection should decrease from 1 to 0.858 ($\mu_1 = \mu_{Fe}^{Cu-K\alpha}$ =308; $\mu_2 = \mu_{Fe_3C}^{Cu-K\alpha}$ =288; x_1 = 0.85) with a 1 % increase of the carbon content. The objects of the investigation were state standard samples (SSS) of carbonaceous and low-alloy steels (sets 127, 154 and UG). X-ray diffraction analyses were performed using a continuous recording mode with a DRON-2 diffractometer in the filtered radiation of a chromium anode, and with a DRON-3M diffractometer, where the Cu-Kα radiation was monochromatized by (002) graphite in the diffracted beam using the discrete scanning mode with an accumulation time of 40 s at each measurement point. The error when measuring the

integrated intensity of the α-iron (110), (200) and (310) diffraction lines did not exceed 0.5%, and for the cementite lines it was 1–5%, depending on their intensity.

Table 3.9: The measured intensities of α-Fe (110), (200), and (310) reflections found in SSS from the 127 set. I_{110} and I_{200} are peak intensities (counts/s); and I_{310} is the integrated intensity (arbitrary units).

Sample number	*C*,%	I_{110}	I_{200}	I_{310}
127-14	0.053	1296	128	380
127-2	0.670	1536	196	380
127-3	0.185	1048	148	385
127-4	0.276	1328	184	360
127-5	0.296	1304	184	340
127-6	0.348	1200	148	342
127-7	0.431	1144	120	320
127-8	0.490	1512	136	320
127-9	0.509	1256	120	325
127-10	0.703	1136	116	295
127-11	0.770	1344	128	290
127-12	0.970	1320	112	270
127-13	1.400	1352	96	245

Figure 3.18 shows the experimental (curve 1) and calculated (curve 2) dependences of the α-Fe (310) reflection integral intensity on the carbon content for the SSS of the 127 set. The experimental plot has a much greater slope than the calculated one: 34% of the change in intensity indicating 1% change in the carbon content. It is likely that such a large effect

is associated with a texture change within the SSS 127 set. The result of the analysis of the UG20 sample from the UG set is marked as (□). As might be expected, the points for samples of different sets generally do not lie on the same curve, as evidenced by the "spike" of the point for steel from the UG set. The experiment shows (Table 3.9) that the intensity ratio of the first two α-Fe reflections (110) and (200) doubles with an increase in the carbon content from 0.03 to 1.4% mass, which indicates a change in the texture.

According to Table 3.9, we calculated the pole density P_{hkl} [46] for reflections from the (110), (200), and (310) planes, which were in the same plane as the pole figure (Fig. 3.18).

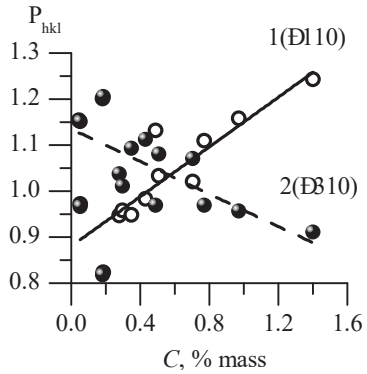

Figure 3.19: The determination of the pole density *P* for reflections (110) (curve 1) and (310) (curve 2) depending on the carbon content in a series of SSS.

In Figure 3.19, the texture change with an increasing carbon content is clearly visible in SSS of the 127 set. The determination of the carbon content via the (110) reflection is inadvisable, because the intensity increase

due to texture changes from an increasing carbon concentration reduces the sensitivity.

From the intensity of the (310) reflection within the same SSS series, we have got a calibration function with a standard deviation $S = 0.089$ % mass, which is acceptable for rapid assessment measurements.

3.2.2 Quantitative phase analysis of ferrite and cementite using an X-ray fluorescence spectrometer

In the X-ray fluorescence spectrometer scheme, there are two main factors that make it difficult to quantify the carbon content from the Bragg reflection intensity. One of them is associated with the change in texture, as discussed above, and the other is connected with the superposition of diffraction reflections and the sample's analytical fluorescence lines. A significant decrease in the influence of the texture can be achieved if the diffraction reflections with "medium" Miller indices are measured. For example, we used a gold anode to analyze iron. The lines of the gold *L*-series allow us to obtain α-Fe diffraction reflections with medium indices.

According to the Table 3.10, we chose the angle $2\theta \approx 71 \pm 4°$ so that the Au-L_β line (310) reflects α-Fe, the Au-L_γ line (321) reflects α-Fe, and the Au-$L_{\alpha\ \text{line}}$ is adjusted between the (211) and (220) α-Fe lines. In the interval between the (211) and (220) α-Fe reflections, there are at least two cementite reflections; the intensity of which is conveniently measured simultaneously. Setting up in the middle of the interval and limiting the angular divergence of the spectrometer to the value $\Delta 2\theta \approx 6 \div 7°$, we obtain two independent calibration functions for determining the carbon content. The

first one determines the α-Fe amount from the intensity of the (310) reflection in the Au-L_β radiation (Fig. 3.20, *a*), while the second one determines the cementite amount using the totality of (134) and (330) reflections in the Au-L_α radiation (Fig. 3.20, *b*).

Table 3.10: Calculated Bragg doubled angles 2θ for gold spectral lines diffracted by the main phases: α-iron and cementite in the chosen angular range 2θ = 71 ± 4°

Line	λ, Å	(211) α-Fe d = 1.166	(134) Fe_3C d = 1.150	(330) Fe_3C d = 1.126	(220) α-Fe d = 1.010	(310) α-Fe d = 0.904
Au L_α	1.276	66.3	67.4	69.0	78.3	89.8
Au $L_{\beta1}$	1.084	–	–	57.5	64.9	73.6

The first type calibration function gives the standard deviation $S \approx 0.10\%$ mass within one set of SSS. However, a large standard deviation ($S \geq 0.20\%$ mass, Fig. 3.20, *a*) for the first type curve makes it unusable in practice when using several SSS sets. The nonidentity of the calibration functions is clearly manifested in various sets. The second curve obtained with three SSS sets gives $S \approx 0.09\%$ mass and shows a high sensitivity: 50% of the signal variation per 1% of the carbon content mass change. This curve (Fig. 3.20, *b*) is suitable for carbon quantitative analysis even for different sets of standard samples. A disadvantage is that in the scheme with the anode line diffraction it is difficult to measure the small amounts

of other light elements commonly present in steels—namely silicon, phosphorus, and sulfur—because of the high background level.

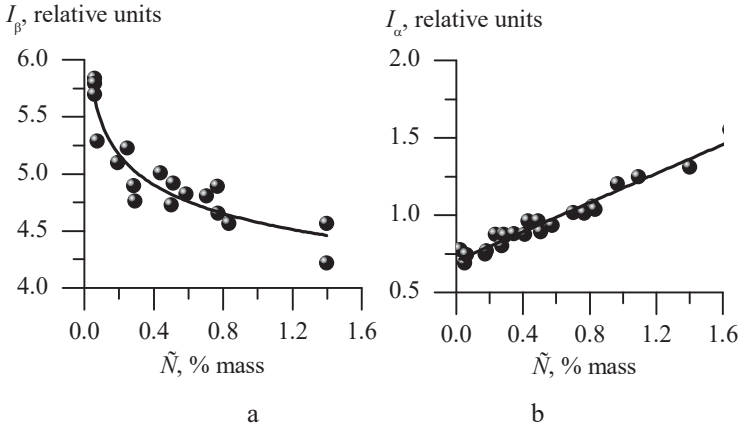

Figure 3.20: The calibration function used to determine carbon by the intensity of gold anode diffraction lines: a, by decreasing the α-Fe (310) line intensity in the Au-*L*β1 radiation without correction for texture change, I_β; and b, by increasing the intensity of (134) and (330) cementite lines in Au-*L*α radiation, I_α.

3.2.3 Quantitative analysis using cementite reflections with a secondary target

Measurement scheme

Cementite possesses a complex crystalline lattice, which gives many diffraction lines. However, their intensity in carbon steel's diffraction pattern is one or two orders of magnitude lower than the intensity of α-Fe lines. Therefore, quantitative analysis using single Fe_3C lines is difficult due to the insufficient intensity of the analytical signal. Nevertheless, when capturing several lines with a proper background reduction, it is possible to

obtain good quality calibration functions and to determine the carbon content in low-alloyed cast product using the amount of Fe_3C. The device's X-ray optical scheme with a complex secondary target is shown in Figure 3.21. Diffraction reflections from the sample are obtained in the secondary target light, which emits the scandium, potassium, and chlorine fluorescence lines (λ= 3.03 Å, 3.74 Å, and 4.74 Å). These lines are located in the λ range of 2.8 Å to 5 Å, where there are no fluorescence lines from the chemical elements that are constituents of the steel. Therefore, their treatment does not require taking into account the superimposition of fluorescence lines and diffraction reflections.

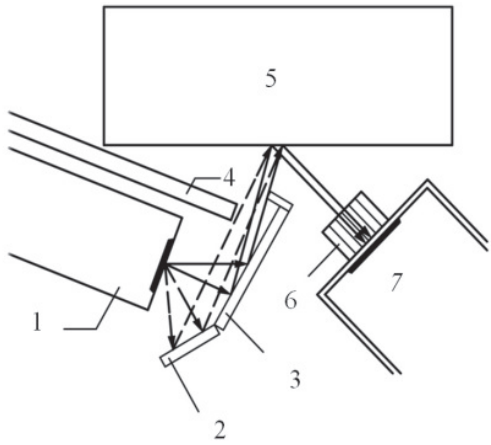

Figure 3.21: X-ray optical scheme with a complex secondary target: 1, X-ray tube; 2 and 3, secondary targets; 4, knife slit; 5, sample; 6, collimator; and 7, detector [47].

A shoot-through type tube with a silver anode 1 illuminates both parts of the secondary target, which is made of layers from different materials, such as KCl and Sc. The fluorescent radiation from both parts of the sec-

ondary target and the scattered spectrum of the tube pass through the knife slit (4) and hit the surface of the sample (5). The distance from the sample to the detector window is 5.3 mm. In the sample, we have scattering of secondary target lines, double scattering of the primary spectrum, and fluorescence radiation of sample atoms, and all of these pass through the collimator (6) and are simultaneously detected by the detector (7) as a single spectrum.

The collimation system allows the transmission of K-K_α radiation (λ = 3.74 Å) scattered by the sample in the range $2\theta = 106 \pm 5°$, and Sc-K_α (λ = 3.03 Å) in the range $2\theta = 116 \pm 5°$, which corresponds to the diffraction reflections of cementite in the following two ranges: d = 2.2÷2.4 Å and d = 1.69÷1.89 Å, respectively. In these ranges, there are intense Fe_3C reflections and no lines for the main phase of α-Fe with a bcc lattice. The residual γ-phase (austenite) produces an intense diffraction reflection with d = 1.8 Å, but has no reflections in the first range. Therefore, the appearance of the γ-Fe phase in the sample is easily controlled by the intensity ratio of the signals in these two ranges. A complex collimating system for the spectrometer, which was not previously used in XRF devices, makes it possible to reduce the distance "sample–detector window" to 5 mm without significant loss of the spectrum contrast. The minimum path through the air allows the light element lines to register without evacuation and to fill the working volume with inert gas.

An algorithm to determine the carbon in low-alloy steels using combined X-ray fluorescence and diffraction spectrum

Determining carbon using the amount of cementite is possible for low-alloy steels containing two main phases: α-Fe and cementite Fe_3C. Carbon's extremely low solubility in α-Fe (~ 0.002% mass) means that it is only present in the cementite [45]; therefore, its content C_C in the sample material can be determined from the quantity of cementite C_{Fe3C}: $C_C = 0.068 \cdot C_{Fe3C}$ (% mass). The conversion factor, 0.068, determines the amount of carbon in the Fe_3C molecule.

Let us now pay attention to the very high sensitivity of such a determination. Indeed, 1% change in the intensity of the cementite diffraction reflections, which is easily detected experimentally, corresponds to 0.068% change in the carbon content. Consequently, precision measurements of intensity may well provide an accurate carbon measurement of 0.01 to 0.02% mass, which is usual for modern methods. Using interplanar distances (d) of the main crystallographic phases, we determined the ranges where intense reflections of the phase of interest (Fe_3C) were present and there were no reflections of other phases (α-Fe). For the quasi-binary Fe_3C–α-Fe system, there are two such ranges: d = 2.2÷2.4 Å and d = 1.69÷1.89 Å. Furthermore, in order to obtain the given range, d, we used the Bragg equation to calculate the wavelength of the secondary target line, the angle of scattering of this line in the sample, and the angular divergence of the collimation device. These reflections should be located in those parts of the fluorescence spectrum where there are no analytical lines in the sample elements. Tuning is carried out by standards that show diffraction reflections near the edges of a given d range.

It should be noted that the possibilities of this method are not limited to the analysis of low-alloy steels. The spectrometer's secondary target and the collimation system can be tuned to the basic diffraction reflections of other phases of interest, which simultaneously allows the quantitative phase X-ray diffraction analysis and the X-ray fluorescence analysis of similar materials: ores, minerals, and other multiphase systems.

Conclusion to Chapter 3

The drawback of energy-dispersive spectrometers is their small dynamic range and low energy resolution. However, the high luminosity of the X-ray optical scheme makes it possible to use various methods for the fluorescence selective excitation of sample atoms. The fluorescence selective excitation schemes considered in this section allow us to minimize the detector's parasitic loading and to increase the contribution the "trace" impurity lines by one or two orders of magnitude. Due to this, it is possible to raise the sensitivity to a level of 10^{-4}% mass, which is the limit in the analysis of pure materials. A higher sensitivity can only be obtained for materials with a light matrix, where the spectrum does not contain high intensity lines. To expand the analytical range into the region of light elements, we have offered a complex analysis of the combined spectra of fluorescence, diffraction, and Compton scattering.

CHAPTER 4

DETERMINATION OF LIGHT IMPURITIES USING THE COMPTON AND RAYLEIGH SCATTERING INTENSITY RATIO

The fundamental limitation of the XRF method is connected with the impossibility of determining elements with a small atomic number ($Z < 6$). This limitation is due to the fact that the fluorescence yield reduces sharply with a decreasing atomic number and, consequently, the intensity of the analytical lines decreases. In addition, an increase in the wavelength leads to both a sharp increase ($\sim \lambda^3$) in the radiation absorption coefficient and a decrease in the depth t of radiation penetration into the sample material. For example, the penetration depth for C-$K\alpha$ radiation in steel is only 100 Å. With such a small information layer depth, special procedures for the sample surface preparation are required to ensure the adequacy of the analysis results. For the above reasons, the determination of elements with atomic numbers $Z < 6$ using the XRF method is only carried out in special cases. Measuring Compton scattering in the combined X-ray spectra can eliminate this fundamental limitation on the range of the detected chemical elements.

The use of the Compton effect to determine the concentration of light chemical elements in compounds and alloys is a very promising research area. Due to the large penetration depth of 0.1 to 1 mm for hard ($E \geq 17$ keV) X-ray radiation, the influence of material distorted surface layers on

the analysis results is sharply reduced. Thus, the sample preparation procedure is simplified. However, to ensure the necessary accuracy of scattering peak measurements, high-quality X-ray spectra with a low background level are required. Below, we will show that precision measurements of X-ray scattering intensities provide an extension to the range of tasks required when determining light elements.

The Compton effect is an experimental confirmation of the radiation quantum nature. In the classical paper [5], it was shown that the scattering of monochromatic X-ray radiation by matter is of a quantum nature. Two peaks are observed in the scattering spectrum: one has the wavelength of the incident radiation (coherent or Rayleigh scattering), and the second has a slightly larger wavelength (incoherent or Compton scattering). Subsequently, many theoretical and experimental studies were carried out on Compton scattering [7, 48, 49].

In this section, we will only consider those aspects of this complex problem that relate to the practical possibilities of analyzing the composition of a substance using Compton scattering.

Already two important facts have been established:

1) The wavelength distance $\Delta\lambda$ between the Compton and Rayleigh peaks does not depend on the atomic number Z of the substance by which the radiation is scattered, but it is determined by the scattering angle 2β [7, 48, 49]

$$\Delta\lambda = 0.02426\left(1-\cos 2\beta\right) \text{ (Å)}, \tag{4.1}$$

from which

$$2\beta = \arccos\left(1 - \frac{\Delta\lambda}{0.02426}\right);$$

2) The ratio of the Compton and Rayleigh peak intensities increases sharply with a decreasing atomic number Z, and also with an increase in the scattering angle.

Based on these regularities, Compton proposed a new method for determining light elements using the ratio of coherent and incoherent scattering peaks. This method has great promise for practical applications, since its sensitivity increases with a decreasing atomic number up to hydrogen (Z = 1). For several years after the discovery of Compton, the method was experimentally implemented in the study of gases and liquids [48]. However, it was impossible to apply it to the study of crystalline materials. According to Compton, this difficulty is related to the distortion of the scattering peaks intensity ratio due to the superimposition of Bragg reflections in the scatterer material.

Indeed, each substance is characterized by a set of reflections with a specific value of $1 / d_{hkl} = \sin\theta/\lambda$. One or more of these reflections can fall into the range $\sin\theta/\lambda$. As a result, an artifact arises, whose value depends on the scatter's structure. It is likely that it was not possible to obtain precision measurements for the ratio of the scattering peaks due to this reason.

In recent works [50–58], I_C/I_R measurements were used to obtain additional information on elements with an atomic number of Z < 11, particularly to correct the matrix effect when calculating concentrations of elements using the XRF method [55]. Such measurements do not require a precise determination of the peak profile or the careful removal of the continuous spectrum's background. Therefore, a standard XRF scheme is acceptable when a broadband primary spectrum has been used to excite fluorescence. In this case, the Rayleigh and Compton scattering peaks for the analytic line of the anode material were observed in the spectrum of the sample against a significant background of X-ray tube bremsstrahlung scattering. The presence of such a background complicates the ability to obtain precision measurements for the scattering peaks and limits the scope of the method.

4.1 Theory

4.1.1 Introduction and restrictions

The general theory of coherent and incoherent X-ray scattering is very complex and it is the basis for measurements in many areas of modern physics. Here, we restricted ourselves to the scattering of photons with energy lower than 25 keV. Such beams are used to obtain the spectra discussed in this work. This restriction simplifies the basic scattering formulas. Indeed, with the adopted limitation, the relative difference in the photon energies of coherent and incoherent scattering does not exceed a few percent. This means that the Klein-Nishina formulas for incoherent scattering on free electrons are transformed into a simple Thomson formula [55]. The absorption coefficients μ for both scattering components differ by no more than 10–12%, and this difference does not depend on the scatter's

atomic number. Thus, when analyzing the dependence of the intensity ratio on the atomic number, the difference in μ can be taken into account by a constant factor and does not require special consideration. The adopted limitation considerably simplifies the dependence of the scattering peaks intensity ratio on the atomic number of the scatterer material.

4.1.2 Scattering on a chaotic cluster of atoms

According to Pirenne's review [59], the total intensity scattered by an isolated atom for unpolarized primary radiation is

$$I_S = I_0 \frac{a_e^2}{R^2} \frac{1+\cos^2 2\beta}{2} \underbrace{\left[\; f^2 \; \right]}_{coherent} + \underbrace{\left[\; QZS \; \right]}_{incoherent}, \tag{4.2}$$

where, according to Heisenberg-Bewilogua, $Q = \left(1 + \frac{h\left(1-\cos 2\beta\right)}{mc\lambda}\right)^{-3}$ is the relative correction factor for incoherent radiation, h is the Plank's constant, m is the mass of an electron at rest, λ is the wavelength in Å, I_0 is the primary beam intensity, a_e is the classical radius of an electron, 2β is the scattering angle, f is the atomic scattering factor for X-rays, Z is the atomic number, and S is the incoherent scattering function [59, 60].

In formula (4.2), the expression in brackets determines both coherent and incoherent scattering. The function $S = S(\upsilon)$ depends on the chosen model of the electron distribution in the atom: $\upsilon = 2.21\left(\frac{\sin\beta}{\lambda}\right) \Big/ Z^{2/3}$ with λ in Å. Heisenberg obtained a formula for calculating $S(\upsilon)$, and Bewilogua

compiled a numerical table of S values as a function of υ [59]. Using Table 4.1, we can calculate the Compton scattering intensity for any atom. For convenience, the data provided in Table 4.1 in the range of $0.2 < \upsilon < 1$ can be approximated by a polynomial with an error of less than 0.32%:

$$S(\upsilon) = 0.8367\upsilon^3 - 2.074\upsilon^2 + 1.812\upsilon + 0.3911.$$

Let us now define the range of values of the atomic number Z, which is covered by this formula for different values $\left(\frac{\sin\beta}{\lambda}\right)$ of scattered radiation in Table 4.2.

Table 4.1: A numerical table of *S* values as a function of υ

υ	S(υ)	υ	S(υ)	υ	S(υ)	υ	S(υ)
0.05	0.319	0.3	0.776	0.6	0.909	0.9	0.954
0.1	0.486	0.4	0.839	0.7	0.929	1.0	0.963
0.2	0.674	0.5	0.880	0.8	0.944		

We must pay attention to contradictory trends. The increase in $\left(\frac{\sin\beta}{\lambda}\right)$ improves the separation of the Compton and Rayleigh scattering peaks and reduces the intensity of Bragg reflections, which can be superimposed on the scattering peaks. However, we can also observe that increasing the Z_{min} of the chemical element allows us to use the Heisenberg formula.

Table 4.2: The range (Z_{min}, Z_{max}) of analyzed elements and the relative difference between Compton and Rayleigh wavelengths for different scattering angles and for probing radiation

λ, Å	2β, deg	$\frac{\sin\beta}{\lambda}$	$\frac{\Delta\lambda}{\lambda}$	Z_{min}	Z_{max}
0.709	100	1.08	0.0402	3.7	41.2
	135	1.303	0.0584	4.9	54.6
0.559	100	1.370	0.0509	5.3	58.9
	135	1.653	0.0741	7.0	78.1

Now, we will consider scattering by a cluster of atoms. For a random aggregation of different types of atoms, which give an additive contribution to the scattering, we can write down the formula for the ratio of the Compton and Rayleigh scattering intensities as follows:

$$\frac{I_C}{I_R} = Q\frac{\sum_{i=1}^{m} n_i Z_i S_i}{\sum_{i=1}^{m} n_i f_i^2} \tag{4.3}$$

where n_i is the number of atoms of the i-th type, and m is the number of types of atoms in the cluster. We note that, because of the nonlinear dependence of S on the atomic number [59], it is impossible to apply the concept of the average atomic number for the cluster of atoms in the calculations.

4.1.3 Scattering on molecules

Certain difficulties arise in the analysis of the materials that are multi-component systems. Such materials include ores, coal, and alloy steels. The effect of correlation in the arrangement of atoms, such as in the formation of molecules, manifests as oscillations on the diffraction curves at $\frac{\sin\beta}{\lambda} < 0.6$ [6]. The result is shape distortions of the Compton and Rayleigh scattering peaks, which makes calculations difficult. This influence can be avoided by measuring the spectra in the angle β range with $\frac{\sin\beta}{\lambda} \geq 0.6$ where the correlation effect is absent.

Then for the cluster of molecules, by analogy with (4.3), we can write

$$\frac{I_C}{I_R} = Q\frac{\sum_{j=1}^{q} N_j \sum_{i=1}^{p_j} n_{ji} Z_i S_i}{\sum_{j=1}^{q} N_j \sum_{i=1}^{p_j} n_{ji} f_i^2} \tag{4.4}$$

where q is the number of types of molecules; N_j is the number of j-type molecules; and p_j is the number of atoms in the j-type molecule. Taking into account $N_j \sim \frac{W_j}{M_j}$, where W_j is mass fraction of j-type molecules and M_j is the molecular mass, we can write (4.4) in the following form [57]:

$$\frac{I_C}{I_R} = Q \frac{\sum_{j=1}^{q} W_j / M_j \sum_{i=1}^{p_j} n_{ji} Z_i S_i}{\sum_{j=1}^{q} W_j / M_j \sum_{i=1}^{p_j} n_{ji} f_i^2} \tag{4.5}$$

This formula establishes the relationship between the ratio of the intensities of the scattering peaks and the mass fractions of the molecules included in the multi-component material.

4.1.4 Scattering by materials with inhomogeneous depth distribution of impurities

Inhomogeneous depth distribution of impurities is typical for materials subjected to surface treatment: coating, ion implantation, radiation, etc. Usually, to determine the characteristics of such a distribution, very complex methods are used, which are associated with the destruction of the sample [61–63]. In this section, we will provide a theoretical justification for a non-destructive method of analyzing the depth distribution of impurities.

This method is based on measuring the intensity ratio of the Compton and Rayleigh scattering peaks at different angles of X-ray emission from the sample surface. If, at the selected scattering angle 2β (Fig. 4.1), the incidence φ and exit ψ angles are varied by rotating the sample then the depth of the informative layer can be significantly changed. Measuring the ratio of the scattering peaks allows us to determine the average impurity content for each depth of the informative layer. With an inhomogeneous distribution of impurities, the average value depends on the depth; so, the ratio of the peaks should change.

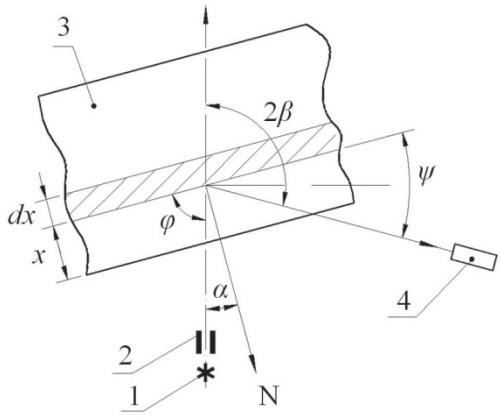

Fig. 4.1: Schematic ray path of monochromatic radiation scattered by a sample that has an inhomogeneous depth distribution of impurities. N represents what is normal in the sample's surface; 2β is the scattering angle; φ and ψ are the incident and exit angles of the beam: 1, radiation source; 2, collimator; 3, sample on the goniometer; and 4, crystal-diffraction spectrometer unit.

Let us consider the attenuation of the intensity I of the monochromatic radiation incident at an angle φ to the surface of the sample with an inhomogeneous composition. The scattered radiation is observed at the angle 2β (Fig. 4.1). On the surface we set $x = 0$ and $I = I_0$. The intensity at the depth x is denoted by I_x. Then the decrease in the intensity dI_x on the path from x to $x + dx$ is [49]:

$$dI_x / I_x = -\mu(x)\left(\sin^{-1}\varphi\right)dx \quad , \tag{4.6}$$

where μ (x) is the linear attenuation coefficient whose value varies with depth x in connection with the change in sample composition.

The intensity at depth x can be calculated by integrating (4.6) over x from 0 to x:

$$\ln I_x\big|_0^x = -\sin^{-1}\varphi\int_0^x \mu(x)dx \tag{4.7}$$

$$I_x / I_0 = \exp\left(-\sin^{-1}\varphi\int_0^x \mu(x)dx\right) \tag{4.8}$$

Thus at $\mu(x)$ = const., the intensity at the depth x is determined by the value $I_0\exp(-\mu x/\sin\varphi)$ [49], while with a varying $\mu(x)$ it is determined by the formula (4.8). Taking this fact into account, the intensity of the radiation scattered by the dx layer is written as

$$dI_x^{Sc} \sim \sigma(x,2\beta)\exp\left(-\int_0^x \mu(t)\left(\frac{1}{\sin\varphi}+\frac{1}{\sin\psi}\right)dt\right)dx, \tag{4.9}$$

where t is the integration variable, and $\sigma(x, 2\beta)$ is the linear scattering coefficient. Here, $\sin^{-1}\psi$ takes into account the absorption of the outgoing radiation [49]. Thus, the intensity of scattering by the dx layer is determined by the scattering coefficient $\sigma(x, 2\beta)$ and by the value of the upper integration limit of x.

The scattered radiation contains coherent (Rayleigh) and incoherent (Compton) components:

$$\sigma(x,2\beta) = \sigma_R(x,2\beta) + \sigma_C(x,2\beta). \tag{4.10}$$

We are interested in the ratio of their intensities. In formula (4.9) and further calculations, we neglected the difference between the linear attenuation coefficients for Rayleigh μ_R and Compton μ_C scattering.

It is easy to show that this difference can be taken into account by the factor $\left(1+\frac{\sin\varphi}{\sin\psi}\right)\Big/\left(1+\frac{\mu_C}{\mu_R}\frac{\sin\varphi}{\sin\psi}\right)$ in the ratio of the intensities of the Compton and Rayleigh peaks. Such a factor does not depend on the atomic number of the scatter material and therefore does not affect the dependence I_C/I_R on *Z*.

In accordance with [59] and taking into account the foregoing, the intensity of Compton scattering by an inhomogeneous layer is as follows:

$$I_C(\varphi,\psi)=\sum_j Z_j\ S(v_j)\int_0^\infty C_j(x)\exp\left(-\int_0^x \mu(t)\left(\sin^{-1}\varphi+\sin^{-1}\psi\right)dt\right)dx \quad . (4.11)$$

Similarly for the Rayleigh scattering, it is

$$I_R(\varphi,\psi)=\sum_j f_j^{\,2}\int_0^\infty C_j(x)\exp\left(-\int_0^x \mu(t)\left(\sin^{-1}\varphi+\sin^{-1}\psi\right)dt\right)dx \quad . (4.12)$$

where $C_j(x)$ is the distribution of the atomic concentration of the element *j* over the depth *x*; f_j is the atomic scattering factor for X-rays; *Z* is the atomic number; and *S(v)* is the incoherent scattering function according to Hei-

senberg-Bewilogua [59]: $v = 2.21\left(\frac{\sin\theta}{\lambda}\right)\Big/ Z^{2/3}$, with λ in Å. The integral in the exponent determines the depth of X-ray penetration into the sample, and, consequently, the depth of the averaging layer of the function $C(x)$.

At a constant scattering angle 2β, as seen in Figure 4.1 it follows that $\varphi = \pi/2 - \alpha$; $\psi = 2\beta - \pi/2 - \alpha$.

Relations (4.11) and (4.12) depend on the single parameter α and are inhomogeneous Fredholm equations of the first kind:

$$g(\alpha) = \int_a^b K(\alpha, x) C(x) dx \quad . \tag{4.13}$$

The problem is finding the functions $C(x)$ from experimental values of $g(\alpha)$ for a given kernel function $K(\alpha, x) = \exp\left(-\int_0^x \mu(t)(\sin^{-1}\varphi + \sin^{-1}\psi)dt\right)$. However, in the case under consideration, the kernel of the integral operator depends on the concentration distribution, since the linear coefficient of attenuation depends on the function $W(t)$:

$$\mu(t) = \sum_j W_j(t)(\mu/\rho)_j \Big/ \sum_j W_j(t)/\rho_j$$

where $(\mu/\rho)_j$ is the mass attenuation coefficient of the probe radiation by the element j; $W(t)$ is the weight concentration; and

$(\rho(x))^{-1} = \sum_j W_j(t)/\rho_j$ determines the sample density ρ (x) [49]. Therefore, equations (4.11) and (4.12) can only be solved by numerically fitting the coefficients for a given analytic form of the profile C (x). In the absence of interaction of layers, the distribution function is used in the following form:

$$C = C_0 \exp\left(-(x/x_0)^{2n}\right), \tag{4.14}$$

where C_0 is the atomic fraction, x_0 is the characteristic thickness of the layer, and n determines the sharpness of the interface.

Consider a binary system A-B in which the atomic concentration of the component A varies with depth according to the law C (x), the concentration of the component B is 1– C (x). Then from (4.11) and (4.12),

$$\frac{I_C}{I_R} = \frac{Z_B S(v_B) + (Z_A S(v_A) - Z_B S(v_B))\,\Phi(\alpha)}{f_B^2 + \left(f_A^2 - f_B^2\right)\Phi(\alpha)}, \tag{4.15}$$

where

$$\Phi(\alpha) = \frac{\int_0^\infty C(x)\exp\left(-\left(\sin^{-1}\varphi + \sin^{-1}\psi\right)\int_0^x \mu(t)dt\right)dx}{\int_0^\infty \exp\left(-\left(\sin^{-1}\varphi + \sin^{-1}\psi\right)\int_0^x \mu(t)dt\right)dx},$$

$$\mu(t) = \frac{(\mu/\rho)_B + W_A(t)\left((\mu/\rho)_A - (\mu/\rho)_B\right)}{W_A/\rho_A + (1-W_A)/\rho_B}.$$

The kernel of the integral operator in the physical sense determines the radiation penetration depth d. The values of the integrals depend on the relationship between the characteristic scale of the change in the function $C(x)$ and the depth of penetration. If we define d as the thickness of the layer, which gives 90% of the contribution to the scattering [49], we obtain:

$$d = \frac{2.3}{\mu} \times \left(\sin^{-1} \varphi + \sin^{-1} \psi \right)^{-1} \tag{4.16}$$

It is seen that a variation in the exit angle ψ from 1 to 15º gives a 30-fold increase in the penetration depth. We note that the use of the probing radiation with different wavelengths allows for further expanding the range d because $\mu \sim \lambda^{2.7}$. As a result, varying the λ and the radiation exit angle makes it possible to change the penetration depth by three to four orders of magnitude. According to our estimations, this allows for expanding the range of the layer thicknesses from 100 Å to 1 mm.

It follows from formula (4.16) that, in order to obtain information from the thinnest layers, it is necessary to make measurements at very small values of $\psi \sim 1$ °. However, the determination of the zero angle (the origin) using a goniometric device is rather difficult due to the significant angular divergence of the collimator in the primary beam (Fig. 4.1). In order to determine the origin, it is convenient to use the dependence of the total scattering intensity on the entrance and exit angles. In our notation, this dependence has the following form:

$$I(\alpha) \sim \frac{\sigma}{\mu} \left(\cos^{-1} \alpha + \sin^{-1} \left(2\beta - \pi/2 - \alpha \right) \right)^{-1} . \tag{4.17}$$

Taking into account $\cos\alpha \approx 1$, and $\sin\left(2\beta - \pi/2 - \alpha\right) \approx \psi$ at small $\psi << 1$, we obtain a linear dependence of $I(\alpha)$ and can determine the origin of the α angles. Thus, to implement the method, it is necessary to measure experimentally the ratio I_C / I_R depending on the α angle. Then, by varying the parameters of the formula (4.14), the fitting of the relation (4.15) to the experimental ratios I_C / I_R is carried out.

4.2 Specificity of measuring the incoherent scattering intensity

In this section, we consider measurements of the Rayleigh and Compton scattering peak intensities for the primary beam photon energy less than 25 keV. The beams of such photons can be obtained in the equipment for XRD and XRF analyses, and for them the simplified theory described in Section 4.1 is applicable. However, the use of beams with low photon energy (less than 25 keV) makes it difficult to measure the intensity of the scattering peaks due to the overlay of the broadband scattering background of the continuous spectrum and the diffraction reflections of the sample material on the peaks of Rayleigh and Compton scattering. Therefore, standard XRD and XRF schemes are not suitable, and special measures are required for the formation of a monochromatic primary beam and the registration of the scattered radiation. Even with the monochromatic primary beam, it is not always possible to avoid the imposition of diffraction reflections on the scattering peaks. The contribution of these reflections to the intensity of the scattering peaks can be reduced by several orders of magnitude due to increasing the $\frac{\sin\beta}{\lambda}$ ratio and choosing the scattering angle and angular divergence. Obviously, both the scattering angle 2β and

the angular divergence range $\Delta\beta$ of the X-ray optical scheme should be chosen so that within this range the Bragg condition $\frac{1}{d_{hkl}} = \frac{\sin(\beta \pm \Delta\beta)}{\lambda}$ does not hold for any type of crystallographic planes d_{hkl} in the material under study. In addition, for all amorphous materials and a significant amount of polycrystals, the intensity of Bragg reflections at $\frac{\sin\beta}{\lambda} \geq 1.2$ Å^{-1} is extremely low, and they cannot noticeably distort the scattering peaks via superposition. These conditions make it possible to formulate specific requirements for X-ray optical schemes.

4.2.1 X-ray optical schemes to measure the scattering peaks

The basic requirements for X-ray optical schemes for measuring scattering peaks are as follows:

1. Monochromatization of the primary photon beam with energy of ≤ 25 keV at a large scattering angle in order to satisfy the condition of $\sin\beta/\lambda > 1.2$ Å.
2. The ability to change the scattering angle and the angular divergence of the scattered radiation.

Taking into account these requirements, we developed X-ray optical schemes to measure scattered radiation using crystal-diffraction (Fig. 4.2) and energy-dispersive (Fig. 4.3) spectrometers.

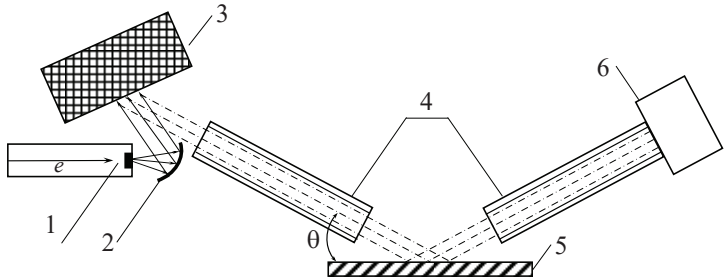

Figure 4.2: Scheme for measurement of scattered radiation using a crystal-diffraction spectrometer [64]: 1, X-ray tube with a silver anode; 2, secondary target; 3, sample; 4, Soller collimators; 5, crystal-analyzer; and 6, detector.

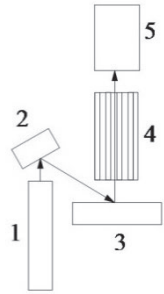

Figure 4.3: Scheme for measuring scattered radiation using an energy-diffraction spectrometer: 1, X-ray tube; 2, secondary target; 3, sample; 4, collimator; and 5, detector.

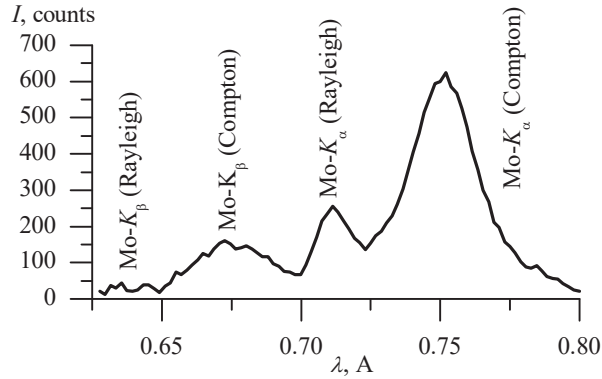

Figure 4.4: A fragment of the scattering spectrum from amorphous carbon measured using a crystal-diffraction spectrometer. The secondary target is molybdenum and the scattering angle is 130°.

In the scheme shown in Figure 4.2, an X-ray tube with a silver anode (pos. 1) illuminates a secondary target with a curved surface (pos. 2). The secondary target is made of pure molybdenum (or niobium) and is located 2–3 mm from the tube anode. The investigated sample (pos. 3) is located at a distance of 7 mm from the secondary target. The radiation scattered by the sample is registered by a crystal-diffraction spectrometer with two Soller collimators, which are discussed in Section 2.3. The scattering angle 2β is varied from 110° to 130°, $\Delta 2\beta \approx 15°$.

The half-width of the Rayleigh peak $\Delta\lambda \leq 1.7 \cdot 10^{-2}$ Å is sufficient to observe the scattering peaks separately (Fig. 4.4).

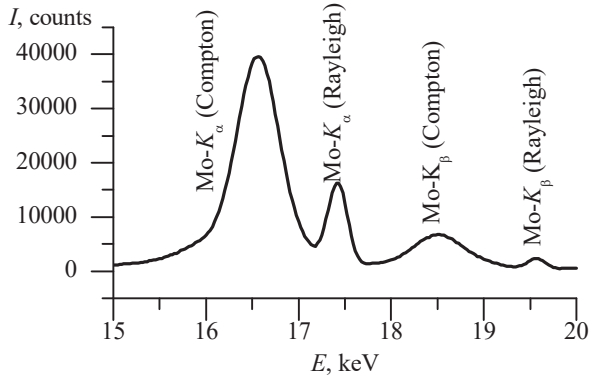

Figure 4.5: A fragment of the scattering spectrum from amorphous carbon measured using an energy-dispersive spectrometer. The econdary target is molybdenum. The scattering angle is 135°, the SDD detector is Amptek X-100, and the accumulation time is 300 s.

In the scheme with an energy dispersive spectrometer, we managed to achieve a large scattering angle of 2β =135° and to reduce the angular divergence to $\Delta 2\beta$ = 10°. This provided a high-quality separation of the scattering peaks (Fig. 4.5), which is necessary to ascertain precision measurements of their intensity. Both schemes provide a high contrast in the scattering spectra, make it possible to reliably separate the peaks, and even to analyze the asymmetry of the Compton band shape, which is predicted by the theory.

4.3 Possibilities of these developed schemes to determine light elements using the scattering peaks' ratio

The Fe-Fe_3C system, which includes low-alloy steels and cast irons, was chosen as the test object. The experimental calibration plot (Fig. 4.6) for determining the carbon content in steel using the Compton and Rayleigh

peaks integral intensities ration $X = \frac{I_C}{I_R}$ is characterized by a concentration sensitivity of $\frac{1}{X}\frac{\partial X}{\partial C} = 1.83\frac{\%}{\text{mass}\%}$ and a standard deviation of 0.03% mass. In principle, this method can be applied for rapid analysis of the carbon content in steel.

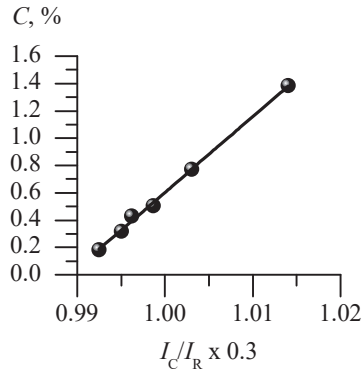

Figure 4.6: Calibration plot for the Compton-to-Rayleigh scattering integrated intensity ratio in low-alloyed steels. The accumulation time is 600 s.

However, one of this method's drawbacks is the need to introduce corrections based on the contribution of other light elements to the ratio of the peaks' integrated intensities. If the difference in the content of other light elements in the samples reaches ~ 1% mass, then their effect leads to a marked increase in the dispersion of the calibration function. Figure 4.7 demonstrates that, for standard cast iron samples with differing silicon concentrations of more than 1% and phosphorus concentrations of 0.7%, the introduction of the correction significantly reduces the dispersion of

the calibration function: i.e., increases the accuracy of carbon measurements.

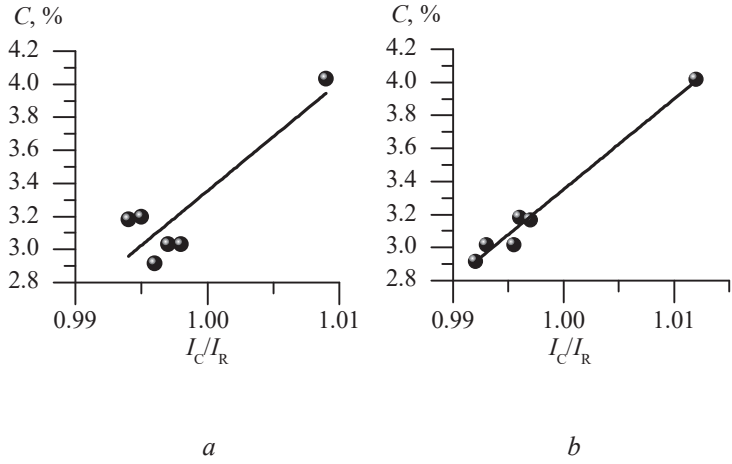

Figure 4.7: Reduction of the dispersion in the calibration function after taking into account the influence of other elements on the Compton and Rayleigh peaks' ratio: *a*, without correction; and *b*, with corrections for Si, P, and S.

Making a correction based on the influence of other light elements provides the possibility of determining the carbon content in multi-component systems, if the variation in the concentration of these light elements does not exceed a few percent.

Let us estimate the possibility of using the scattering method to analyze other light impurities in metals (see Table. 4.3). As follows from the data of the table, the concentration sensitivity of the measurements increases noticeably with a decreasing atomic number. This is particularly pronounced in metal-hydrogen systems, where a detection limit of $10^{-4} \div 10^{-3}$% mass can be reached.

Table 4.3: Calculated values for the concentration sensitivity $\frac{1}{X}\frac{\partial X}{\partial C}, \frac{\%}{\%\ \text{mass}}$ when measuring light impurities in metals using Compton-to-Rayleigh integrated intensity ratios.

		Ti	Fe	Ni	Zr	Nb	Ag	W
	Z	22	26	28	40	41	47	74
H	1	16.52	20.70	22.30	125.25	153.9	–	–
He	2	3.63	3.95	4.02	5.68	5.74	6.50	11.66
Li	3	2.47	2.66	2.70	3.64	3.67	4.05	6.18
Be	4	2.16	2.32	2.36	3.15	3.18	3.49	5.14
B	5	1.96	2.12	2.16	2.89	2.92	3.20	4.64
C	6	1.89	2.05	2.09	2.83	2.85	3.13	4.51
N	7	1,70	1.85	1.90	2.58	2.60	2.86	4.09
O	8	1.55	1.70	1.75	2.40	2.42	2.65	3.78

The experimental verification of this position was performed with standard samples of the titanium-hydrogen binary system (Fig. 4.8). The obtained concentration sensitivity of 170 turned out to be even higher than the calculated values, although the reason for this result has not yet been clarified.

The high sensitivity of determining light elements using the intensity ratio of the Compton and Rayleigh scattering peaks can serve as a basis for developing express methods for the non-destructive testing of materials subjected to surface processing: coating, ion implantation, irradiation, etc.

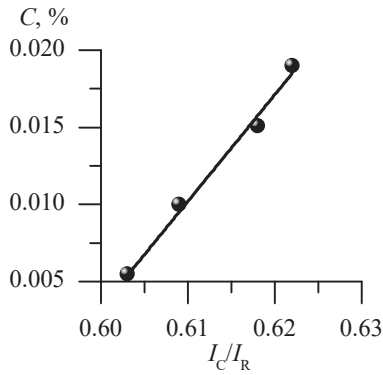

Figure 4.8: The calibration plot to determine hydrogen in the Ti-H system by the Compton-to-Rayleigh scattering peak ratio

4.4 Reducing the intensity of Bragg reflections due to the temperature

With precise measurements of the scattering peaks, it is not always possible to avoid the superposition of Bragg reflections (with large Miller indices) on the scattering peaks, even if the scattering angle and the angular divergence of the beam are chosen correctly. It is worth noting that the intensity of these reflections is significantly reduced due to the influence of the Debye-Waller temperature factor [6] and the static distortion factor [65].

Both of these factors reduce the intensity of Bragg reflections when increasing $\frac{\sin\beta}{\lambda}$ by the same law:

$$I \cong I_0 \exp(-2M),$$

$$2M = (g(u_T) + g(u_S))\frac{\sin^2\beta}{\lambda^2}$$

where .

The value of $g(u_T)$ depends on the root-mean-square temperature displacements of atoms, and $g(u_S)$ on the static displacements caused by micro-strains. By increasing the sample temperature or introducing the micro-strains through an external action, one can significantly reduce the intensity of Bragg reflections for large $\frac{\sin\beta}{\lambda}$ values.

In this section, we consider the effect of the sample temperature and micro-strains on the intensity of Bragg reflections under the experimental conditions $\sin\beta/\lambda = 1.2 \div 1.65$ Å^{-1} for measuring the scattering.

The temperature factor $\exp(-2M)$ can be calculated from the Debye characteristic temperature θ_D [6] in the following form:

$$M = \frac{6h^2T}{mk\theta_D^2}\cdot\left[\Phi(x) + \frac{x}{4}\right]\cdot\frac{\sin^2\beta}{\lambda^2}, \tag{4.18}$$

where h and k are Plank and Boltzmann constants, respectively; $m = A\cdot 1.66\cdot 10^{-27}$kg is the atomic mass; and $x = \theta_D / T$; 2β is the scattering angle.

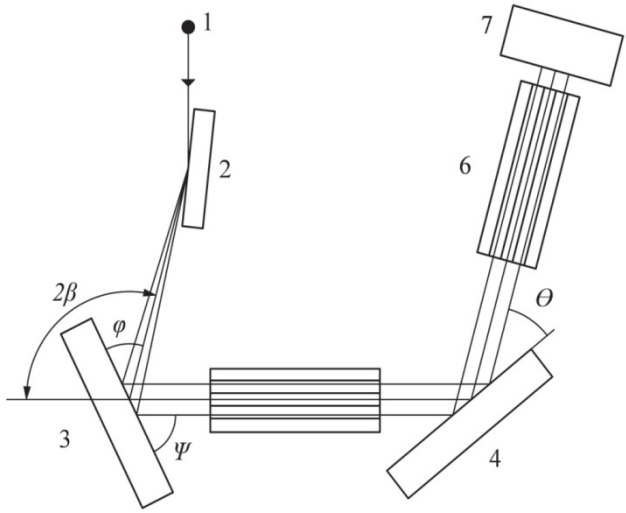

Figure 4.9: Scheme for measuring X-ray scattering in the range of sinβ/λ from 1.2 to 1.65 Å^{-1}: *1*, X-ray source; *2*, monochromator (graphite [002]); *3*, sample; *4*, crystal-analyzer LiF (002); *5* and *6*, Soller collimators; and *7*, detector

In accordance with (4.18), Bragg reflections are more pronounced for materials with larger atomic masses and Debye temperatures. To establish the quantitative criterion for the absence of superposition of the Bragg reflections on the scattering peaks, we carried out temperature X-ray measurements for a number of one-component materials and binary chemical compounds. For the study, we selected one-component materials with atomic number Z from 12 (Mg) to 74 (W), as well as binary chemical compounds. The crystal lattices of all the selected samples belong to the classes with the highest symmetry, as well as mainly face-centered and body-centered cubic systems. Lattices with high symmetry give, as is known, the greatest intensity of Bragg reflections. The X-ray measurements were performed in the radiation of a silver anode at a voltage of 43

kV in the sinβ/λ range from 1.2 to 1.65 Å^{-1}. The sample was placed in a vacuum chamber mounted in the X-ray diffractometer. An autonomous unit of hetero-ion pumping provided a vacuum of 10^{-7} Torr within the chamber in the temperature range from 0 to 800°C. The measurement scheme is shown in Figure 4.9.

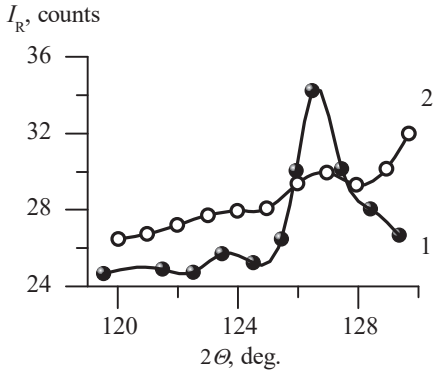

Figure 4.10: Influence of the temperature factor on the detectability of Bragg reflections in the range of $\frac{\sin\beta}{\lambda}$ from 1.2 to 1.65 Å^{-1} at T = 300K for crystalline materials with an fcc lattice: (*1*) copper, $2M = 2.93$, and (*2*) aluminum, $2M = 4.64$.

Three scanning modes were implemented: (1) θ–2θ scanning of an analyzer crystal at a constant scattering angle; (2) 2β scanning of the source, while the analyzer is tuned to the Rayleigh peak; and (3) 2β scanning of the source with sequential θ–2θ displacement of the analyzer crystal tuned to the Compton peak.

In the first mode, the Rayleigh and Compton peaks are separated; thus, it is possible to carry out separate tuning for each peak. The second and third scanning modes were used to select the 2β scattering angle range where no

diffraction reflections were observed for the sample under study in the $\frac{\sin\beta}{\lambda}$ range from 1.2 to 1.65 $Å^{-1}$.

The measurements at room temperature made it possible to establish that, for polycrystalline materials with the highest symmetry lattices (fcc and bcc), the Bragg reflections in the $\sin\beta / \lambda$ range from 1.2 to 1.65 $Å^{-1}$ are observed for tungsten ($2M_T$ = 1.08), molybdenum ($2M_T$ = 2.93), but are not detected for aluminum ($2M_T$ = 4.64) and magnesium ($2M_T$ = 7.65), (Fig. 4.10). Thus, in order to completely eliminate the influence of Bragg reflections with the used measurement geometry, the value of $2M$ must be increased to at least 4.6.

For quantitative testing of the $2M$ value, a direct experiment was carried out to measure the intensity of an α-Fe (bcc) Bragg reflection at various temperatures. The range of the temperature change was chosen so that no change in the sample structure occurred when heating in a high vacuum.

For the chosen (844) reflection, d = 0.3056Å, $\frac{\sin\beta}{\lambda}$ = 1.65 $Å^{-1}$. The measurement results are presented in Figure 4.11.

As it is seen from the figure, the Bragg reflection intensity decreases in accordance with the law exp (–$2M$) as the temperature increases. Indeed, with an increase in temperature from 300 K to 510 K and then to 660 K, the value of $2M$ increases, respectively, from 1.84 to 3.13 and to 4.05. Accordingly, the calculated intensity of the Bragg reflection decreases from

0.159 to 0.044 and to 0.017, which agrees with the experimentally observed decay of the Bragg reflection temperature in Figure 4.11.

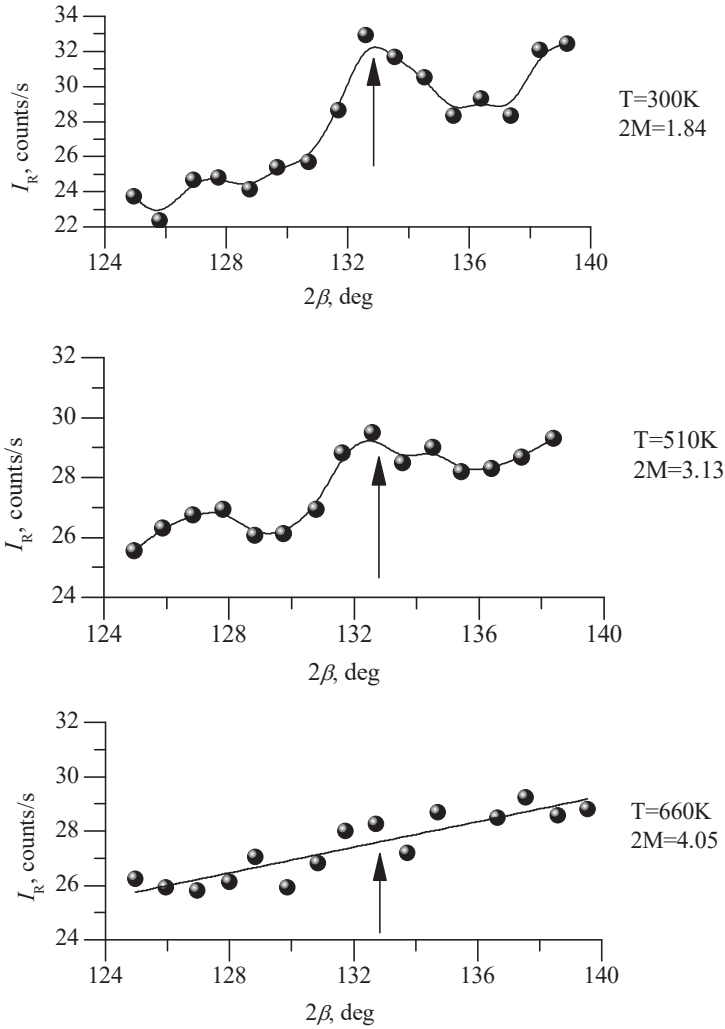

Figure 4.11: Fragments of the α-Fe scattering spectra measured at different temperatures. The arrow indicates the Bragg reflection (844), $2\beta = 132.8°$ [64].

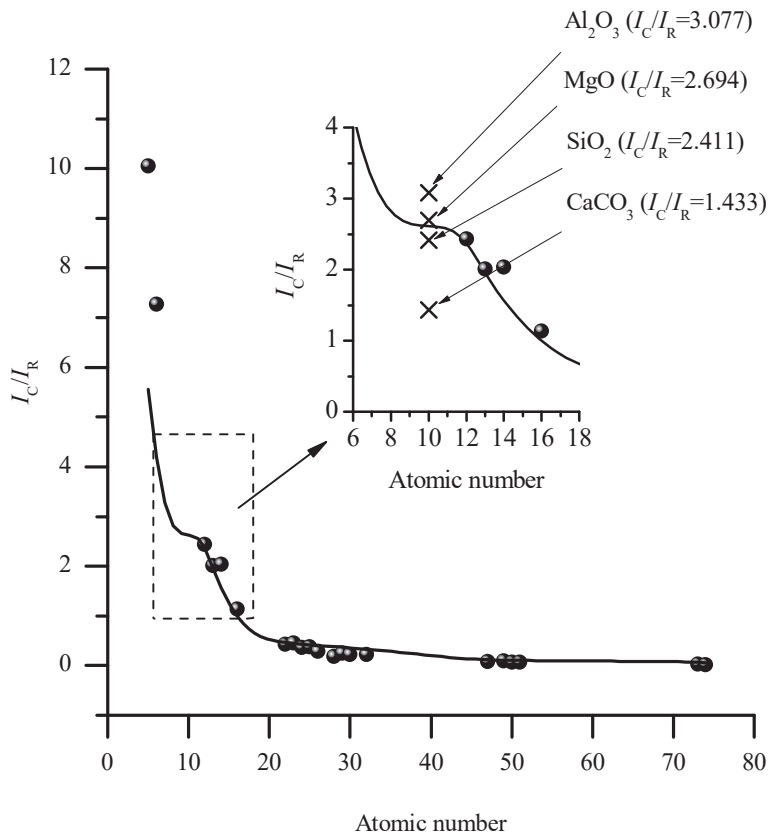

Figure 4.12: The experimental dependence of the scattering peaks ratio on the atomic number of the scatterer material. An EDXRF type spectrometer ($2\beta = 135°$) and the accumulation time for each spectrum is 300 s.

A similar attenuation of Bragg reflections is also observed due to the static distortion factor: exp ($-2M_S$). However, due to the impossibility of calculating the magnitude of static displacements in atoms under mechanical action, we could not establish quantitative relationships between the im-

pact parameters and the attenuation of the Bragg reflections. The value of M_S is added to the temperature component of M_T, which leads to an additional extinction of Bragg reflections and a decrease in their contribution to the intensity of scattering peaks.

Thus, the imposition of the material's Bragg reflections onto scattering peaks is, as Compton foresaw, a serious factor when measuring the ratio of the Compton and Rayleigh scattering intensity. In most works, this was not taken into account, and no methodological measures were taken to reduce its influence on the results. Probably for this reason, all the experimental measurements on the ratios of the scattering peaks did not have high reproducibility and were only used for semi-quantitative estimates, such as when studying the effect of the light element matrix on XRF results. Due to the spread of experimental data, it was not possible to precisely obtain the dependence of the peaks' ratio on the scatterer's atomic number.

The proposed criteria for selecting the measurement conditions (sin β/λ, divergence $\Delta\beta$ angular range and $2M$ value in the temperature factor) and the developed X-ray optical schemes in which these conditions are realized, allowed for the experimental dependence of the ratio of scattering peaks on the atomic number of the scatterer material (Fig. 4.12) for polycrystalline materials with a different type of crystal lattice. This dependence decreases monotonically with an increase in the atomic number and does not contain the spikes associated with the different superposition conditions for the Bragg reflections on the scattering peaks. The ratio of the scattering peaks does not depend on the same material's structural state. We now want to draw the reader's attention to the experimentally

observed difference in the I_C/I_R ratio for chemical compounds with the same average atomic number. This result casts doubt on the well-known approach of the "average atomic number". Thus, the artifact associated with the imposition of Bragg reflections on the scattering peaks has been virtually eliminated. The completed designs are applied to solve some specific problems (see Chapter 5).

4.5 Displacement of the Compton band in scattering by bound electrons

In conclusion, we consider a very interesting result, which was obtained with the help of the developed X-ray optical schemes. The main contribution of bound electrons to the Compton effect is provided by electrons that have outer shells with a characteristic binding energy of ≤ 100 eV [49]. It is these shells that undergo changes under doping, and one should expect an increase in the binding energy when forming thermodynamically stable solid solutions and compounds. In the description of the scattering by bound electrons, the Compton formula for free electrons is corrected in accordance with Bloch theory [49]. This correction is proportional to the square of the wavelength, λ^2. Therefore, to detect its effect, it is advisable to use radiation with the longest wavelength, λ, where the precision registration of the Compton profile is still possible, since the Compton peak intensity decreases sharply with increasing wavelengths.

The use of a high-aperture X-ray optical scheme (Fig. 4.2) for precision measurements of the Compton peak in soft radiation of Nb-K_α (16.6 keV) made it possible to reveal experimentally the Compton peak shift with increasing carbon content in steel. Experimental studies were carried out

on the State Standard Samples (SSS) of low-alloyed carbon steel (series 154) with a carbon content of 0.03 to 1.1% mass (Table 4.4).

Table 4.4: Positions λ_{max} (Å) of the Compton peak maximum and its energy displacement, ΔE (eV), for standard samples of low-alloyed steels (series 154) with different carbon contents, C (% mass) [66].

Sample number	*C*, %mass	λ_{max}, Å	ΔE, eV
154-4	0.03	0.7900	0
154-1	0.42	0.7885	30
154-2	0.82	0.7882	36
154-7	1.1	0.7865	70

For all the samples studied, the position and half-width of the Rayleigh peak from Nb-K_α were practically the same, being, respectively, $\lambda = 0.748$ Å and $\Delta\lambda = 0.015$ Å. The half-width of the Compton peak remained in the range of $\Delta\lambda = 0.027 \div 0.029$ Å (Fig. 4.13), and it was impossible to detect any regular change with an increasing carbon content. Nevertheless, the displacement of the Compton peak position toward smaller wavelengths has been revealed (Fig. 4.13), which changes monotonically with an increasing carbon content in steel (Table 4.4).

Taking the position of the Compton peak for the sample with the minimum carbon content as the origin, we calculated the displacement of this peak for the steel samples with different carbon contents in energy units (Table 4.4). It turned out that the maximum displacement (about 70 eV) is close to the binding energies of the outer subshells M_1, M_2, and M_3 of the

free iron atom, which were 98, 61, and 59 eV, respectively. Only the electrons of these subshells give the main contribution to the Compton scattering, while the contribution of the next L_3 shell with a binding energy of 713 eV does not exceed 1 % by our estimation. The introduction of carbon into iron leads to the formation of an entire complex of thermodynamically stable solid solutions and phases with a corresponding increase in the binding energy of electrons in the iron atom outer shells. Apparently, this increase is manifested in the Compton peak displacement that we observed.

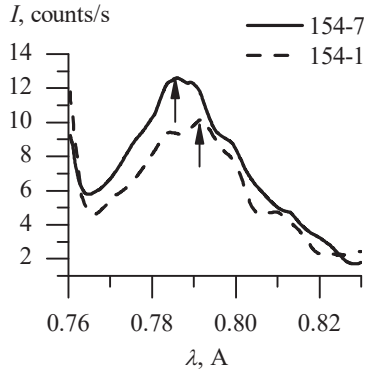

Figure 4.13: Displacement of the Compton peak with increasing carbon content in steel for SSSs: 154-1 (C_c = 0.42 % mass); and 154-7 (C_c = 1.10 % mass). Smoothing was completed in five points. The arrows indicate the position of the maximum found by the median method.

Conclusion to Chapter 4

In this chapter, we proposed and experimentally substantiated the conditions for measuring the intensity of scattering peaks (sin β/λ, angular $\Delta\beta$ divergence range, and sample temperature), which allow for minimizing

the effect of the artifact associated with the Bragg reflections of the material under investigation on the scattering peaks. This made it possible to apply the Compton effect to solve a number of applied problems associated with the determination of the impurities of light elements in polycrystalline materials. A fundamental dependence of the scattering peak intensity ratio on the atomic number of the scatterer has been obtained for polycrystalline and amorphous materials. This relationship serves as the basis for the new analytical methods presented in Chapter 5.

CHAPTER 5

COMPLEX X-RAY METHODS FOR ANALYSIS OF MATERIAL COMPOSITION

The methods of analyzing the composition of materials by the intensity of fluorescence, scattering, and diffraction reflections considered in the previous sections have significantly expanded the application of X-rays. Owing to the increased spectra contrast, it became possible to not only increase (by one or two orders of magnitude) the sensitivity in detecting "trace" impurities by the fluorescence lines, but to also develop complex measurement techniques, including Compton scattering and X-ray diffraction. This has had a positive effect; first, in the study of systems with light matrix—objects of ecology, biology, and medicine—which were previously almost inaccessible to XRF because of high sensitivity requirements at levels of 0.1 to 1 ppm. Measuring the intensity of fluorescence lines, diffraction reflections, and Compton scattering in a single X-ray spectrum not only expanded the range of chemical elements to be determined down to hydrogen, but also made it possible to simultaneously carry out a quantitative phase analysis of some of the sample's important structural components.

In this section, we will only present the first results from the application of complex X-ray methods in various fields of science and technology. The objects of the study were State Standard Samples (SSS) of aqueous solu-

tions, ferrous and non-ferrous metals, and minerals (coal, gold, etc.). Most of the experiments were carried out using "SPRUT" [67] spectrometers.

The experimental studies presented in this section were performed on SPRUT-type portable spectrometers developed with the authors' participation. The main technical characteristics of these instruments are given below.

The vacuumed scanning crystal-diffraction spectrometer SEF-01-M includes the radiation source, which was a 15 W power X-ray tube BS-22 with a shooting-through anode; an X-ray optical scheme with two Soller collimators (Section 2.3); crystal-analyzers, LiF, HOPG, fullerite, and X-ray multilayer mirrors (W-B_4C, Mo-B_4C, Co-C, Ni-C, and Cr-Se); detectors that have a flow-proportional with a 0.65 μm window (Proline-10); and a scintillation.

The energy-dispersion spectrometer SEF-01-M-1 includes the X-ray radiation source (a BS-22 tube); the secondary target (homogeneous KCl, Sc, Ti, Ge, Y, Nb, Mo, and two-layer Sc/Nb or Ti/Ag); and the detector SDD X-100 (Amptek).

5.1 Determining trace contaminants in pure materials

5.1.1 Express certification of material purity using the ratio of Compton and Rayleigh peak intensities

This method is very effective for detecting heavy impurities in a light matrix or for light impurities in a heavy matrix. Although the method gives an

integral evaluation of all impurities without specifying their type, it is very convenient for a quick estimation of the material's purity.

The calibration curve (Fig. 5.1) for standard samples of primary aluminum (light matrix) clearly shows the linear I_C/I_R ratio of the intensities of the Compton and Rayleigh peaks versus the aluminum content in the mass fraction range of 97.3 to 99.9% mass. From this dependence, it is convenient to sort out primary aluminum in order to avoid painstaking work to determine the concentration of all impurities. Indeed, with a relative concentration sensitivity of $\frac{1}{I}\frac{\partial I}{\partial C} = 2.5\%$ mass (Fig. 5.1) and accurate measuring of the I_C/I_R ratio at about 0.1%, it is possible to determine the purity of aluminum to a level of 99.99% mass.

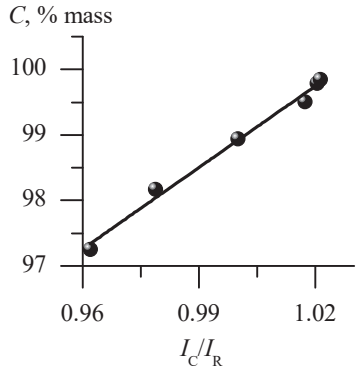

Figure 5.1: Aluminum content in standard samples of primary aluminum vs. Compton and Rayleigh peak intensity ratio I_C/I_R.

5.1.2 Determining the content of "trace" impurities in the light matrix

Gold in ion-exchange resins

Obtaining spectra with a low background level when using the scheme with a secondary target provided the possibility of measuring "trace" gold impurities in a scattering filler as an ion-exchange resin [39]. The measurements were carried out on SSS with gold contents from 0 to 50 ppm (Fig. 5.2). A monotonic decrease in the intensity of the Au-L_α line was observed with a decrease in the gold content. Unfortunately, the standard samples contained other trace impurities: Br, Pb, and Hg. The quantities of which were not certified. The lines of these impurities were superimposed on the Au-L_β line and created difficulties when measuring its intensity. However, the intensity of the Au-L_α line could still be reliably measured in all samples.

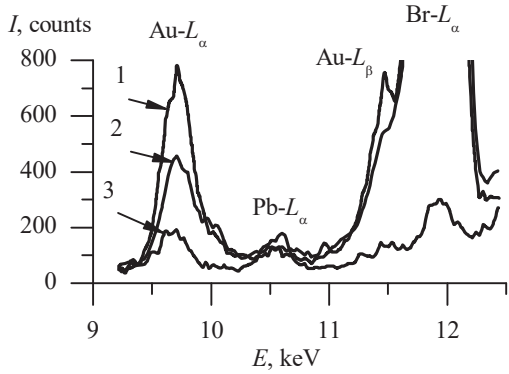

Figure 5.2: Fragments of spectra from standard samples with trace impurities of gold in an ion-exchange resin: 1, 50 ppm; 2, 20 ppm; and 3, 10 ppm. The secondary target is yttrium and the accumulation time is 600 s.

With a gold content of 10 ppm (Fig. 5.2, curve 3), the peak-to-background ratio of the Au-L_α line is 4.2. This peak-to-background ratio makes it possible to use the calibration function to determine traces of precious metals, starting with a gold content of 0.5 ppm.

Figure 5.3 shows the calibration function used to determine the gold content in the ion-exchange resin via the integrated intensity of the Au-L_α line. The monitor signal (I_Y) is the integrated intensity of the Y- K_α and Y- K_α lines scattered by the sample.

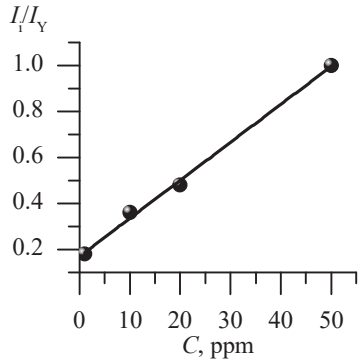

Figure 5.3: The calibration function to determine the gold content in ion exchange resin. The secondary target is yttrium and the accumulation time is 600 s.

In the range of gold mass fractions from 0 to 50 ppm, the standard deviation S of the calibration function is 0.86 ppm.

In this case, the sensitivity determined from the integral intensity of the Au-L_α line is $\partial I/\partial C$ = 105 counts/ppm. The background signal on the "blank" sample (without gold) is 1100 counts. The detection limit is 0.95

ppm, which corresponds to the limit of detection in the spectrometer with the polarization of the primary beam (Barclay's scheme) [68].

Alloys of non-ferrous metals

The modernization of X-ray optical schemes and the use of new crystal analyzers have significantly increased the sensitivity when determining the content of many chemical elements. Figure 5.4 shows a fragment of the pure aluminum standard sample spectrum containing V-K_α, Mn-K_α, and Cr-K_α lines. The spectrum was obtained in the X-ray optical scheme of an EDXRF spectrometer with a secondary target. The contrast of the analytical lines is so high that it provides detection limits for these elements from 1 to 2 ppm in aluminum alloys. These values are at least an order of magnitude lower than in the standard XRF scheme.

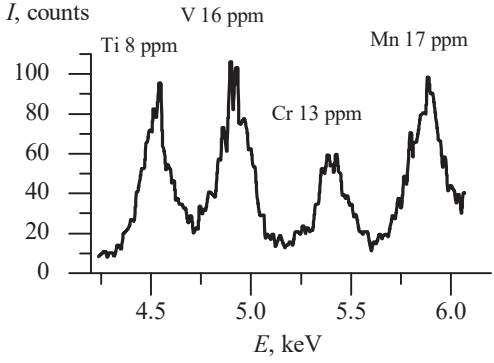

Figure 5.4: A fragment of an X-ray fluorescence spectrum from a standard sample of pure aluminum. The secondary target is germanium and the accumulation time is 300 s.

Table 5.1: The background intensity I_b, concentration sensitivity $\partial I/\partial C$, dispersion of calibration function ΔC, and detection limit C_{min} per 300 s for micro-impurities in pure aluminum. Analyzers: graphite (002) and W-B_4C X-ray mirror with a period of d = 25 Å.

Element	I_b, counts/s	$\partial I/\partial C$, counts/(s·% mass)	ΔC, % mass	$C_{min}\times10^4$ % mass
Mg	24.7	45.8	0.0179	188
Si	27.0	56.2	0.0528	160
Ti	27.0	1832	0.0016	4.9
V	41.0	3676	0.0017	3.0
Cr	78.0	4687	0.0018	3.3
Mn	112	5968	0.0034	3.1
Fe	250	6375	0.0206	4.3
Cu	1030	9897	0.0045	5.6
Zn	280	7267	0.0011	3.9
Pb	348	2027	0.0089	15.9

Table 5.1 gives the contents of impurities in pure aluminum standard samples measured by the calibration plots in the X-ray optical scheme of a crystal-diffraction spectrometer. Despite the low power of the primary source (tube BS-22, power 15 W), the achieved results are not inferior to those obtained on the most modern full-size spectrometers. Indeed, for most impurities, the measurements are successful in terms of several ppm (10^{-4}% mass), and starting from 0.02% for the lightest elements, silicon and magnesium, which is a good result.

From the comparison of the data in Figure 5.4 and Table 5.1, it follows that the sensitivity in detecting "trace" impurities with an atomic number of $Z \geq 22$ is much higher in the scheme of an EDXRF spectrometer with selective fluorescence excitation. However, a vacuum crystal-diffraction spectrometer with broadband fluorescence excitation of the sample provides an advantage in the detection of light elements, particularly magnesium and silicon.

5.2 Studying the characteristics of thin films

In Section 2.5, it was noted that the small-angle X-ray reflectometry is a generally accepted method for studying the characteristics of multilayer structures. The method makes it possible to independently determine the thickness and density of the film by the intensity and positions of the X-ray reflection coefficient's oscillations. Good accuracy is ensured with a film thickness exceeding 50 Å, when more than three orders of oscillations are confidently observed. However, special requirements to the sample surface smoothness are a disadvantage of the method. As an alternative, two other X-ray methods can be considered, which are based on measuring the intensity of fluorescence radiation of either the film itself or the substrate [4].

Figure 5.5 shows a fragment of the fluorescence spectrum from a cobalt film with a thickness of less than 20 Å deposited on a silicon substrate. Owing to the high quality of the spectrum, it is possible to reliably detect the characteristic radiation of a small amount of the substance, which makes it possible to measure the effective thickness of cobalt films by fluorescence intensity, starting from 0.5 Å. Since the intensity of fluorescence is proportional to the mass of the film, rigid requirements to the

quality of the surface are removed; this makes it possible to determine the effective thickness of the "lace" and "island" films.

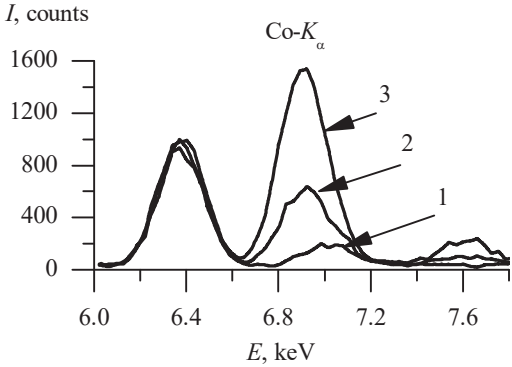

Figure 5.5: Co-K_α fluorescence lines from Co films with different thicknesses: *t*: *1* – t = 0 Å; *2* – t = 6.0 Å; and *3* – t = 18 Å. The secondary target is germanium and the accumulation time is 600 s.

In order to efficiently excite the fluorescence, the sample is irradiated with a wavelength close to the absorption jump of the film material. The radiation of a secondary target from germanium is well suited for cobalt. The disadvantage is that in the study it is impossible to directly determine the thickness of the film, as this can only be performed via the product ($\rho \cdot t$). In this case, the density of the coating can depend on the thickness, especially for the nano-layers. The value of the ($\rho \cdot t$) parameter is determined by the following formula [4, 69]:

$$\rho \cdot t = \left(\frac{\mu_{Co}^{Ge}}{\sin\varphi} + \frac{\mu_{Co}^{Co}}{\sin\psi} \right)^{-1} \cdot \ln\left(1 - \frac{I_{\rho t}^{Co}}{I_{t=\infty}^{Co}} \right), \tag{5.1}$$

where μ_{Co}^{Ge} and μ_{Co}^{Co} are, respectively, mass coefficients of attenuation in the secondary target line Ge-$K\alpha$ and the film analytical line by cobalt; φ is the angle of incidence of the secondary target radiation on the sample; ψ is the angle of fluorescence emission which is registered by a detector; $I_{\rho t}^{Co}$ is the intensity of the film analytical line; and $I_{t=\infty}^{Co}$ is the intensity of the same line for a sample with "infinite" thickness. To check the obtained results, it is possible to calculate the thickness of the coating by the substrate fluorescence radiation absorbed by the film [4, 69]:

$$\rho \cdot t = \left(\frac{\mu_{Co}^{Ge}}{\sin\varphi} + \frac{\mu_{Co}^{Si}}{\sin\psi} \right)^{-1} \cdot \ln\left(\frac{I_{t=0}^{Si}}{I_{\rho t}^{Si}} \right), \tag{5.2}$$

where μ_{Co}^{Si} is the mass coefficient of attenuation of the substrate analytical line by cobalt; $I_{\rho t}^{Si}$ is the intensity of the substrate analytical line taking into account the radiation portion absorbed by the film; and $I_{t=0}^{Si}$ is the intensity of the same line in the absence of a film.

Figure 5.6 shows the results of studying cobalt films with different thicknesses deposited on silicon substrates. Oscillations of the X-ray reflection coefficient were confidently observed on the sample with a cobalt film thickness of 168 Å. The value of the ($\rho \cdot t$) was $13.44 \cdot 10^{-6}$ g/cm^2.

The other two methods for the same samples yielded close values of this parameter: $13.87 \cdot 10^{-6}$ g /cm^2 (the intensity of the fluorescent radiation of

the film), and $14.04 \cdot 10^{-6}$ g /cm^2 (absorption of the substrate fluorescence radiation in the cobalt film). Thus, the relative error in measuring the ($\rho \cdot t$) value did not exceed 2%. With decreasing film thickness, the fluorescence intensity of the cobalt dropped linearly; this is explained by the linear dependence of the fluorescent radiation intensity on the mass of the chemical element.

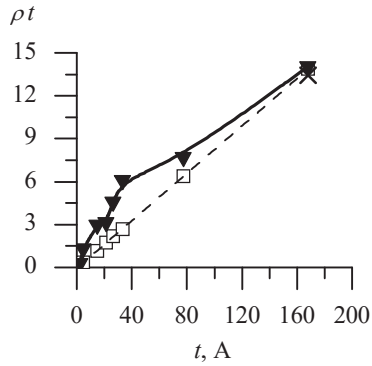

Figure 5.6: Determination of the coating thickness by three independent methods: (×), the positions and intensity of oscillations of X-ray reflection coefficient; (□), the intensity of fluorescence of the film (Co-K_α line); and (▼) the intensity of fluorescence of the substrate (Si-K_α line).

The determination of the film thickness from the absorption of the substrate fluorescent radiation in the film material gave higher ($\rho \cdot t$) values, and the dependence of ($\rho \cdot t$) on t was clearly nonlinear because at low thicknesses a sharp increase was observed in the range of 1 to 35Å. As the thickness increased, the curve asymptotically approached the linear dependence characteristic of the film fluorescence. This effect is probably associated with a violation of the film's outer boundary's strict planarity at the initial stage of growth [37]; as a result, the adopted model of absorp-

tion of the substrate radiation by plane film becomes inadequate for the object. It should be noted that the method of small-angle X-ray reflectometry does not take into account the presence of substrate regions that are not covered by the film, as in the case of the thinnest discontinuous samples. The model used for the calculation assumes the homogeneity of the film's thickness over the entire surface of the substrate. As a result, when calculating thicknesses less than 50 Å, the volume and mass of the coating chemical element can be overestimated. From our point of view, the most reliable results in the range of small thicknesses are obtained using the fluorescence intensity of the film material, because it is less sensitive to the uniformity of the coating.

5.3 Analyzing the distribution of impurities in the substrate depth

Controlling the distribution of elements with an atomic number $Z < 9$ in the substrate depth is very relevant for various types of surface processing of materials. In Chapter 4, we considered a method for impurity depth distribution analysis based on measuring the ratio of Compton and Rayleigh scattering peaks. Here, we present the results of experimental measurements that have been performed on model samples of beryllium ($Z = 4$) and aluminum ($Z = 13$) foils, as well as on real coatings from boron ($Z = 5$) and titanium nitride.

The objects of the study were model samples and real coatings. The model samples were made of 30 μm thick beryllium foils and 20 μm thick aluminum foils on steel substrates. The attestation of the foils in the value of the mass absorption coefficient μ was carried out via X-ray absorption analysis with Cu-Kα radiation.

One sample—an analog of a model foil on a substrate—had a coating of titanium nitride deposited by ion-plasma sputtering at a low substrate temperature. A TiN layer with a thickness of 5.9 μm was deposited on a substrate of the same material as for the model samples.

Boron-based coating was another sample. The substrate for this coating was alloy steel: C (0.12÷0.19% mass), Cr (10÷11.5% mass), Mo (0.6÷0.8% mass), and V (0.25÷0.40% mass). The samples were ground, degreased, and coated with a plaster that contained a material supplying free boron atoms (B_4C), an activator (NaF), and a binder. After drying, the samples were held for 1.5 hours at a temperature of 950 to 1000°C. The samples were cleaned of plaster and protective backfill residues by settling them in water for 30 minutes. The certification of the boron coatings was carried out using cross-section metallography, as well as X-ray phase analysis in Cu-$K\alpha$ radiation.

The scheme of the measurements is shown in Figure 4.1. An X-ray tube with a molybdenum anode illuminates the surface of the sample through a collimator. The sample is mounted on a goniometer and can be rotated by means of a lever with a micro-screw in a range of α angles from − 15° up to + 8°. The scattered radiation passes through the first Soller collimator with an angular divergence of 0.2 degrees, it is reflected from the monochromator (a highly oriented pyrolytic graphite HOPG), and then enters the scintillation detector through the second Soller collimator. The scattering angle is $2\beta = 96^{o}$.

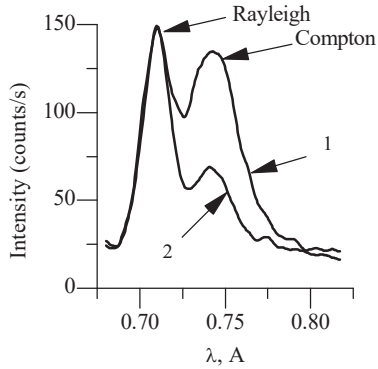

Figure 5.7: Experimental scattering peaks scanned at different exit angles ψ for beryllium foil on steel. The radiation is Mo-$K\alpha$ and the scattering angle is 2β = 96°. The Rayleigh peak normalizes the spectra: 1, ψ = 2° and 2, ψ = 11°.

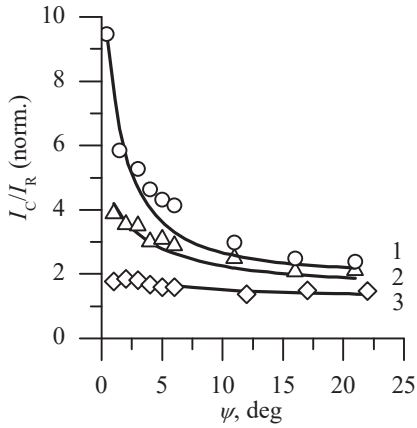

Figure 5.8: Experimental dependences of the Compton-to-Rayleigh scattering peak intensity ratio on the radiation exit angle ψ for various coatings on steel. Experimental data are normalized by the I_C/I_R ratio for the substrate. Solid lines show theoretically calculated data: 1, 30 μm beryllium foil; 2, 20 μm aluminum foil; and 3, 6 μm titanium nitride coating.

The peak intensities of Rayleigh and Compton scattering (Fig. 5.7), as well as the background, were measured by collecting pulses for 4×60 s at each measuring point. The impulse-statistic error when measuring the peaks did not exceed 0.5% of the measured value. The ratio of the peak intensities was calculated after subtracting the background.

The experimental scanning spectra taken from the coating side have different values of the exit angle ψ (Fig. 4.1) differ considerably in the ratio of the peaks. Under our conditions, the half-width of the Compton peak is 2.3 times larger than that of the Rayleigh peak. Therefore, we cannot directly compare the ratio of peak intensities with the theoretical ratio for integrated intensities. In order to take this difference into account, as well as the geometric factor, each sample was measured both from the side of the coating and from the side of its substrate at the following values of the radiation exit angle: ψ = 1, 2, 3, 4, 5, 6, 11, 16, and 21°. The experimental ratios of the peak intensities for the coating were normalized in comparison to these for the substrate. These normalized experimental values were used to fit the theoretical curve. The results of the measurements are given in Tables 5.2 and 5.3.

Consider the results of the fitting for two model samples: beryllium and aluminum foils on steel substrates. Beryllium (Z = 4) has an I_C/I_R ratio that is a factor 30 greater than for steel. The thickness of the beryllium foil at 30 μm is less than the radiation penetration depth d into beryllium ($d \approx$ 75 μm at $\psi = 1°$ and $d \approx 2280$ μm at $\psi = 21°$). Thus, a superposition of the scattering from the foil and the substrate occurs.

Table 5.2: Compton-to-Rayleigh scattering peak intensity ratios measured for the steel substrate and deposited coatings of Be, Al, and TiN at different exit angles ψ.

ψ^o	Substrate	Be 30 μm	Al 20 μm	TiN 6 μm
1	0.1334	1.2620	0.5165	0.2371
2	0.1065	0.6228	0.3768	0.1960
3	0.0878	0.4630	0.3071	0.1597
4	0.0822	0.3805	0.2461	0.1377
5	0.0773	0.3338	0.2386	0.1237
6	0.0744	0.3076	0.2152	0.1190
11	0.0728	0.2174	0.1813	0.1003
16	0.0860	0.2135	0.1782	0.1282
21	0.0923	0.2208	0.1946	0.1365

It is clear that the observed multiple lowering the I_C/I_R ratio (Table 5.2) with the penetration depth increase (Fig. 5.8, curve 1) is due to the increasing substrate contribution to the scattering. The parameters from formula (4.14) are easily determined by fitting: C_0 = 99 at % and x_0 = 35 μm. We note that the effect is rather great. According to our estimates, it is possible to reveal layers of light elements ($Z \leq 4$) with a thickness of a fraction of a micron on the surface of materials with $Z \geq 20$.

Aluminum with an atomic number Z = 13 is characterized by a much smaller I_C/I_R ration. Nevertheless, a 20 μm foil on the surface increases the ratio by almost three times compared to the steel substrate. In this case, we find C_0 = 100 at % and x_0 = 22 μm through fitting, which is in satisfac-

tory agreement with the certified characteristics of this object. As expected, the sensitivity of the detection of a thin aluminum layer (Z = 13) is much worse than beryllium (Z = 4) and does not exceed 0.5-1 μm under our experimental conditions.

Table 5.3: Compton-to-Rayleigh scattering peak intensity ratios measured at different exit angles ψ for the steel substrate and a boron-containing coating in its initial state and after polishing

ψ,°	Substrate	Initial B-coating	ψ,°	Substrate	Initial B-coating
1.2	0.1772	0.3063	7.0	0.0897	0.1235
2.5	0.1205	0.1949	11.0	0.0806	0.0970
3.7	0.0978	0.1649	16.0	0.0845	0.1012
4.7	0.1007	0.1425	21.0	0.0937	0.1048
5.7	0.1020	0.1344			
0.5	0.1454	0.2163	5.0	0.0813	0.1052
1.0	0.1050	0.1412	5.5	0.0800	0.0984
1.5	0.0983	0.1309	6.0	0.0784	0.0993
2.0	0.0938	0.1247	8.5	0.0739	0.0897
2.5	0.0883	0.1180	11.0	0.0764	0.0955
3.0	0.0835	0.1166	13.5	0.0781	0.0907
3.5	0.0801	0.1123	16.0	0.0777	0.0958
4.0	0.0811	0.1099	18.5	0.0831	0.0998
4.5	0.0806	0.1056	21.0	0.0838	0.0999

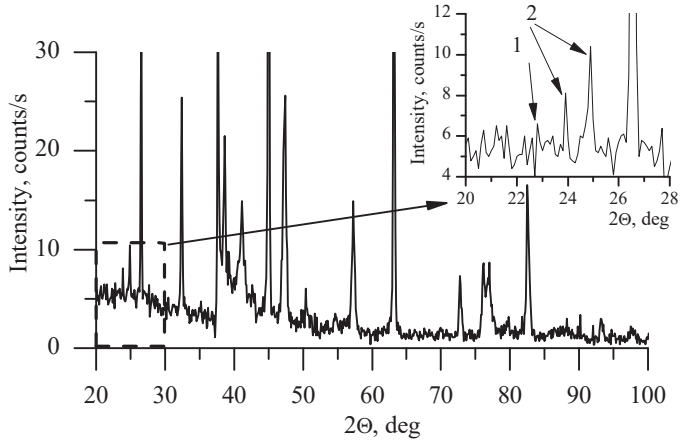

Figure 5.9: XRD patterns from boron based coatings on steel substrate. All strong reflections correspond to the FeB phase: 1, halo from an amorphous phase and 2, reflections of high boron-containing phases.

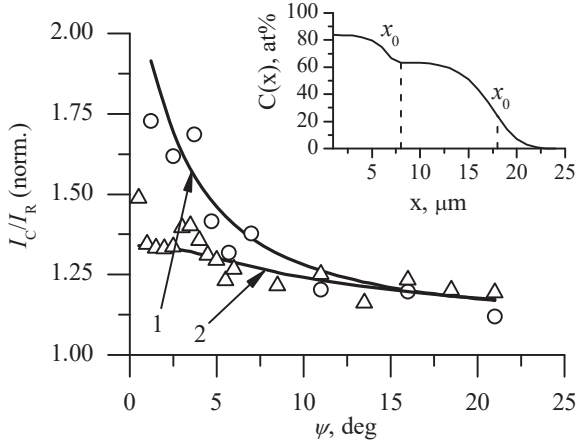

Figure 5.10” Scattering peak intensity ratios versus the radiation exit angle for a boron-based coating. Experimental data are normalized by the ratio for the substrate: 1, initial coating and 2, coating after polishing.

A real sample—an analog of model foils on a substrate—is a coating of titanium nitride deposited on a steel substrate by ion-plasma sputtering at a low temperature. Interfacial interaction of the coating material with the substrate was practically absent, and no extraneous phases were detected with XRD. The average value of the atomic number of titanium nitride Z = 14.5 is very close to aluminum. The essential difference consists in a much lower penetration depth of Mo-$K\alpha$ radiation in TiN (μ = 108.8 cm^{-1}) than in aluminum (μ = 18.5 cm^{-1}). As long as the thickness of the coating is greater than the penetration depth of the probing radiation, the contribution of the substrate to the scattering will be absent. In this case, the experimental curve must be parallel to the abscissa axis in principle. As soon as the depth of penetration becomes greater than the thickness of the coating, the contribution of the substrate to the scattering manifests itself and the level of the experimental curve decreases. For the first three experimental points (ψ = 1°, 2°, and 3°; Table 5.2), the depth of penetration does not exceed the thickness of the TiN layer, and a constant-level section is observed on the curve (Fig. 5.8, curve 3). As the penetration depth increases, the contribution of the substrate to the scattering increases and the scattering level decreases smoothly. Fitting the theoretical curve to the experimental curve yields a value of C_0 = 100 at % and x_0 = 8 μm, which is close to the certified values.

Consider another real sample: a boron-containing coating on steel. This coating is not completely analogous to the beryllium foils because of the possible interfacial interaction. Indeed, in the XRD pattern, in addition to the main FeB phase, an intense halo from an amorphous phase and reflections from boron-containing phases with a complex crystal lattice are revealed (Fig. 5.9, positions 1 and 2 in the insert). Table 5.3 and Figure 5.10

(curve 1) show a significant decrease in the ratio of the scattering peaks with an increasing radiation exit angle. The fitting leads to the following solution: C_0 = 84 at % and x_0 = 8.0 μm. This means that, in addition to FeB with C_0 = 50 at %, a thin layer with high boron content is present on the surface. Perhaps it is due to baking the plaster's particles. Surface polishing was carried out to remove the top layer, which is 3–5 μm thick. After polishing, only the reflections from the main FeB phase remained on XRD patterns, while the amorphous halo and extraneous reflections were not observed. This means that the high boron layer was removed. After polishing, the character of the I_C/I_R dependence on the radiation exit angle changed qualitatively (Fig. 5.10, curve 2): the I_C/I_R ratio significantly decreased and practically did not change with the increasing depth of penetration. This means that after polishing a sufficiently thick layer with a low boron concentration remained on the surface. The fitting led to the following solution: C_0 = 61 at % and x_0 = 15 μm. The structural scheme of the coating is shown in Figure 5.10. A layer of 8 μm with a high boron content is present on the surface and below this there is a thicker layer, which is based on FeB. This data is in good agreement with the results of cross-section metallography. There is a loose layer, which is about 5 μm thick on the surface, and a dense 20μm layer below it.

5.4 Determination of light elements in heterogeneous samples using WDXRF

The determination of the content of light elements with Z ≤ 8 in heterogeneous systems cannot be performed by usual non-destructive methods. A good technique is the use of X-ray mirrors: Co-C, W-B_4C, W-Si, $MoSi_2$-

Si, Cr-Sc, and ultra-thin Proline 10 windows with a thickness of 0.65 μm. In this section, we will present the results of quantitative determination of a number of light elements by the analytical line intensity: Na-*K*α (λ = 11.9 Å), F-*K*α (λ = 18.3 Å), O-*K*α (λ = 23.6 Å), N-*K*α (λ = 31.6 Å), C-*K*α (λ = 44.7 Å), and B-*K*α (λ = 67.6 Å).

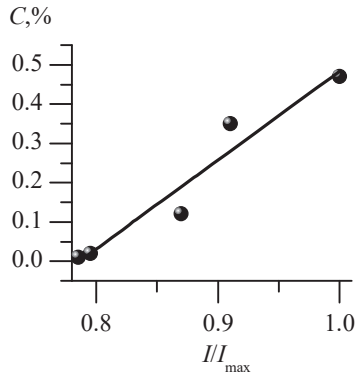

Figure 5.11: Calibration of kaolin samples using sodium. The X-ray mirror is Mo-B_4C and the accumulation time is 6×100s.

Figure 5.11 shows the experimental calibration for the sodium content in powder samples of kaolin that has been compressed into tablets. The standard deviation, D = 0.04% mass, is acceptable for qualitative measurements, and the detection limit according to the calibration is about 0.02% mass. The spectra of binary compounds with light elements also have low contrast levels (Fig. 5.12). The detection limits obtained for various binary systems were about 0.05% mass (O_2), 0.1% mass (N_2), and 0.05% mass (C). These values cannot compete with the results of other modern methods. However, considering the uniqueness of the non-destructive analysis resulting from the XRF method, it means it can be

used for the certification of both powder and film materials, and for the analysis of a stoichiometric violence in oxides, nitrides, and carbides.

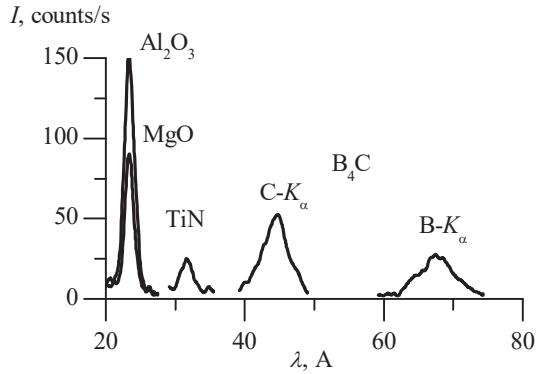

Figure 5.12: Light element spectra of some binary compounds. The X-ray mirrors are Mo-B_4C (for Al-$K\alpha$, Mg-$K\alpha$), and Co-C (for C-$K\alpha$, B-$K\alpha$).

Significant difficulties are caused by the large dispersion of the calibration function, which is difficult to control experimentally. Thus, for example, the calibration plot of Al-Al_2O_3 powder mixtures by oxygen (Fig. 5.13) in the range of Al_2O_3 mass fractions from 34 to 61% mass is characterized by a dispersion of 3.22% mass, which results in the low accuracy of measurements using the O-K_α line. This difficulty was overcome by implementing additional measuring for the I_C/I_R ratio of the Compton and Rayleigh peaks intensities (Fig. 5.14).

The dispersion of the calibration function of 0.73% mass provides an acceptable accuracy of Al_2O_3 measurements. However, it is necessary to control the level of concomitant impurities of nitrogen and carbon using a vacuum device for this type of measurement. This is because as the content of these impurities becomes more than 0.3-0.5% mass a systematic

error in the determination of Al_2O_3 by the Compton scattering may occur, and a corresponding correction is required.

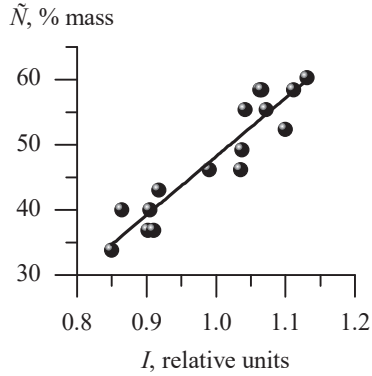

Figure 5.13: The calibration function that determines the Al_2O_3 content in Al-Al_2O_3 powder mixtures using the intensity of the O-K_α line. The multilayer X-ray mirror is Co-C and the exposure is 120 s.

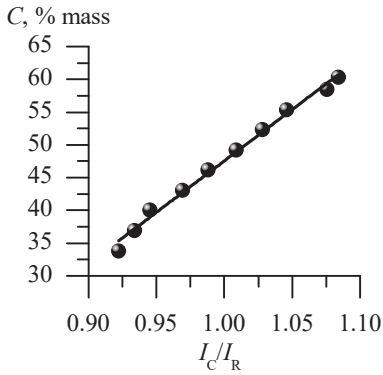

Figure 5.14: The calibration function that determines the Al_2O_3 content in Al-Al_2O_3 powder mixtures using the Compton and Rayleigh peak intensity ratio. The secondary target is molybdenum and the exposure is 120 s.

The proposed approach makes it possible to carry out an express analysis of the light element content using fluorescence intensity with an independent Compton scattering control.

5.5 Analyzing the composition of multiphase systems using combined X-ray scattering, fluorescence, and diffraction spectra

An example of a complex analysis of materials using several X-ray methods is the determination of the impurity content in steels and cast irons. In subsections 2.5.2 and 4.3, we considered the theoretical possibilities for determining the main impurity—carbon—using the fluorescence intensity of the C-*K*α line, as well as the ratio of the Compton and Rayleigh scattering peaks. Both of these methods provide approximately the same detection limit, ≈ 0.1% mass, and the measurement accuracy of about 0.05 to 0.07% mass, but cannot be realized in a single X-ray optical system.

Let us consider an example of a simultaneous elemental and phase analysis of iron-based alloys within the same spectrum. In Section 3.3, we presented an X-ray optical scheme with a complex secondary target, which made it possible to obtain a joint fluorescence and diffraction spectrum. Thus, the content of most impurities is determined from the intensity of the fluorescence lines and the carbon content using the intensity of the diffraction reflections of cementite in a certain range of interplanar distances.

The method's main difficulty is its extremely high requirements for the spectrometer's collimating system, since even a minimal capture of the main-phase reflections' "tails" leads to a loss of sensitivity and "missed"

measurements. However, an excessive decrease in divergence leads to a loss of luminosity and makes it difficult to analyze the light elements using their fluorescence emission. Therefore, the combination (in the same device) of an X-ray diffraction scheme tuned for low divergence and an X-ray spectral scheme with large divergence requires a system of standard samples to adjust and calculate the characteristics of the secondary targets in order to solve this problem (materials, scattering angles).

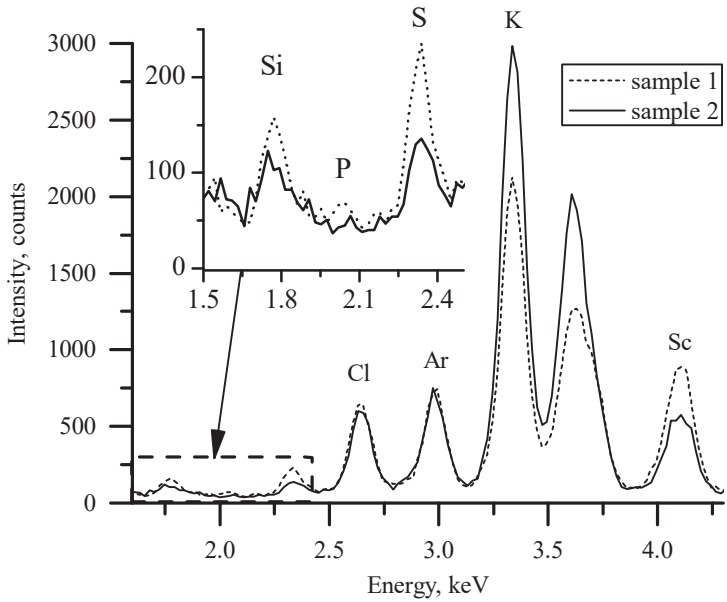

Figure 5.15: Fragments of the X-ray spectra for two carbon steel standard samples. A combined KCl-Sc secondary target was used. The spectrum contains diffraction reflections of the sample in Sc-*Kα*, K-*Kα*, and Cl-*Kα* radiations, and fluorescence lines of silicon, phosphorus, and sulfur. The accumulation time is 120 s. Concentrations of elements are as follows: Sample 1: C (0.43% mass), Si (0.311% mass), and P (0.025% mass); Sample 2: C (0.053% mass), Si (0.061% mass), and P (0.010% mass).

Figure 5.15 shows a fragment of the carbon steel spectrum, which contains the components' fluorescent emission lines and the sample's diffraction reflections, thereby tuning *d* from 1.69 to 1.89 Å (see Section 3.2.3). The diffraction reflections of iron and cementite were obtained by means of secondary targets from scandium, potassium, and chlorine. The carbon content was determined from the intensity of the diffraction reflections. The analytical lines of silicon, phosphorus, and sulfur were clearly observed in their contents of 0.01 to 0.1% mass.

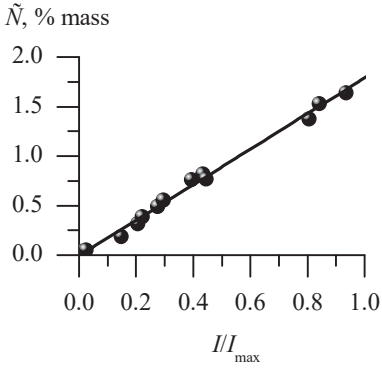

Figure 5.16: The calibration function used to measure carbon in low-alloy steels using diffraction reflections from cementite.

Figure 5.16 shows the calibration function for carbon plotted on the base of the integrated intensities from the cementite diffraction reflections. The spectrometer was tuned in the range of interplanar distances *d* from 1.69 to 1.89 Å. In this range, there are no diffraction peaks of α-Fe, but intense reflections of cementite (Fe_3C) that correspond to interplanar distances of d = 1.867 Å and d = 1.687 Å. A low level background when using the scheme with a complex secondary target made it possible to obtain a very high sensitivity of the calibration function, where a variation of 1% mass

in the carbon content corresponds to a change in the intensity of the diffraction reflections ≥ 64.4%. Thus, with the real accuracy for the integrated scattering intensity measuring about 0.5%, the carbon content is determined with an accuracy of 0.01% mass in principle.

Table 5.4: Results from analyzing the composition of the 127-6 standard sample using the calibration function. The carbon mass fraction is determined from the Fe_3C diffraction reflections, and the remaining elements are measured using the intensity of the fluorescence lines. The secondary target is Sc + KCl and the accumulation time is 300 s.

Element	Mass fraction (certified), % mass	Mass fraction, (measured), % mass	Error, % mass
Carbon	0.348	0.324	0.0343
Aluminum	0.124	0.155	0.0246
Silicon	0.301	0.322	0.054
Phosphor	0.012	0.016	0.006
Sulfur	0.014	0.017	0.006
Titanium	0.084	0.102	0.024
Vanadium	0.003	0.005	0.003
Chromium	0.301	0.320	0.012
Magnesium	0.197	0.203	0.023
Nickel	0.286	0.310	0.012
Copper	0.071	0.095	0.017

The experimentally obtained standard deviation S = 0.047% mass of the calibration function for three different sets of standard samples provides a measurement accuracy of 0.05% mass in a concentration range from 0.02 to 1.7% mass, even when using standard samples from different sets. Within one set of SSS, it was possible to obtain S = 0.03% mass and a measurement accuracy of about 0.04% mass. Any further increase in the accuracy is limited by the impulse-statistical error, which is $\Delta C = \pm$ 0.013% mass for small concentrations, and $\Delta C = \pm$ 0.021% mass for large concentrations.

The results of Table 5.4 show the expansion in the XRF scope when using combined fluorescence and diffraction spectra.

So, we considered an example for application of the method that used the combined spectra and determined the light element (C) using the quantity of the corresponding phase (Fe_3C).

As shown in Section 3, the diffraction part of the spectrum can be tuned to any given range of interplanar distances by selecting the secondary target wavelength and an angle range of $\theta \pm \Delta\theta$ for the diffraction reflections. This opens up the possibility of a comprehensive solution for not only fdetermining the elemental composition, but also for a quantitative assessment of the characteristic phases' content. Such tasks are often encountered when controlling the processing of minerals, as well as in the chemical and metallurgical industries.

5.6 Experimental comparison of the analytical capabilities of various selective excitation schemes

Improvement of the device characteristics using a scheme with selective excitation of fluorescence is well illustrated by the data provided in Table 5.5. In the first variant of the scheme, the composite secondary target contains a single crystal, KCl (001), which is angular-aligned so that its crystal planes (002) reflect the long-wave portion of the tube spectrum adjacent to the *L*-series spectral lines of the silver anode. This "diffraction" tuning doubles the excitation efficiency of light elements (S, P, Si, Al, and Mg) compared to the tuning to the fluorescence emission of KCl or Sc secondary targets. This ensures that the fluorescence of light elements can be vacuum-free measured up to magnesium using a tight arrangement in the spectrometer. A negative effect of “diffraction tuning” is the increased background created by the continuous spectrum segments with wavelengths near $\lambda/2$, $\lambda/3$, etc., which are reflected by the (400), (600), etc. planes, respectively. Also, the broadband regions in the continuous spectrum play a positive role, since they stimulate the fluorescence of the “medium” elements.

In contrast to the XRF excitation from an X-ray broadband spectrum when using diffraction tuning, a significant increase in the fraction of the long-wavelength component from the broadband spectrum provided, because the reflection coefficients for the (002) planes are at least four times larger than those for the (004) planes (see the estimate in Section 1.7) and are an order of magnitude larger than those of the (006) planes. Thus, the diffraction tuning makes it possible to increase the excitation efficiency of light elements by about an order of magnitude compared with the medium ones. It has been experimentally established that, under such excitation, the fluo-

rescence intensity of a single-component sulfur reference can be brought to the level of the intensity of an iron standard, if an X-ray tube voltage greater than 20 kV is used. In the standard XRF scheme that uses this voltage, the sulfur line would be at least an order of magnitude smaller than the iron line. Since the total load of the detector is limited by the counting speed and is determined by high-intensity lines of the main elements, it is impossible to detect small amounts of light impurities in the standard XRF scheme.

Diffraction tuning is extremely useful for increasing the sensitivity in the determination of light elements in the matrix from medium and heavy elements within a single spectrum. Generally, in order to detect light elements in the standard XRF scheme, it is necessary to reduce the X-ray tube voltage to 8÷10 kV to decrease the detector load of high intensity lines of the base component [13]. This makes it not only necessary to take two measurements of the sample at low and nominal voltages, but it also significantly reduces the efficiency of excitation of light elements due to the imminent loss of the source power when operating at a low voltage.

An artificial increase (by an order of magnitude) in the intensity of the long-wave component of the continuous spectrum incident on the sample, in comparison with the rest of the spectrum, provides the possibility to increase the tube voltage to 20 kV and higher, where the tube operates in a stable mode and develops the rated power. From the data in Table 5.5, it follows that the diffraction tuning of a KCl single crystal in the complex Sc + KCl secondary target makes it possible to measure small amounts of magnesium and silicon in aluminum alloys without vacuuming the sample or the spectrometer channels.

Table 5.5: Concentration sensitivity ∂I/∂C, background intensity I_b, and detection limit C_{min} of impurities in standard samples of pure aluminum. The determination of concentration was carried out using calibration functions and the accumulation time is 300 s.

	Vacuumed crystal-diffraction spectrometer			Air energy-dispersive spectrometer Secondary target Sc+KCl			Air energy-dispersive spectrometer Secondary target Ge		
Impurity	$\partial I/\partial C$, counts/s·%	I_b, counts/s	C_{min}, % mass	$\partial I/\partial C$, counts/s·%	I_b, counts/s	C_{min}, % mass	$\partial I/\partial C$, counts/s·%	I_b, counts/s	C_{min}, % mass
Mg	45.8	24.7	0.0188	3.92*)	6.10*)	0.109*)			
Si	56.2	27.0	0.0160	10.59	2.41	0.0254	3.04	1.56	0.071
Ti	1832	27	$4.9\cdot10^{-4}$	65.73	1.46	$3.18\cdot10^{-3}$	771.1	2.0	$3.19\cdot10^{-4}$
V	3677	41	$3.02\cdot10^{-4}$	81.13	0.67	$1.75\cdot10^{-3}$	887.2	2.1	$2.83\cdot10^{-4}$
Cr	4687	78	$3.26\cdot10^{-4}$	141.7	1.16	$1.32\cdot10^{-3}$	1776	1.7	$1.27\cdot10^{-4}$
Mn	5969	112	$3.07\cdot10^{-4}$	143.6	6.93	3.17·10–3	2213	3.4	$1.44\cdot10^{-4}$

Table 5.5 continuation

	Vacuumed crystal-diffraction spectrometer			Air energy-dispersive spectrometer Secondary target Sc+KCl			Air energy-dispersive spectrometer Secondary target Ge		
Impurity	$\partial I/\partial C$, counts/s·%	I_b, counts/s	C_{min}, % mass	$\partial I/\partial C$, counts/s·%	I_b, counts/s	C_{min}, % mass	$\partial I/\partial C$, counts/s·%	I_b, counts/s	C_{min}, % mass
Fe	6375	250	$4.29\cdot10^{-4}$	177.7	40.0	$6.16\cdot10^{-3}$	2599	26.9	$3.45\cdot10^{-4}$
Cu**	9897	1030	$5.62\cdot10^{-4}$				6098	27.5	$1.49\cdot10^{-4}$
Zn	7267	280	$3.99\cdot10^{-4}$	177.5	16.7	$3.99\cdot10^{-3}$	9395	22.8	$9.85\cdot10^{-5}$
Pb	2027	348	$1.59\cdot10^{-4}$	65.6	9.9	$8.31\cdot10^{-3}$			
Cu***				37.63	14.0	0.017	1049	27.5	$8.77\cdot10^{-4}$

*) The objects of the research are SSS from AK5M2 aluminum, series 182; the range of magnesium concentrations is from 0.23 to 0.71 % mass.

**) Using the Cu-K_α line.

***) Using the Cu-K_β line.

Although the sensitivity of determining the medium elements in this scheme is much worse, it is quite acceptable for practical applications (Section 5.4). A considerable increase in the sensitivity of the medium elements can be achieved with the help of a scheme with a germanium secondary target, whose fluorescence line effectively excites impurities with an atomic number Z from 30 (Zn) to 22 (Ti) (Fig. 5.17). As follows from Table 5.5, the detection limits for these elements are significantly lower than using the crystal-diffraction spectrometer, even for samples based on aluminum, which is not a strong scatterer.

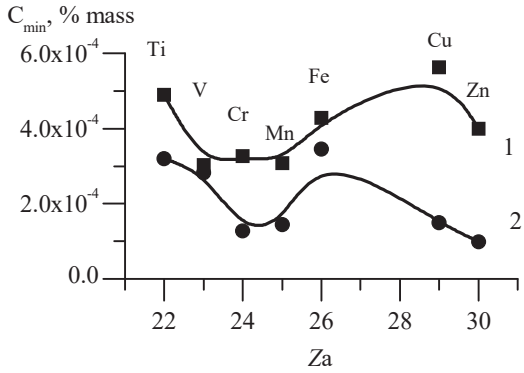

Figure 5.17: Detection limits for impurities from 22(Ti) to 30(Zn) in standard samples of pure aluminum. The exposure is 300 s: 1, vacuum spectrometer (excitation of fluorescence with the spectrum of a tube with a silver anode) and 2, air EDXRF spectrometer (the secondary target is germanium).

Thus, the scheme with the fluorescence selective excitation and the spectrum accumulation time of 600–1000 seconds provides a quantitative determination of "trace" impurities with a content of less than 1 to 2 ppm, even with portable equipment.

5.7 Determination of ash content in coal

Coal is a multi-component mixture of carbon based combustible materials and a mineral component consisting of magnesium, aluminum, silicon, calcium, titanium, iron, and other oxides. A fuel's consumer merits are first characterized by the ratio of combustible and incombustible components. A generally recognized method to determine the coal mineral constituent (ash content) [70] is to use air combustion (ashing) and calcination in order to reduce the ash residue to a constant mass. The ash content in the sample is calculated on the basis of the ash mass. A disadvantage of this method is the significant expenditure of time for the analysis. One of the more rapid methods used for ash content determination is EDXRF analysis [71–73] where the mineral component amount is determined as a sum of all the oxide concentrations. The concentrations are evaluated by the intensities of secondary emission (fluorescence) lines. However, it is known from the literature [5] that light element fluorescence intensity is strongly dependent on the grain size. This effect is related to the low penetrability of radiation with an energy level of $E < 2$ keV. Thus, as the grain average increases in size from 2.3 μm to 50 μm, the fluorescence intensity decreases by a factor 5 for sodium, by a factor 4 for magnesium, and by a factor 3 for aluminum, etc. Plant laboratories have occasional technology facilities to prepare samples with a grain size lower than 60 μm. In addition, quantitative measurements of the carbon low-energy fluorescence (E=0.28 keV) are practically impossible for powder samples.

An alternative method to determine concentrations in elements with a low atomic number is by measuring the Compton and Rayleigh peak intensity ratio: I_C/I_R [56–58]. This ratio sharply increases with a decrease in the

atomic number and can be calculated for any aggregation of scattering atoms [59]. As the scattered X-ray radiation with photon energy $E > 17$ keV has a significantly higher penetrability than the fluorescence radiation of light elements, their grain sizes are no object; therefore, the sample preparation procedure can be simplified.

5.7.1 Calibration plots

We use the $y_i=ax_i+b$ function to obtain a linear calibration when measuring standard samples. Usually, certified mass fractions are denoted as x_i, and measured analytical signal values as y_i. Here, the experimental $y=I_C/I_R$ ratio is denoted as an analytical signal, and x_i according to the formula

$$x = \frac{1 + pA_d + qW_{Fe_2O_3}}{1 + mA_d + qW_{Fe_2O_3}} = \frac{y - b}{a}. \tag{5.3}$$

In this calibration, the x_i depends on the mass fractions of ash, A_d, and iron oxide, $W_{Fe_2O_3}$, in the standard samples; a and b are the fitting parameters determined in the calibration procedure.

In the experimental spectra (Fig. 5.18), we cannot remove the background completely or separate the Compton and Rayleigh scattering peaks perfectly. The integral intensity of each peak is partially measured in certain ranges of photon energy. Therefore, the experimental I_C/I_R ratios differ from the calculated ones; this difference is taken into account by using fitting parameters in the calibration procedure.

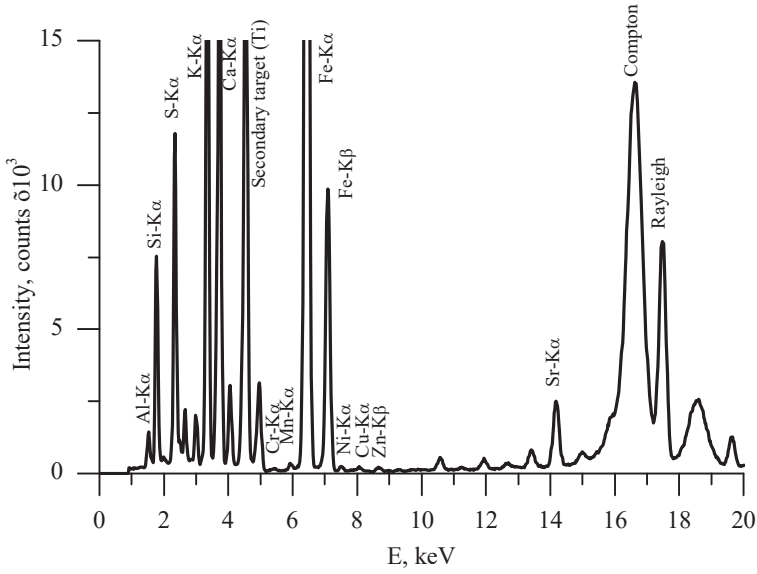

Figure 5.18: The combined X-ray spectrum of a powder coal sample. The secondary target is Ti/Mo, and the scattering angle is 130°. The titanium scattering peak is labeled, "Secondary target".

The calibration procedure of the experimentally measured ratio $y = I_C / I_R$ is fulfilled using 17 standard samples with certified A_d and $W_{Fe_2O_3}$ values (Fig. 5.19). Coal standard samples and experimental ones (Table 5.6) were powdered to granules about 60 μm. No tableting was used.

The experimental I_C/I_R ratios measured with the standard specimens are calibrated using a linear function in a very wide range from A_d (from 7 to 56% mass) and $W_{Fe_2O_3}$ (from 0.2 to 6.5% mass). The standard deviation

from the linear regularization solution did not exceed 0.005. This allows for the application of x values calculated by (5.3) in the usual calibration procedure; the obtained a and b parameters are then used to calculate A_d.

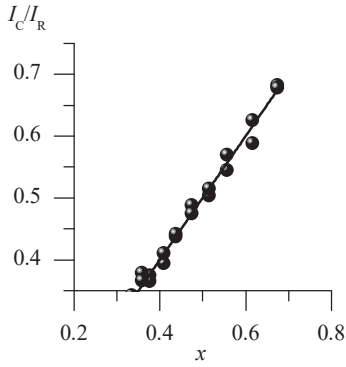

Figure 5.19: Calibration of the Compton-to-Rayleigh scattering intensity ratio using the x parameter from Eq. (5.3)

An unknown sample is measured using the following sequence. First, the iron oxide mass fraction, $W_{Fe_2O_3}$, is determined by the iron fluorescence intensity using a relevant calibration plot. Then, the measured y and $W_{Fe_2O_3}$ values are used for the A_d calculation:

$$A_d = \frac{b + a - y - W_{Fe_2O_3}\left(y\,n - b\,n - a\,q\right)}{\left(y\,m - b\,m - a\,p\right)}. \tag{5.4}$$

It is important to note that for the determination of the ash mass fraction, it is not necessary to measure the fluorescence measurements of light elements.

Using the proposed method we can theoretically estimate an ash mass fraction measurement error, ΔA_d, depending on the I_C/I_R and $W_{Fe_2O_3}$ measurement errors. The ΔA_d is determined as the total differential of Eq. (5.4):

$$\Delta A_d = \frac{\partial A_d}{\partial y}\Delta y + \frac{\partial A_d}{\partial W_{Fe_2O_3}}\Delta W_{Fe_2O_3}. \tag{5.5}$$

Here, the first term, ΔA_{d1}, is defined by the measurement error for the ratio of scattering signals, Δy; and the second one, ΔA_{d2}, by the measurement error of the iron oxide mass fraction, $\Delta W_{Fe_2O_3}$. Then, from (5.4) and (5.5) we obtain

$$\Delta A_{d1} = \frac{1 + n\,W_{Fe_2O_3} + m\,Ad}{m\left(1 - b/y - \frac{a\,p}{y\,m}\right)}\;\frac{\Delta y}{y}, \tag{5.6}$$

where $\frac{\Delta y}{y}$ is a relative error of the measurement, and

$$\Delta A_{d2} = \frac{yn - bn - aq}{(ym - bm - ap)^2}\;\Delta W_{Fe_2O_3}. \tag{5.7}$$

Substituting the numerical values of the coefficients gives $\Delta A_{d1} = 1.895\frac{\Delta y}{y}$ and $\Delta A_{d2} = 1.997\,\Delta W_{Fe_2O_3}$. The error for the iron oxide content measured by the fluorescence intensity is rather small (≤ 0.05% mass), so the main contribution to the ΔA_d values is introduced by the relative error of the scattering peak ratio measurements. With standard requirements for the precision of A_d in the limits of ±1%, it is necessary to measure the I_C/ I_R ratios with an accuracy not less than 0.5 %; this requires a pulse accumulation of not less than ~ $5 \cdot 10^4$ at each of the scattering peaks. To support these requirements, a nonstandard scheme of measurements is needed.

5.7.2 Experiment

Powdered coal specimens (with grain size about 60 μm) of 2 g mass were poured into a cylindrical container with a bottom made of Ultralene 3225 with an organic film of 4 μm thickness.

The spectra of X-ray fluorescence and Compton scattering were registered using the energy-dispersion spectrometer, “SPRUT” SEF 01 (JSC “Ukrrentgen”, Ukraine), which was equipped with an SDD detector (X-123, Amptek, USA) and an X-ray tube with a power of 15 W. We applied an original X-ray optic scheme with double-layer Ti/Mo (or Sc/Cu) secondary targets. These targets effectively excited fluorescence of light elements with Ti (or Sc) characteristic radiation and the Mo-*K*α (or Cu-*K*α) “probing” radiation lines gave the Compton and Rayleigh scattering peaks.

In order to obtain the condition, $\frac{\sin\theta}{\lambda_R} \geq 0.6$ Å^{-1}, a specified scattering angle $2\theta \approx 130°$ was set using Soller collimators with angular divergence of 5° (by analogy with the X-ray optical scheme from [47]). We obtained $\frac{\sin\theta}{\lambda_R} = 1.28$ Å^{-1} for Mo-K_α and $\frac{\sin\theta}{\lambda_R} = 0.59$ Å^{-1} for Cu-K_α. The fluorescence lines from chemical elements with atomic numbers Z ≥12 (Mg), as well as Compton and Rayleigh scattering peaks, were registered simultaneously in the common X-ray spectrum (Fig. 5.18). The optimization of the target upper layer (Ti or Sc) by thickness allowed us to obtain the high contrast spectra necessary to measure the scattering peaks with a high precision. When measuring the ratio of the Compton-to-Rayleigh scattering integral intensities with an accumulation time of 300 s, the impulse-statistical error was reduced to 0.2 %.

In the X-ray spectrum of a coal powder sample (Fig. 5.18), the fluorescence lines of mineral components are observable, whereas the background of the bremsstrahlung radiation scattered from the X-ray tube is practically absent. The double-layer Ti/Mo target radiation scattered from the sample shows three peaks. The titanium scattering peak (E = 4.5keV) is not split. The molybdenum scattering peak is split into Rayleigh (E=17.4keV) and Compton (E=16.5keV) types, which vary by width.

In Table 5.6, the I_C/I_R values are given for coal powder samples taken from different deposits. The $W_{Fe_2O_3}$ values were determined by fluorescence, and

the A_d was calculated using Eq. (5.4) and the calibration plot (Fig. 5.19). These samples were independently certified using analytical chemistry.

According to Table 5.6, the standard deviation for the A_d values determined by our method is not more 0.084. Singular spikes of ΔA_d are caused by the fact that the samples were taken from different deposits. Evidently, the special attestation of standards for each deposit is necessary in order to obtain measurements that are more precise. The following coefficients were used: a = 0.865; b = 0.015; p = -0.213; q = -0.186; m = 2.192; and n =1.266

Table 5.6: Determination of the ash mass fraction A_d in coal powder samples using the I_C/I_R ratio and the iron oxide mass fraction $W_{Fe_2O_3}$

Sample	Certificated	Measured		Calculated	
№	A_d, % mass	I_C/I_R	$W_{Fe_2O_3}$ % mass	A_d % mass	ΔA_d % mass
1	48.10	0.4495	3.48	50.18	2.08
2	48.00	0.4649	3.54	46.49	-1.51
3	33.10	0.5212	3.46	35.22	2.12
4	48.30	0.4552	3.65	48.69	0.39
5	50.50	0.4639	3.63	46.66	-3.84
6	28.50	0.5653	4.56	27.40	-1.10
7	39.50	0.4791	4.84	42.52	3.02
8	36.30	0.5046	4.92	37.35	1.05
9	52.70	0.4453	3.89	50.97	-1.73

Table 5.6 continuation

Sample	Certificated	Measured		Calculated	
№	A_d, % mass	I_C/I_R	$W_{Fe_2O_3}$ % mass	A_d % mass	ΔA_d % mass
10	37.20	0.4917	4,44	40.17	2.97
11	41.60	0.4840	4.52	41.69	0.09
12	46.60	0.4806	3,19	43.26	-3.34
13	47.00	0.4624	3.65	46.98	-0.02
14	41.90	0.4751	4.60	43.55	1.65
15	32.00	0.5482	4.30	30.17	-1.83
16	28.20	0.5670	4.64	27.10	-1.10
17	44.70	0.4670	3.39	46.09	1.39
18	37.60	0.5124	4.62	36.08	-1.52
19	38.20	0.4961	4.81	39.06	0.86
20	41.30	0.4851	3,20	42.29	0.99
21	40.00	0.4890	4.32	40,80	0.80
22	50.70	0,4472	3.28	50.88	0.18
23	43.50	0.4731	4.87	43.80	0.30
24	45.40	0.4631	3.61	46.84	1.44
25	45.40	0.4591	3.43	47.90	2.50
26	51.40	0.4478	3.60	50.53	-0.87
27	45.60	0.4594	3.41	47.85	2.25
28	38.60	0.4902	4.80	40.26	1.66
29	47.90	0.4590	3.14	48.12	0.22
30	45.20	0.4676	3.48	45.92	0.72
31	10.30	0.7060	4.94	10.87	0.57

Table 5.6 continuation

Sample	Certificated	Measured		Calculated	
№	A_d, % mass	I_C/I_R	$W_{Fe_2O_3}$ % mass	A_d % mass	ΔA_d % mass
32	16.30	0.6500	4.97	16,42	0,12
33	20,40	0.6215	4.95	19.68	-0.72
34	25,40	0.5730	4.79	26.14	0.74
35	9,40	0.7284	0.32	11.72	2,32
36	13.70	0.6828	1.34	15.26	1.56
37	19.10	0.6411	2.15	19.13	0.03
38	10.50	0.7234	2.78	10.65	0,15
39	15.80	0.6596	3.72	16.16	0.36
40	20.20	0.6141	3.80	21.29	1.09
41	25.10	0.5979	4.29	23.05	-2.05
42	30.00	0.5477	4.37	30.21	0.21

5.8 Nano-impurities in ecology, biology, and medicine

5.8.1 Rapid diagnostics of urinary iodine using a portable EDXRF spectrometer

Iodine is an essential element for human nutrition. Nearly a third of the global population has insufficient iodine intake and is at risk of developing Iodine Deficiency Disorders. Most countries have iodine supplementation and monitoring programs. Urinary iodine is the biomarker used for epidemiological studies; only a few analytical methods are currently routinely used to monitor this. These methods apply quite expensive instrumentation: high-power X-ray sources [74, 75], inductively coupled plasma mass-spectrometry, and instrumental nuclear activation analysis [76]. They can

also be based on destructive sample enrichment. Such sample preparation procedures require time and effort because possible artifacts may result being unable to reproduce the results [77]. Therefore, the destructive sample enrichment is carried out in specialized laboratories with qualified personnel. One of the inexpensive reliable methods to determine trace impurities is X-ray fluorescent analysis (XRF). In the XRF classical arrangement, the excitation of sample atoms is realized by the X-ray tube primary spectrum, which contains broadband bremsstrahlung radiation and the analytical lines of the target material. Therefore, the X-ray spectrum of the sample not only shows the fluorescence lines of its atoms, but also the broadband background of the primary radiation, which is scattered in the sample. This background limits the sensitivity of the XRF analysis. For this reason, direct XRF determination of iodine in urine is impossible because the iodine concentration is in the range of 50 to 200 μg/L (or from 0.05 to 0.20 ppm) [76]. However, by using a simple evaporating procedure, the sample can be enriched by a factor of 30: i.e. the iodine content increases from 1 to 6 ppm due to the removal of the water. After the water evaporation, the sample is a jelly-like residue containing the carbon constituent. Therefore, this residue strongly scatters the primary X-ray radiation. According our calculations and experiments, the background level of the continuous spectrum scattering is quite high and allows no possibility of determining iodine concentrations lower than 10 ppm. Therefore, the sensitivity of the classical XRF arrangement is found to be insufficient for the determination of 1 ppm iodine in jelly-like residue. In the energy dispersion X-ray fluorescent analysis (EDXRF), the selective excitation of sample fluorescence was used in order to lower the detector charging [13]. For selective excitation, the X-ray primary radiation is transformed using secondary targets, filters, and so on. In the transformed spectrum, a high in-

tensity sector is formed in the specific energy range for the effective excitation of analyzed chemical elements, while the intensity of the rest of the spectrum is being minimized. The transformation of the primary spectrum always decreases the intensity of the analytical lines of sample impurities. However, lowering the broadband background sharply increases the contrast (peak-to-background ratio), which defines the sensitivity of the method. Thus, in order to achieve the maximum sensitivity, it is necessary to calculate the optimal parameters of the X-ray optical scheme. The optimization task can be solved for a special range of photon energies where the analytical lines of the impurity are positioned. For this purpose, calculations are carried out for the distribution of the background created by the primary radiation scattered by the sample, intensities of the sample fluorescence lines, and artifact peaks [13]. The solution for the optimization inverse problem consists of selecting and varying the materials and thicknesses of both the secondary targets and filters, as well as the configuration of the collimation system to obtain the minimum detection limit. This optimization increases the sensitivity by a factor of 50 [37, 38]. It is sufficient for the determination of iodine in jelly-like organic residue that contains about 1–6 ppm of iodine (taking into consideration the thirtyfold enrichment after the water evaporates).

Computer processing of the X-ray fluorescence spectrum was applied to reveal and separate the Ca-$K\beta$, I-$L\alpha$ and I-$L\beta$ fluorescence lines. In the literature, mathematical methods for treatment of the spectra are well known [78]. However, these are unacceptable for this problem because, when the whole spectrum is treated, the contribution of high-intensity lines is dominant in the residual function. Thus, it is impossible to reveal the intensity variations of weak lines. Therefore, we selected a narrow spectral

area in the photon energy range from 3.8 to 4.4 keV where strong lines were absent for the processing. This allowed us to decrease the approximation error to 3–5%.

The Sample Preparation Procedure

The first stage of the preparation for the X-ray fluorescent analysis is the samples' enrichment with iodine via water evaporation. Because of the iodine vapor's high partial pressure, a fractional volatilization of iodine is possible. Therefore, it is important to choose the optimal temperature for evaporation. The evaporation temperature was chosen using the experimental dependence of I-*L*α (E = 3.93 keV) and I-*L*β (E = 4.22 keV) fluorescence line intensities on the evaporation temperature in comparison with their intensities at 20°C for the same sample. A 20% decrease of iodine fluorescence line intensities was revealed after evaporation at 80°C.

There was no decrease in the temperature range of 30 to 40°C; therefore, this range was considered to be optimal for the iodine enrichment. The sample contained a substantial quantity of calcium, and the strong Ca-*K*β fluorescence line (E = 4.01keV) was close to the iodine line I-*L*α (E = 3.93keV) in the spectrum. The energy resolution of the detector was insufficient to separate these lines. In order to remove the calcium from the sample, we applied Sulkovich. This allowed us to lower the calcium concentration by about four orders of magnitude.

Preparation of Calibration Mixtures

Calibration mixtures were prepared in the biological liquid sample by adding KI water solutions with different iodine concentrations ("the method of additions" [4, 5]). The first mixture (zero) had the following composition:

0.8 g urine, 0.1 g Sulkovich, and 0.1 g distilled water. To increase the iodine concentration, the next three mixtures were prepared by adding 0.1 g of KI water solution to various iodine contents (1000, 2000, and 3000 μg/L) to the "zero" composition instead of the distilled water. As a result, we obtained four calibration mixtures with additional iodine concentrations: 0, 100, 200, and 300 μg/L [5]. The calibration mixtures and the experimental samples were placed on Ultralene 10 film and dried at T=30 - 40°C in a dustproof chamber to obtain the jelly-like residue. After the procedure, the composition of the dried sample filler was slightly changed, and a linear calibration could be used to determine the concentration sensitivity of the I-$L\alpha$ and I-$L\beta$ lines independently.

Measuring Technique

The X-ray fluorescence spectra of the prepared samples were recorded using a portable EDXRF spectrometer "SPRUT-K" (JSC "Ukrrentgen", Ukraine) with an SDD detector (X-123, Amptek, USA) and an X-ray tube of 15 W with an Ag anode. The time for the spectrum accumulation was 3600 s. The X-ray optical scheme was optimized to provide the maximum sensitivity for revealing the iodine I-$L\alpha$ and I-$L\beta$ lines in the matrix, which consisted of Na, K, Cl, P, S, and carbon constituents. The mass portions of the main components of the matrix were determined by using XRF, and the carbon portion by using the ratio of Compton and Rayleigh scattering peaks [7]. The optimization parameters were as follows: the material of the secondary target; the material and the thickness of the filter; radiation incident and exit angles; the aperture of collimation system; and the thickness of the jelly-like sample. As a result of the optimization procedure, the following set was used: a chromium secondary target; an incident angle of

24±5° for the sample; a 4 μm vanadium filter for the secondary emission; and a Soller collimator positioned directly in front of the detector.

Results and discussion [79]

The experimental spectrum of the calibration sample with 300 μg/L iodine (Fig. 5.20) shows the fluorescence lines of chemical elements of the jelly-like residue and the secondary target lines scattered by the sample (Cr-*K*α, Cr-*K*β). The calcium lines were absent in the general spectrum as a result of the sample treatment with Sulkovich. There was a reasonably low background in the energy range of 3.8 to 4.3 keV near the lines of interest, I-*L*α (E = 3.93keV) and I-*L*β (E = 4.22 keV), which only exceeded the theoretically calculated minimum value twice. The intensities of the iodine analytical lines corresponded to the calculated values. The obtained contrast level of the iodine lines allows the possibility of determining iodine concentrations less than 100μg/L in biological liquids using calibration mixtures.

The I-Lα and I-Lβ lines can determine the iodine content independently. Note, that in the second case (I-*L*β), the concentration sensitivity of the calibration function is lower because of the I-*L*β line's doubly lower integral intensity. However, the stronger I-*L*α overlaps the Ca-*K*β line from the residual calcium after the Sulkovich treatment. The positions of the I-*L*α (E = 3.93keV) and Ca-*K*β (E = 4.01keV) lines are different at 0.075 keV in energy, and their experimental half-widths are about 0.130 keV in our spectrum. Therefore, these lines can only be separated using full-profile analysis for the spectral range of 3.8 to 4.1 keV. Gaussian profiles were taken for each line for this separation. The Gaussian curve half-width was determined by the spectra of standards. The separation was carried out within the multiplet.

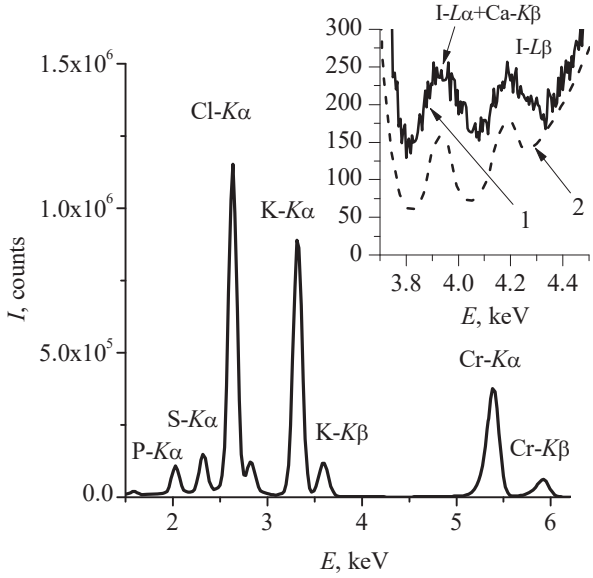

Figure 5.20: A fragment of the spectrum recorded for the calibration sample treated using the drug, Sulkovich. Iodine concentration is about 300 μg/L. In the insert: fragments of the experimental spectrum (curve 1), and the calculated (curve 2) spectrum in a photon energy range of 3.8 to 4.4 keV.

The adequacy of the separation is confirmed by the results of the mathematical processing of the calibration mixtures' different spectra in the iodine concentration, which is similar in quantity to the residual calcium (Fig. 5.21). As seen from the figure, the intensity of the Ca-*K*β line remains practically unchanged as the iodine concentration grows in the calibration mixture, while the intensity of the separated I-*L*α line increases proportionally to the iodine concentration.

In order to find the quantitative determination of iodine concentrations use I-$L\alpha$ intensities, the calibration mixtures based on urine samples from different patients were used (Fig. 5.22). Plot 1 corresponds to urine samples with "low" iodine contents (from 100 to 110 μg/L), and plot 2 is based on samples with a "high" iodine concentration (about 180 μg/L). Naturally, these plots are shifted by the Y-axis, but have the same slopes. The experimental value $\partial I / \partial C$ = 300 counts/ (100 μg/L) corresponding to the theoretically calculated one was determined from the slope.

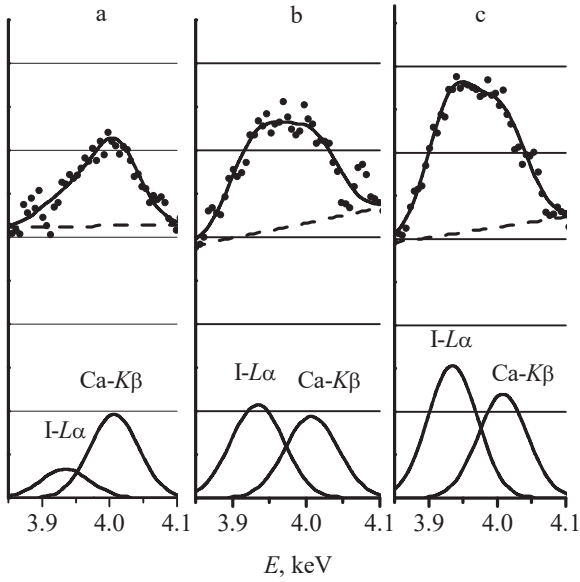

Figure 5.21: Separation of superimposed I-L_α and Ca-K_β lines in the spectra of calibration mixtures with different iodine contents: a, without additional iodine; b, with 200 μg/L of additional iodine; and c, with 300 μg/L of additional iodine.

The integral intensity of the background, I_b, can be determined by the area bounded by the background line under the experimental curve (Fig. 5.20).

Then use, $I_b = I_b^1 \times n$, to measure the intensity, where I_b^1 is the average accumulation of counts per a channel and *n* is the number of channels over which the summation takes place. Taking into account I_b^1 = 140 counts and *n* = 15 channels, we obtain a detection limit of C_{min}= 45.8 μg/L for the I-*L*α line. The theoretical detection limit is C_{min} = 32 μg/L at I_b^1 = 70 counts/channel (Fig. 5.20). Thus, the experimentally achieved sensitivity is only a factor 1.5 worse than the highest of the theoretically possible values. For an I-*L*β line with I_b^1 = 170 counts/s and $\partial I / \partial C$ = 200 counts/(100μg/L), we obtain C_{min} = 75.7μg/L. The achieved sensitivity level is sufficient for iodine in urine diagnostics in a concentration range of 50 to 200 μg/L.

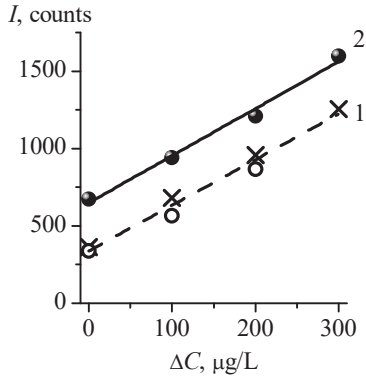

Figure 5.22: The dependence of the I-L_α line integral intensity on the additional iodine mass portion, Δ*C*, in the calibration mixture: 1, the iodine concentration in the initial sample is 100 μg/L; and 2, the iodine concentration in the initial sample is 180 μg/L.

Table 5.7: Iodine fluorescence I-*Lα* and I-*Lβ* peak intensities, and the results of determination of iodine concentrations in urine from different patients. The concentration sensitivity in the peak intensity is 40 counts/ (100 μg/L) for the I-*Lα* line, and 26 counts/ (100 μg/L) for the I-*Lβ* line.

№	I-*L*α, counts	I-*L*β, counts	Determined iodine concentration, μg/L	
			by I-*L*α line	by I-*L*β line
1	54.91	30.48	138	118
2	70.57	40.91	176	158
3	35.86	19.32	90	75
4	31.89	18.24	80	70
5	30.76	26.20	77	100
6	50.14	39.36	125	152
7	55.48	36.60	139	142
8	40.67	28.60	102	110
9	50.47	37.10	126	142
10	45.01	31.00	142	119
11	49.79	31.40	125	121
12	69.50	35.10	174	135

The results of clinical investigations for a group of patients are given in Table 5.7. The integral intensities (according to the expression for C_{min}) to evaluate the detection limit have been given so that they can be compared with Figure 5.20. Patients 3, 4, and 5 has lowered iodine concentration, and patients 2 and 12 had heightened levels (about 100-150 μg/L).

The measurements of the urine samples obtained from different patients confirm the good convergence of the results of the iodine independent determinations with I-$L\alpha$ and I-$L\beta$ line intensities. Using such measurements, it is possible to rapidly obtain information about the iodine concentration in the patient's urine and its variations during the patient's treatment. The increase in the accuracy of the measurements can be achieved by improving the statistics of counts accumulation; for example, by increasing the X-ray source power and the optimized X-ray optic scheme.

5.8.2 Biological tissues

The identification of "trace" impurities in biological tissues without their destruction is complicated not only due to the presence of a strongly scattering base, but also the presence of intense spectral lines in the main components: such as sulfur, phosphorus, potassium, and calcium. This makes it difficult to measure weak impurity lines in a wavelength range from 3 to 6.5 Å. However, after eliminating the scattering background, it is possible to measure the fluorescent radiation intensity of elements (with a high sensitivity) in the wavelength range of 0.75 to 3 Å, where the *K*-series lines of the elements from titanium (Z=22) to strontium (Z=38) and the *L*-series lines from iodine (Z=53) to bismuth (Z=83) are located. The content of chemical elements from yttrium (Z=39) to tellurium (Z=52) can be determined by the *L*-series lines in the absence of their superposition on the intense lines of the main components. In some cases, in order to avoid this overlap, special methods of sample preparation are used to remove one of the main components, such as in the analysis of iodine in urine [79]. Measuring light elements—sodium, magnesium, aluminum, silicon, and phosphorus—can be performed by the *K*-series lines with a sensitivity of 1 to 110 ppm without destroying the sample. The measurements of the

Compton scattering in tissues make it possible to determine an important characteristic: the fraction of the carbon component on which many properties of tissues depend. Such an analysis can be carried out using a common X-ray spectrum, which includes both fluorescence lines and the scattered lines of the secondary target.

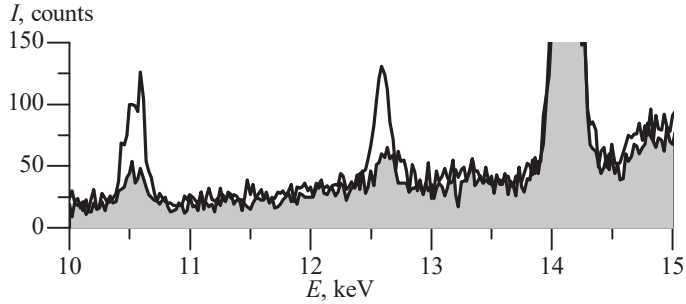

Figure 5.23: Fragments of X-ray fluorescence spectra show the increase heavy elements (lead) content in the bone tissue of a laboratory animal when these substances were added to their food. The secondary target was molybdenum and the exposure was 600 s.

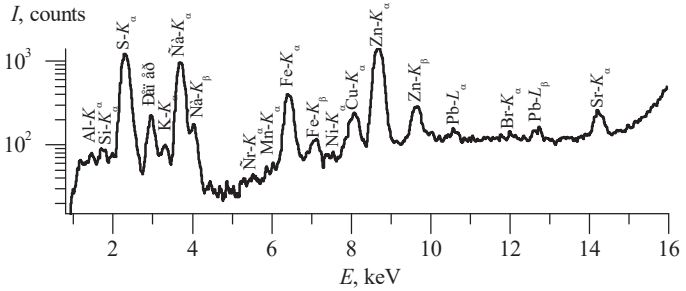

Figure 5.24: X-ray fluorescence spectrum of human hair. The secondary target was molybdenum and the exposure was 600 s.

The dissection of bone tissue for X-ray examinations involves cutting thin sections. The study can be performed separately for both compact and internal part via the appropriate localization of the irradiated sample area. Figure 5.23 shows a significant change in the lead content in animal bone, when they had consumed this substance.

The diagnosis of many diseases in the early stages can be performed by analyzing the content of microelements in the hair. However, for this diagnosis, several tens of trace elements need to be measured, which results in significant time and material costs. In Figure 5.24, the lines of fourteen chemical elements are clearly observable in the X-ray fluorescence spectrum of human hair. The content of these impurities can be quantified within 600 seconds.

The achieved sensitivity increase allows us to expand the use of X-ray methods in the research of biological objects and to diagnose many human diseases at early stages.

5.8.3 Drinking water and food

Sanitary standards for drinking water control allow for the sensitivity of methods that determine most of the chemical elements at a level of 0.01 ppm to 1ppm. This sensitivity can be achieved in XRF only by means of sample enrichment: for example, by drying. Figure 5.25 shows the spectra of drinking water concentrated by evaporation. For most chemical elements, detection limits have been reached at a level of 0.01 to 0.1 ppm, which is quite sufficient for practical measurements.

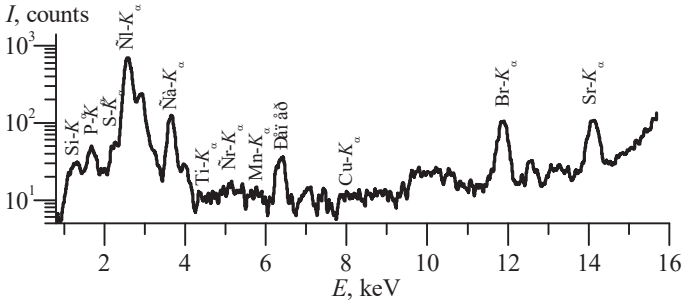

Figure 5.25: Fragment of the experimental X-ray fluorescence spectrum of mineral water. The measuring mode is a tube with an Ag anode, U = 35 kV, I = 170 μA; the secondary target is Mo; and the exposure is 600 s.

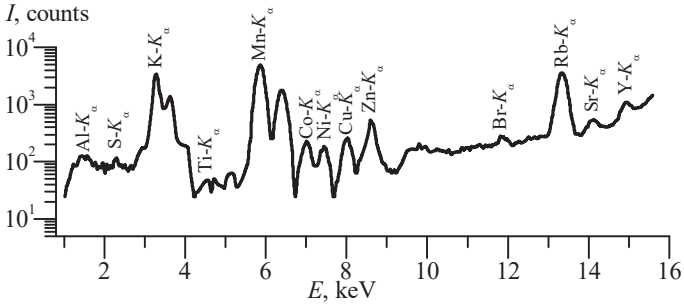

Figure 5.26: Fragment of the experimental X-ray fluorescence spectrum for tea. Measuring mode: tube with an Ag anode, U = 35 kV, i = 170 μA, secondary target is Mo, and the exposure is 600 s.

Unlike water, food contains an organic component that cannot be removed by simple evaporation, but requires a destructive preparation (e.g., ashing). This sample preparation is very complicated and can lead to the appearance of artifacts in the analytic spectrum. The advantage of the XRF methods considered above, in comparison with classical methods, is the possibility of determining the content of micro-impurities in objects with

an organic component. However, the sensitivity is lower than in the case of evaporated water.

Figure 5.26 shows the spectrum for tea. The characteristic value of the detection limit in the range of elements with Z from 22 to 83 is C_{min}~1 ppm.

Conclusion

This book proposed a general approach to optimizing X-ray spectra using the criterion of the detection limit and its special applications: the selection of the materials for monochromators, configuration and materials for secondary targets, filter thicknesses, and so on. This solution can be applied to any shape of preliminary radiation spectrum: synchrotron radiation, ondulator radiation, laser-electron generator radiation, etc. We hope that the proposed information will promote the creation of new X-ray optic schemes that form X-ray radiation into the optimal spectrum to obtain the maximum sensitivity to “trace” impurities between 0.01 and 0.1 ppm without any destruction to the sample.

REFERENCES

1. Quantitative X-Ray Spectral analysis / N.F. Losev // Moscow: Nauka, 1969. – 336 p.
2. Theory of XRF: getting acquainted with the principles/ P. Brouwer// PANalytical B.V., Almelo, the Netherlands, 2010.
3. Röntgenfluoreszenzanalyse Anwendung in Betriebslaboratorien / Von einem Autorenkollektiv unter Federführung von Dr. rer. nat. H.Ehrhardt / Leipyig : VEB Deutscher Verlagfür Grundstoffindustrie 1981
4. X-Ray Fluorescent Analysis / V.P. Afonin, N.I. Komyak, V.P. Nikolayev, R.I. Plotnikov; Ed. by N.F. Losev. – Novosibirsk: Nauka, 1991. – 171 p.
5. Handbook of Practical X-Ray Fluorescence Analysis, by B. Beckhoff, B. Kanngießer, N. Langhoff, R. Wedell, and H. Wolff.//- Berlin: Springer, 2006.
6. The optical principles of the diffraction of X-rays/ R.W. James// The crystalline state – VOL.II editor: sir L. Bragg/ London, 1950.
7. Compton A.H. A Quantum Theory of the Scattering of X-rays by Light Elements / A.H. Compton // Phys. Rev.- 1923.- Vol. 21.- P. 483-502.
8. Estimation of the sensitivity limit of X-ray fluorescence analysis / Y.G. Lavrentiev, E. E. Weinstein // Equipment and methods of X-ray analysis.- 1968.- V. 3.- p. 3 – 18.
9. Detection limit and estimate of uncertainty of analytical XRF results/ DR. Richard, M. Rousseau// The Rigaku journal V. 18 (2) 2001.
10. Fluorescent X-Ray Spectral analysis / K.V. Anisovich// Rentgenotekhnika: Reference-Book: in two vol.; Ed. by Klyuev V.V. – Moscow: Mashinostroyenie, 1980. – P. 129–184.
11. Tables of integrals, sums, series and products / I.S. Gradstein, I.M. Ryzhik// - Moscow: Science, 1971.
12. Wavelength Dispersive X-ray Fluorescence Method Development for Asphaltene Samples/ Tuisku Aaro.// Metropolia Ammattikorkeakoulu.- (2018)
13. Energy-Dispersive X-ray Fluorescence Analysis Using X-ray Tube Excitation / A.T Ellis // Handbook of x-Ray Spectrometry. Second

Edition, Revised and Expended, [editors: E. Van Grieken, A. Markowicz].- 2001.- ch. 3.
14. X-Ray fluorescence analysis with sample excitation using radiation from a secondary target / Vasin M.G., Ignatyev Yu.V., Lakhtikov A.E. [et al.] // X-Ray Spectrometry.- 2007.- T. 36, № 4.- C. 270-274.
15. Prospects for increasing the sensitivity of fluorescence X-ray analysis / K.V. Anisovich // Equipment and methods of x-ray analysis. - L.: Mashinostroenie.- 1980.- p. 61-70.
16. Polarized Beam X-Ray Fluorescence Analysis / J. Heckel, R. Ryon // Handbook of X-Ray Spectrometry. Second Edition, Revised and Expended, [editors: E.Van Grieken, A. Markowicz].- 2001.- ch. 10.
17. Optical flats for use in X-ray spectrochemical microanalysis / Y. Yoneda, T. Horiuchi // Rev. Sci. Instrum.- 1971. – Vol. 42.- P. 1069-1070.
18. Comparison of thermoelectrically cooled and conventional Si(Li) X-ray detectors / N. Haselberger, A. Markowicz, V. Valkovic // Appl. Radiat. Isot.- 1996.- 47(4).- P. 455-459
19. Silicon drift detectors for high resolution, high count rate X-ray spectroscopy at room temperature / P. Lechner C. Fiorini, A. Longoni [et al.] // Nucl Instrum Meth Phys Res A.- 2001.- Vol. 458, № 1.- P. 281-287.
20. www.amptek.com.
21. Detrmination of the si-pin detector active zone thickness using analytic line intensity wavelength dependence of the single-component standards/ Mamaluy, A.A., Fomina, L.P., Mikhailov, A.I.// Journal of Nano- and Electronic Physics. .- 2010 V. 2 (4) pp115-118
22. X-Ray Microscopy/ G. Schmahl, D. Rudolph// Proceedings of the International Symposium, Göttingen, Fed. Rep. of Germany, September 14–16, 1983
23. X-Ray Monochromators Based on Fullerite C60 Epitaxial Films / I.F. Mikhailov V.E. Pukha, A.A. Baturin // Zavodskaya Laboratoria. – 2006. – V. 72, № 3. – P. 21–25.
24. X-ray analysis / P.A. Verkhovodov.- K.: Naukova Dumka.- 1984.- 161p.
25. Handbook on X-ray analysis of polycrystals / L.I. Mirkin; [ed. Ya.S. Umanky] .- M .: GIFML, 1961.- 863 p.
26. An efficient X-ray spectrometer based on thin mosaic crystal films and its application in various field of X-ray spectroscopy / H. Legall, H. Stiel, M. Schnurer, M. Pagels, [at al.] // J.Appl.Cryst.- 2009.- Vol. 42.- P. 572-579.

27. Modified X-ray optical Bragg-Soller scheme for scanning spectrometer / I.F. Mikhailov, A.A. Baturin // Visnyk SumU.- 2007.- № 2.- P. 27-32.
28. Condensed films obtained from highly ionized C60 molecular beam / V.A. Dudkin V.E. Pukha, A.S. Vus, E.N. Zubarev, [et al.] // Functional Materials.- 2002.-Vol.9, №3.-P. 481-486.
29. Fullerenes / A.V. Yeletsky, B.M. Smirnov // Uspekhi Fizicheskikh Nauk.-1993. - T.163, No. 2.- P.33-49.
30. Measuring of fullerene molecular form factor in condensed C60 films / I.F. Mikhailov, V.E. Pukha, O.V. Sobol, V.V. Varganov // Functional Materials.- 2003.-Vol.10, №2.- P. 266-269.
31. Molecular form factor and analysis of the diffraction pattern of fullerene crystals / E.V. Shulakov, R.A. Dilanyan, O.G. Rybachenko, V.Sh. Shechtman // Crystallography.-1996.-T.41, No. 1.- S. 39-42.
32. Luzzi D.E., Fischer J.E., Wangetal X.Q. //J. Mater. Res.-7.-335.-1992.
33. X-rays and extreme ultraviolet radiation principles and applications/ D. Attwood, A. Sakdinawat// Cambridge University Press. 2017.
34. Short-period multilayer X-ray mirrors for “Water” and “Carbon windows” wavelengths/ I. Kopylets, O. Devizenko, E. Zubarev [at al.]// J. Nanosci. Nanotechnol. 2019. Vol. 19 (1).
35. I. A. Artyukov, R. M. Feschenko, A. V. Vinogradov, Y. Bugayev, O. Y. Devizenko, V. V. Kondratenko, Y. Kasyanov, T. Hatano, M. Yamamoto, and S. V. Saveliev, Micron 41, 722 (2010).
36. Detection limits evaluation of a portable energy dispersive x-ray fluorescence setup using different filter combinations/ S. Pessanha A. Samouco R. Adão [at al.]// X-ray Spectrometry. V.46 (2). 2017.
37. Detection Limits of Impurities in Light Matrix in the X-Ray Scheme with a Secondary Radiator // I.F. Mikhailov, A.I. Mikhailov A.A. Baturin, L.P. Fomina // Instruments and Experimental Techniques, 2012. – № 4. – P 80–85.
38. Increasing the sensitivity of X-ray fluorescent scheme with a secondary radiator using the initial spectrum filtration / I.F.Mikhailov, A.A.Baturin, A.I.Mikhailov, S.S.Borisova // Functional Materials, 2012. – Vol.19, No.1. – C. 126-129.
39. X-ray fluorescence determination of trace gold in an ion-exchange resin/ I.F. Mikhailov, I.F. A.I. Mikhailov A.A. Baturin, L.P. Fomina// Inorganic Materials.- V. 50, (14), (2014) pp. 1402–1404.
40. Contrast Enhancement of X-Ray Fluorescence Spectra Using a Secondary Two-Layer Radiator / I.F. Mikhailov, A.A. Baturin, A.I.

Mikhailov, S.S. Borisova // Functional Materials, 2011. – Vol.18, No.2. – p. 150-155.

41. Source of Monochromatic X-Rays Based on a Two-Stage Secondary Radiator / A.A. Mamaluy, A.A. Baturin, A.I. Mikhailov, // Problems of Atomic Science and Technology, 2012. – № 2. – P 139–143.
42. Effects of Diffraction in X-Ray Fluorescent Analysis and Application in Analytical Purposes / Kalinin B.D. Rudnev A.V. // Analitika i Kontrol. M., 2011. – V. 15, №3. – P. 332-338.
43. Quantitative Analysis of structure Reflections in X-Ray Fluorescence Spectrum / I.F. Mikhailov, V.V. Belozerov, A.A. Baturin, A.I. Mikhailov // Zavodskaya Laboratoria, 2013. – V. 79, № 7. – P. 7–14.
44. Metal Science and Thermal Treatment of Steel / M.L. Bernshtein, A.G. Rachschtadt // Handbook – M. Metallurgy, 1983. – V. 1. – P. 94–142.
45. Introduction to Quantitative X-Ray Diffraction Methods (prepared by James R. Connolly, for EPS400, Introduction to X-Ray Powder Diffraction, Springer, 2012)
46. X-ray and electron-optical analysis / S.S. Gorelik, Yu.A. Skakov, L.N. Rastorguev.- M .: MISIS, 1994. 320p.
47. Determination of light element content by superimposed spectra of X-ray fluorescence and diffraction / I.F. Mikhailov, A.A. Baturin, A.I. Mikhailov, L.P. Fomina // Problems of Atomic Science and Technology , 2013. – № 2 (84). – P. 172–176.
48. The Distribution of Energy Between the Modified and the Unmodified Rays in the Compton Effect / Y.H. Woo // Phys. Rev., 1926. – Vol. 27, No. 2. – P. 119–129.
49. Physics of X-rays / M.A.Blokhin.- Moscow .: State publishing house of technical and theoretical literature, 1953.- 456 p.
50. Coherent and incoherent scattering of 17.44 and 6.93 keV X-ray photons scattered from biological and biological equivalent samples: characterization of tissues/ M. E. Poletti, O. D. Gonçalves, I. Mazzaro// X-ray Spectrometry. V.31 (1). 2002. 57-61 pp.
51. Authentication of vegetable oils by confocal X-ray scattering analysis with coherent/incoherent scattered X-rays./ Li F, Liu Z, Sun T.// Food Chem. 2016. 435-441pp.
52. Determination of coherent to Compton scattering differential cross section ratios of some inorganic materials with EDXRF/ D. Yılmaz, Ü. Şimşek, T. Akkuş, Y. Şahin // Can. J. Phys, 2017, 95(4): 407-411.

53. Coherent and incoherent scattering of 14.93, 17.44 and 21.12 keV photons from Al, Cu, Sr, Cd, Ce, Pr, Sm, Pt, Au and Pb/ D. V. Rao, R. Cesareo, and G. E. Gigante // Physica Scripta 50 (3), 314 (1994).
54. Improved Rayleigh to Compton scattering ratio curves for mass attenuation coefficients determination for X-ray fluorescence analysis/C.C. Conti, M.J. Anjos, C.M. Salgado// X-ray Spectrometry. V.46 (6). 2017. 522-528 pp.
55. Use of intensity of the X-ray radiation disseminated by substance in practice of X-ray fluorescent analysis / A. L. Tsvetyanskii, A. N. Eritenko//Analitika i kontrol 18 (1), 4-22 (2014)
56. Gaining improved chemical composition by exploitation of Compton-to-Rayleigh intensity ratio in XRF analysis/ Vasile-Dan Hodoroaba, Vanessa Rackwitz// Analytical Chemistry, 86 (2014) 6858-6864; DOI: 10.1021/ac5000619.
57. Determination of coal ash content by combined X-ray fluorescence and scattering spectrum/ Mikhailov, I.F., Baturin, A.A., Mikhailov, A.I., Borisova, S.S., Fomina, L.P.// Rev. Sci. Instrum. 2018; 89(2)
58. Theoretical and experimental study on the angular dependence of scattering processes in X-ray fluorescence systems/ M. Guerra, M. Manso, S. Pessanha, S. Longelin, and M. L. Carvalho// X-Ray Spectrometry 42 (5), 402-407 (2013)
59. Pirenne H.M., The diffraction of X-rays and electrons by free molecules/ Cambridge University Press, Cambridge (1946)
60. Über die inkohärente Streuung von Röntgenstrahlen / W. Heisenberg// Physik. Zeitschr/ 32, 737–740 (1931).
61. Surface and Thin Film Analysis: A Compendium of Principles, Instrumentation, and Applications, Second Edition/Editors: Prof. Dr. Gernot Friedbacher Dr. Henning Bubert // Wiley VCH Verlag GmbH & Co. KGaA (2011)
62. Energy dispersive electron probe microanalysis (ED-EPMA) of elemental composition and thickness of Fe-Ni alloy films/ Hodoroaba, V.-D.; Kim, K.J.; Unger,W.E.S.// Surf. Interface Anal.// 2012, 44, 1459–1461.
63. X-ray Microanalysis of Precious Metal Thin Films: Thickness and Composition Determination/ Giurlani, W.; Innocenti, M.; Lavacchi, A.//Coatings 2018, 8, 84.
64. Determination of mass fraction of light elements in crystalline materials by Compton-to-Rayleigh scattering intensity ratio / I.F. Mikhailov, O.V. Sobol, V.V. Varganov, L.P. Fomina // Functional Materials, 2002. – Vol. 9, № 4. – P. 651.

65. X-ray and thermal neutron scattering theory in real crystals / M.A. Krivoglaz// Moscow: Science.- 1967.- 336 p
66. Shifting Compton's Peak under Increasing Content of Carbon in Steel / I.F. Mikhailov, L.P. Fomina, A.A. Baturin // Problems of Atomic Science and Technology. – 2006, № 1. – P. 103–105.
67. Official site of AS «Ukrrengen» (Kharkov): www.ukrrentgen.kharkiv.com.
68. Determination of gold content by the energy-dispersive X-ray spectral method in solutions and ion-exchange resins / Verigin AA, Naumik A.I., Madzhara E.O. - Abstracts of the VII Conference "Analytics of Siberia and the Far East", (2004). - p. 45.
69. High-Stable Standard Samples of Mass in the Nano-Gram Range / I.F. Mikhailov, A.A. Baturin, A.I. Mikhailov [et al.] // Functional Materials, 2013. №2.- C. 266-271.
70. ISO 1928:2009 Solid mineral fuels - Determination of ash.
71. EDXRF Analysis of Coal by FP Method /Application Notebook Feb 01, 2013 By Applied Rigaku Technologies, Inc.,
72. Wissmann D. Journal of ASTM International, 2, 9, 125 (2005).
73. Evaluation of low-rank coals as raw material for Fe and Ca organomineral fertilizer using a new EDXRF method/ Chassapis K., Roulia M.// International Journal of Coal Geology, 75, 3, 185 (2008).
74. A correlation of breast cancer and calcium levels in hair analyzed by X-ray fluorescence/ Chikawa J, Mouri Y, Shima H, Yamada K, Yamamoto H, Yamamoto S// J XraySciTechnol 2014; 22:587-603.
75. Concentration homeostasis and elements in hair and dried serum observed by X-ray fluorescence analysis using synchrotron radiation/ Chikawa J, Mouri Y, Shima H, Yamada K, Yamamoto H, Yamamoto S// J XraySciTechnol 2014; 22:471-491.
76. Review of analytical methods for the quantification of iodine in complex matrices/ C. Phillip, K. Dasgupta// Analytica Chimica Acta. (2011). 702:16–36. doi: 10.1016/j.aca.2011.05.039
77. Measurement of Urinary Iodine Levels by Ion-selective Electrode: Improved Sensitivity and specificity by Chromatography on Anion-Exchange Resin/ by Guy E. Abraham, MD, Jorge D. Flechas, MD and John C Hakala// RPh The Original Internist, December, 2004 pp 19-31
78. Computer simulation of a backscattered X-ray fluorescence system/ AL-Ghorabie, Fayez H.H // Journal of X-Ray Science and Technology, vol. 23, no. 1, pp. 57-64, 2015

79. Rapid diagnostics of urinary iodine using a portable EDXRF spectrometer/ I.F. Mikhailov, A.A. Baturin, A.I. Mikhailov [at al.]// J. XraySciTechnol 25 (2017) pp. 515–521.